ABSTRACT

Title of Dissertation: PHASE MEASUREMENTS WITH A TWO-MODE SQUEEZED STATE OF LIGHT.

Prasoon Gupta,

Doctor of Philosophy, 2019

Dissertation directed by: Dr. Paul D. Lett,

Adjunct professor, Department of Physics

Joint Quantum Institute

NIST/University of Maryland

Introducing squeezed states of light into interferometers can increase the phase sensitivity of the device beyond the standard quantum limit (SQL). We discuss an SU(1,1) interferometer, where nonlinear optical elements replace the beam splitters in a Mach-Zehnder interferometer. A two-mode squeezed state of light is generated inside of such an interferometer. We talk about the phase sensitivities of an SU(1,1) interferometer with different detection schemes and their improvement over the SQL. We also discuss the concept of an optimal detection scheme for phase measurement in an interferometer. We describe a modification

of the SU(1,1) interferometer which reduces the experimental complexities while giving the same phase sensitivity. We call the design a truncated SU(1,1) interferometer. We show our experimental results of 4 dB improvement in phase sensitivity over the SQL using a truncated SU(1,1) interferometer. We also compare the theoretical sensitivities of vacuum-seeded configurations of a conventional and a truncated SU(1,1) interferometer, and show our experimental results for the phase sensitivity of the truncated version. We explain the dependence of phase sensitivity on the measurement of squeezing. We talk about the methods to improve the measurement of squeezing in a 4-wave mixing experiment, and our efforts in implementing them. Finally, we mention our progress in measuring a big phase shift using an adaptive algorithm in the truncated SU(1,1) interferometer, and discuss the technicalities involved in big phase measurements.

OPTICAL PHASE MEASUREMENT WITH A TWO-MODE SQUEEZED STATE OF LIGHT

by

Prasoon Gupta

Thesis submitted to the Faculty of the Graduate School of the
University of Maryland, College Park in partial fulfillment
of the requirements for the degree of
Doctor of Philosophy
2019

Advisory Committee
Professor Steven Rolston, Chair
Dr. Paul D. Lett
Dr. Alan Migdall
Professor Wendell Hill
Professor Mohammad Hafezi

Dedication

To

my mother Sunita Gupta

and

my father Daya Nand Gupta

Acknowledgements

I wouldn’t say the depth of my gratitude is smaller for anyone who has helped me in my career. But when it comes to my Ph.D., I don’t think it requires a second thought in acknowledging my indebtedness towards my advisor prof. Paul Lett, his guidance has been very helpful over the years. He has maintained a good balance in providing mentorship and letting me do things in my own way, which helped me significantly not only in learning physics but also in pushing a project forward by bringing in new ideas to the experiment. There were many moments when his pieces of advice proved invaluable in the course of building a new experiment as well as in trying new things. He has guided me in every aspect of my Ph.D. that it is redundant to provide any specific example in this case.

I am very grateful to Brie Anderson, who worked as a postdoc during the first four years of my research. She had a major influence on my course of Ph.D. She taught me significantly about experimental physics, from the basics of operating a device to a successful implementation of an experiment. Additionally, her ideas on most issues that I encountered during my research were very informative and applicable.

I also had the opportunity to have significant interactions with Travis Horrom and Bonnie Schmittberger. Both spent their postdoc years in the group while me pursuing my Ph.D. They provided their invaluable expertise on multiple projects we performed together. I was able to learn ample things from them throughout their stay. Though I interacted with Carla Hermann-Avigliano for a short time, conversations with her were very fruitful and helped me in my journey.

Kevin Jones's ideas and bits of advice have always provided new and successful routes to the experiments, they have also guided me in learning new things and have benefitted me in my Ph.D. Conversations with Elizabeth Goldschmidt have always been enlightening and have given me an understanding of other closely related fields to my research area. Alessandro Restelli has been one of the most wonderful people at JQI and has assisted me in most electronics issues that I have encountered in my lab. His diligence on every difficulty I have ever presented to him is simply incomparable.

Rory Speirs joined the lab in early 2018 and has already helped me in two projects. Working with him has been wonderful, and his skills have pushed us in making significant strides in both the experiments. Friendly exchanges with Nicholas Brewer have been wonderful, and his amicable behavior has helped me to overcome the stresses of a Ph.D. Ryan Glasser was there on my first Ph.D. project and provided helpful theoretical groundwork for the experiment we performed together.

Lastly and certainly not the least, Meng-Chang Wu. We joined the lab together but ended up working on two separate projects. Although we never coincided on any project, we talked throughout our PhDs, and have had some very interesting conversations on a variety of topics.

I would also like to thank the groups of prof. Trey Porto and prof. Gretchen Campbell. They lent us many pieces of equipment from their labs and have been very helpful and cordial throughout my stay at JQI. Moreover, there have been times when I have borrowed experimental ideas directly from their labs. Although

there have been many more people with whom I have had positive interactions, and in one way or other they have enhanced my graduate school experience, it would be impractical to mention everyone personally. Hence, I would like to extend my thanks to the Physics department and the JQI especially.

Despite the wonderful interactions with many fantastic people, I have had difficult times in graduate school. Many days were very depressing, and in those days the support from my parents and grand-parents was miraculous for me. Especially my mom, with whom I have interacted the most in my life, and she has always supported me with everything I have done in my life. For their support and trust in me with everything I have done, I am dedicating this thesis to both my parents.

Table of Contents

List of Figures

List of Tables

Overview

Precision phase measurement has applications in a wide variety of areas including gravitational wave detection and biological imaging [1, 2]. Interferometers are devices used for phase measurements of an electromagnetic field. Phase measurements could be of two types. One is a measurement of a small phase disturbance around an otherwise fixed phase of light in an interferometer. The process is known as phase sensing. The other phase measurement process involves measuring a big unknown phase shift.

Historically, the Mach-Zehnder interferometer has been widely used for phase sensing. A classical Mach-Zehnder interferometer uses a coherent state of light. The sensitivity of a classical Mach-Zehnder interferometer provides a standard for phase sensitivity, known as the standard quantum limit (SQL). The phase sensitivity of an interferometer can be increased over the SQL using quantum mechanical states of light such as squeezed states [3, 4, 5] and photon number states [6, 7]. We refer to the phase sensitivity over the SQL as the phase super-sensitivity. Yurke et al. [8] suggested generating a squeezed state of light inside an interferometer instead of injecting it as an input to show phase super-sensitivity. The generation of squeezed states requires a nonlinear optical medium, hence the interferometer suggested by Yurke et al. is a nonlinear interferometer. Yurke et al. call this interferometer an SU(1,1) interferometer. The operation of an SU(1,1) interferometer can be described solely by transformations of the Lie algebra generators of the SU(1,1) group, hence the name SU(1,1)

interferometer. Similarly, a Mach-Zehnder interferometer is also known as an SU(2) interferometer as its working can be explained using the rotation of the angular momentum operators, which are the generators in the SU(2) group. We describe more on the naming in Chapter 3 and Appendix B. Recently, people have demonstrated an application of SU(1,1) interferometer in detection loss tolerant interferometry [9].

Experimentally, an SU(1,1) interferometer is scarcely explored. In 2014, Hudelist et al. [10] showed phase super-sensitivity. But their experiment did not show a direct signal to noise ratio measurement or direct measurement of the phase uncertainty. Very recently in 2017 and 2018, some groups have shown certain super-sensitive phase measurements with a few configurations of an SU(1,1) interferometer [9, 11]. In this thesis, we build on some of the existing theoretical work on SU(1,1) interferometers [8, 12, 13]. We analyze the sensitivity of different detection schemes in an SU(1,1) interferometer and determine the optimal detection scheme for an SU(1,1) interferometer. We suggest a variation on an SU(1,1) interferometer and show its phase super-sensitivity that matches the phase sensitivity of a traditional SU(1,1) interferometer. We call our variation a truncated SU(1,1) interferometer. The truncated version of an SU(1,1) interferometer greatly simplifies the experimental design by removing one of the two nonlinear devices present in an SU(1,1) interferometer; we explain this in Chapter 3. We also built an experimental setup for a truncated SU(1,1) interferometer and showed its phase super-sensitive behavior by demonstrating ≈4dB improvement in signal to noise ratio over the SQL.

Another kind of phase measurement process is a measurement of an unknown big phase shift, also known as adaptive phase measurement. Here instead of sensing a small phase variation around an otherwise fixed phase of light, one tries to measure a big phase shift in the light. In this limit, the approximation $\sin(\theta) \approx \theta$, where θ is the unknown phase shift, breaks down. An unknown phase is placed in one of the arms of an interferometer, and the phase is tracked with a controllable phase device in the other arm of the interferometer. The process requires adaptive algorithms to determine the phase applied to the controllable phase device in the interferometer, hence the name adaptive phase measurement. Here again, the use of quantum resources has provided a reduction in phase measurement error over the SQL [14, 15, 16]. Improvement in adaptive phase measurement has been shown with the use of a single-mode squeezed state [15, 16] and with the use of photon number states, though with post selection of data [17]. As per our understanding, no work in this area has been performed with the use of a two-mode squeezed state. In our work, we try to perform a big AC phase (~10 KHz bandwidth) measurement with our truncated SU(1,1) interferometer. We report the progress of our experimental setup and show some preliminary measurements in our setup.

Since an SU(1,1) interferometer generates a two-mode squeezed state for achieving phase super-sensitivity, we start our discussion with the introduction of squeezed states of light in Chapter 1. We describe the phase space representation of a squeezed state. We talk about the quadrature operators and discuss squeezing in these operators. We also provide a description for our four-wave

mixing experimental setup which we use to generate our two-mode squeezed state.

In Chapter 2, we discuss the measurement of quadrature operators with homodyne detectors. We describe homodyne detection and talk about various parameters involved in performing an accurate quadrature measurement. We also discuss various techniques we used to improve the measurement of squeezing in our experimental setup.

In Chapter 3, we describe an SU(1,1) interferometer in two different configurations namely a coherent seeded and a vacuum seeded configuration. We theoretically discuss the phase sensitivities of different detection schemes and provide optimal detection schemes in both the configurations. We theoretically analyze the truncated SU(1,1) interferometer and present experimental data on the phase sensitivities of the truncated SU(1,1) interferometer in both the coherent seeded and the vacuum-seeded configurations.

Finally, we mention our progress in performing an adaptive phase measurement with our truncated SU(1,1) interferometer. We discuss the concept of an adaptive phase measurement in greater detail. We provide the details of the experiment we have built for performing such a phase measurement and show some preliminary data.

1 Introduction

1.1 QUANTUM MECHANICAL LIGHT

We will start with the quantum mechanical representation of light, where we define the light using the annihilation (a) and the creation $(a^{\dagger})$ operators, which are complex conjugates of each other. We can define light using many representations, in this document we will mostly concern ourselves with the quadrature representation of light. For our purposes, the quadrature operators are very useful in phase measurement applications which we describe in Chapter 3 and 4. We can describe light using two orthogonal and non-commuting quadrature operators namely the amplitude and the phase quadratures [18].

$$X_{amp} = \frac{a + a^{\dagger}}{2} \tag{1.1}$$

and

$$X_{phase} = \frac{a - a^{\dagger}}{2i} \tag{1.2}$$

We can represent a general quadrature operator in the phase space using the below equation

$$X = \frac{ae^{i\phi} + a^{\dagger}e^{-i\phi}}{2}. \tag{1.3}$$

We can get a classical analogy by replacing the annihilation operator with the complex electric field and creation operator with the complex conjugate of the field.

The sine and the cosine terms of the electric field form a pair of orthogonal quadratures in classical wave optics.

For a bosonic system like light, the operators a and $a^{\dagger}$ are non-commuting with the commutator value given by $[a, a^{\dagger}] = 1$. The non-commuting property of the operators a and $a^{\dagger}$ can be written in terms of the amplitude and the phase quadrature operators, whose commutator is given by

$$[X_{amp}, X_{phase}] = \frac{i}{2}. \tag{1.4}$$

The Heisenberg relation for the uncertainty in the measurement of the two operators as a consequence of their non-commuting property

$$\Delta^2 X_{amp} * \Delta^2 X_{phase} \geq \frac{1}{4} \tag{1.5}$$

There are certain states of photons which satisfy the equality of the Heisenberg relation. Coherent beams and quadrature squeezed light are a few examples of them. We will discuss these in detail.

Before describing specific quantum states of light, we begin with a very helpful graphic description of the electro-magnetic (EM) field in phase space using the quadrature operators. Figure 1.1 shows the phase space representation of different beams. The stick in each plot represents the amplitude of the light, and the angle ϕ denotes the phase of the light. The direction along the line represents the amplitude quadrature (X_{amp}) of the light and the direction perpendicular to it presents the phase quadrature (X_{phase}).

1.2 SQUEEZED LIGHT

Before launching ourselves into the squeezed light description, we briefly introduce the coherent beam. As mentioned earlier, a coherent beam satisfies the Heisenberg uncertainty relation, such that the product equals ¼. Another important property of the coherent beam is that the noise of the two orthogonal quadratures operators are equal, with each being ½. Figure 1.1 (a) shows the phase space representation of a coherent beam, with the size of the ball being the same for the measurement operators along any direction [18] [19].

Like a coherent state, a squeezed state of light also satisfies the equality of the Heisenberg relation, i.e., the product of variance in two orthogonal quadratures equals 1/4. But unlike a coherent state, the variances in the orthogonal quadrature operators of a squeezed state are different, i.e., one of the quadratures becomes less noisy than the coherent beam noise at the expense of the other acquiring more noise. For a squeezed state, we can use this notation to represent the quadrature noise values:

$$\Delta^2 \mathrm{X}_{\mathrm{anti-sq}} = \mathrm{e}^{2\mathrm{r}}$$

$$\Delta^2 \mathrm{X}_{\mathrm{sq}} = \mathrm{e}^{-2\mathrm{r}}, \qquad (1.6)$$

where the parameter r defines the ellipticity of the noise ellipse in the Figure 1.1 (b) and (c). $\mathrm{X}_{\mathrm{anti-sq}}$ represents the anti-squeezed quadrature, and X_{sq}, the squeezed quadrature of the light. The quadrature along the stick in Figure 1.1 is the amplitude quadrature and the one perpendicular to it is the phase quadrature. Figure 1.1 (c) shows a phase squeezed state of light.

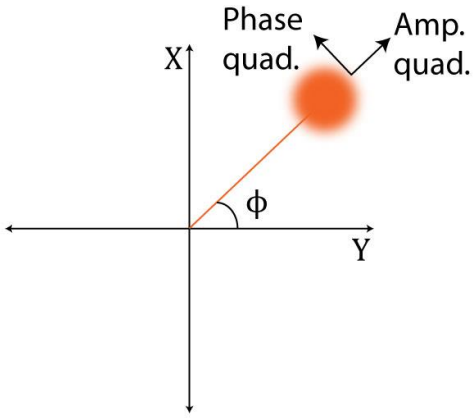

(a) coherent state of light.

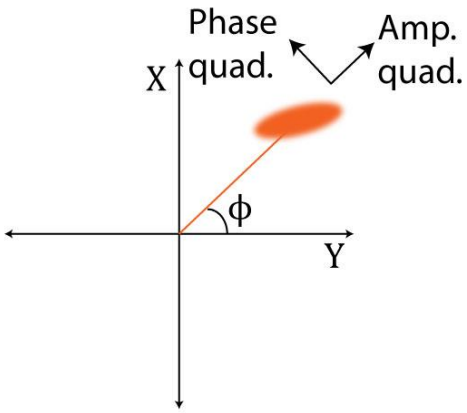

(b) squeezing in arbitrary quadrature.

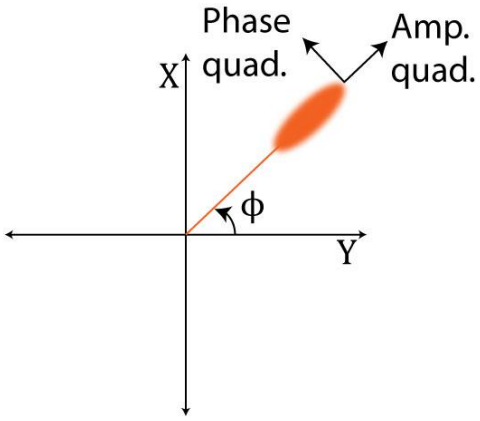

(c) phase quadrature squeezed state of light.

Figure 1.1: (a) Phase space representation of a coherent beam, and of squeezed light ((b) and (c)) with squeezing in different quadrature operators.

So far, we talked about the relationship between the amplitude and the phase quadrature of a single beam. But there could be states where a normalized combination of the quadrature operators of two or more beams shows a reduction in noise below the noise of a coherent beam, referred to as the shot noise limit (SNL). In this thesis, we will analyze a specific kind of beam known as a two-mode squeezed state. We call the two modes of the light, the probe, and the conjugate.

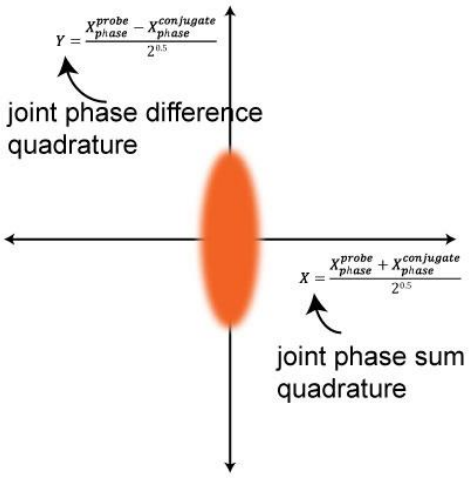

Figure 1.2: Phase space representation of joint quadrature noise of a two-mode squeezed state of light.

Figure 1.2 shows a phase space representation of a specific two-mode squeezed state. In our lab, we generate a two-mode squeezed state, which shows squeezing in the phase sum and the amplitude difference quadratures of the probe and the conjugate beams, and hence anti-squeezing in the phase difference and amplitude sum quadratures. The phase sum quadrature can be written as

$$\mathrm{X} = \frac{\mathrm{X}_{\mathrm{phase}}^{\mathrm{p}} + \mathrm{X}_{\mathrm{phase}}^{\mathrm{c}}}{\sqrt{2}} \qquad (1.7)$$

We can write other joint operators in a similar way as in equation (1.7). Next, we will proceed to the generation of the squeezed states of light, especially the two-mode squeezed light used in our experiments.

1.3 GENERATION OF TWO-MODE SQUEEZED LIGHT

There are multiple ways to produce a quadrature squeezed light beam. One very widely used method is the use of a 2nd order nonlinearity ($\chi^{(2)}$) in a birefringent

material (for example Lithium niobite, periodically poled KTiOPO4 crystal) inside a cavity. The device thus formed is known as an optical parametric oscillator (OPO). There is a significant amount of literature on the topic [20, 21, 22]. In this thesis, we will consider another source of squeezed light namely four-wave mixing (4WM). In our lab, we use a 4WM process in hot rubidium-85 (^{85}Rb) vapor, where we utilize the $\chi^{(3)}$ nonlinearity in the system [23, 24, 25]. In the process, as shown in Figure 1.3, we send a strong pump beam (≈795 nm) through a hot ^{85}Rb vapor cell, along with this we pass another beam 3 GHz down-shifted from the pump beam at an angle of ≈1^{o} with the pump beam. Using the $\chi^{(3)}$ nonlinearity, the medium amplifies the seed probe to give an output probe beam and, in the process, produces a conjugate beam (3 GHz upshifted from the pump beam) at an angle of ≈1^{o} with the pump beam (and ≈2^{o} with the probe beam). The angles are a result of the momentum and energy conservation process. The momentum and the energy conservation relationships for the pump, probe, and the conjugate photons are given by

$$2\vec{k}_{\text{pump}} = \vec{k}_{\text{probe}} + \vec{k}_{\text{conjugate}}, \tag{1.8}$$

$$2\omega_{\text{pump}} = \omega_{\text{probe}} + \omega_{\text{conjugate}}. \tag{1.9}$$

The 1^{o} angle is due to the differing refractive indices of the probe, conjugate, and the pump beams which otherwise would result in collinear beams.

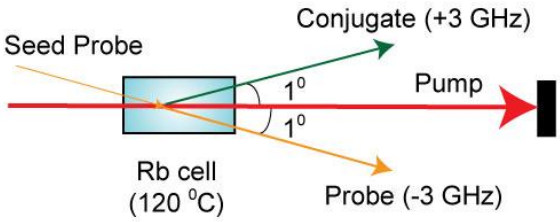

Figure 1.3: Experimental setup for producing a two-mode squeezed state of light.

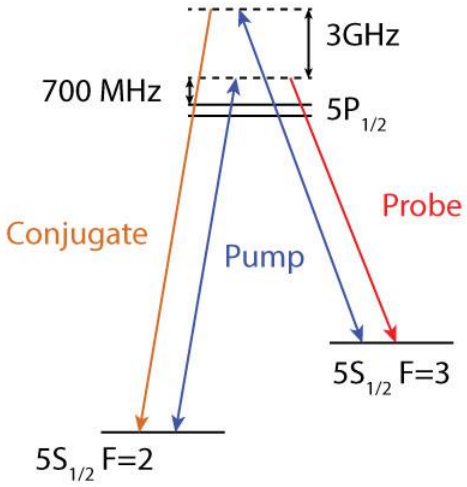

Figure 1.4: Energy level diagram of the Rb-85 atom, showing the process of 4WM to produce the twin beams.

Before moving further, we briefly describe the quantum mechanical process. See the references mentioned earlier for descriptive explanations [26, 23]. Figure 1.4 shows the energy level diagram of ^{85}Rb with the D1 transition line at 795 nm. We detune the pump beam almost 700 MHz blue to the D1 transition line, the process drives the transitions F=2 → F' and F=3 → F'', leading to the generation of the probe (3 GHz downshifted from the pump) and the conjugate (3 GHz upshifted from the pump).

The emission of a probe photon always accompanies the generation of a conjugate photon, and hence we call the pair twin beams. The photon pair is entangled in the quadrature space, giving quantum mechanical correlations. These quantum correlations provide sub-shot-noise fluctuations in the joint phase sum and the amplitude difference quadratures of the two beams. The reduction in quadrature noise below the SNL is the basis of the name of “two-mode squeezed” light. We will discuss more properties of the twin beams in the next section.

1.4 PROPERTIES OF LIGHT IN OUR EXPERIMENTAL SETUP

The probe and the conjugate produced in our experimental setup form a pair of two-mode squeezed light beams. Individually, these beams have bigger variances in quadrature space than a coherent beam. If the process of 4WM in Figure 1.3 is vacuum seeded, the two beams are thermal in nature and if the process is seeded with a coherent seed beam, the probe and the conjugate are displaced thermal beams, individually. Figure 1.5 shows the quadrature picture of the probe beam, generated with a seeded 4WM process, and its comparison with a coherent beam. In our setup, the excess noise of the probe (and the conjugate) beam over coherent beam noise depends on the gain of the 4WM process and increases with it. For a typical gain of 3 in our 4WM process, the excess noise is ≈7 dB, i.e., the probe beam noise is more than four times that of the coherent beam. The relationship between the excess probe (or the conjugate) noise over the quadrature noise of a coherent beam is given by

$$\Delta^2 \mathrm{X}^{\mathrm{probe}} = -1 + 2\mathrm{G}. \qquad (1.10)$$

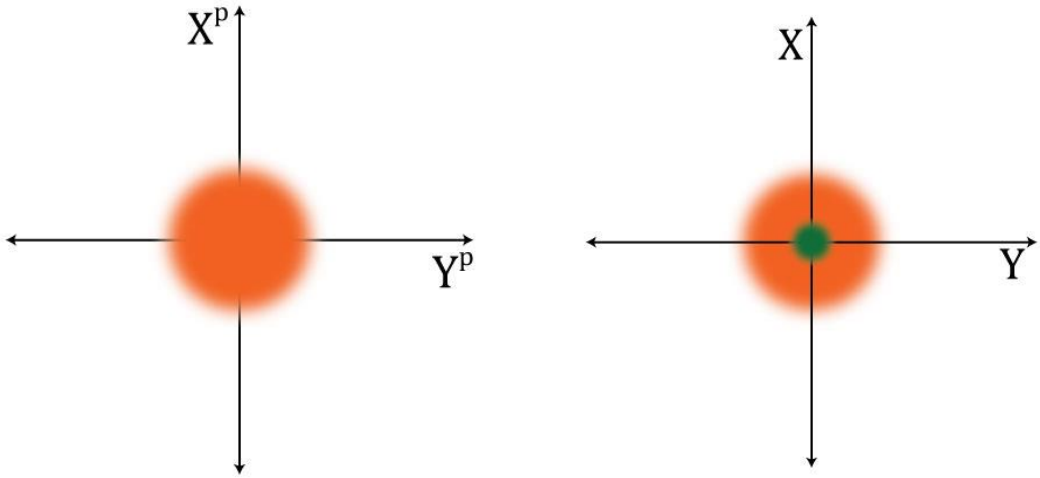

Figure 1.5: Phase space representation of the (a) probe beam and (b) probe beam (orange) and a coherent state (green).

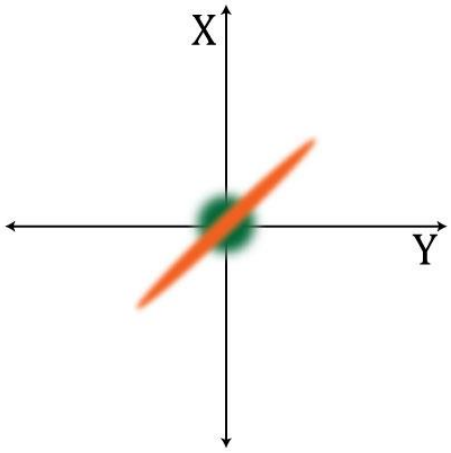

Figure 1.6: Phase space representation of joint quadratures of the probe and the conjugate beams (orange) and the SNL (green).

Having described the individual beam noise, we now discuss the joint quadrature measurement of the twin beams. In our 4WM process, the joint phase sum

quadrature has lower noise than the SNL, whereas the joint phase difference quadrature is the anti-squeezed one (Figure 1.6).

Having discussed squeezed states of light, their generation, and the uncertainties involved in the quadrature operator measurements, we now move on to the measurement of the squeezing in the quadrature noise.

1.5 MEASUREMENT OF A QUADRATURE OF LIGHT

The direct detection of light measures its power and does not give any phase information. To measure the light quadratures, we need phase as well as amplitude information. One method to do this uses homodyne detection. In a homodyne detector, the signal beam (whose quadrature we want to measure) overlaps with a strong local oscillator (LO), of the same frequency and spatial mode, on a 50:50 beam splitter (Figure 1.7). The outputs of the beam splitter are detected on two photo-diodes, and the resulting photocurrents are subtracted. The output is a quadrature term of the signal beam amplified by the amplitude of the local oscillator [18, 19, 20, 27]. We represent a signal beam with the annihilation and the creation operators $ae^{-i\theta}$ and $a^{\dagger}e^{i\theta}$, where θ is the phase of the field. We define the LO field classically with $|\alpha_{LO}|e^{i\theta_{LO}}$, where $|\alpha_{LO}|$ is the amplitude of the field and θ_{LO} is the phase. The output of the homodyne detector is given by

$$X = |\alpha_{LO}|\frac{ae^{-i(\theta-\theta_{LO})} + a^{\dagger}e^{i(\theta-\theta_{LO})}}{\sqrt{2}}, \qquad (1.11)$$

where $\frac{ae^{-i(\theta-\theta_{LO})}+a^{\dagger}e^{i(\theta-\theta_{LO})}}{\sqrt{2}}$ is a generalized quadrature of the signal beam. $|\alpha_{LO}|$ acts as a scalar amplification factor in the output.

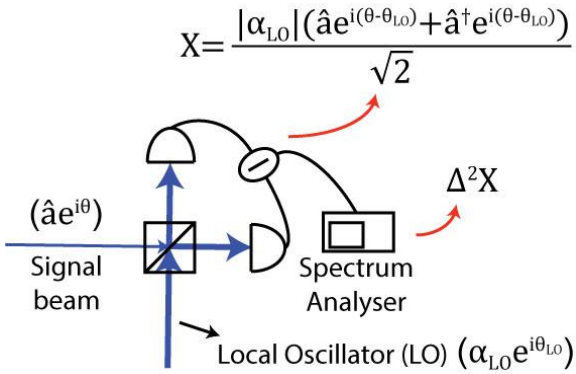

Figure 1.7: Homodyne detector for quadrature measurement. a and $a^{\dagger}$ are the annihilation and the creation operators of the signal beam. $|\alpha_{LO}|$ is the amplitude of the LO beam. θ and θ_{LO} are the phases of the signal beam and the LO respectively. $\frac{ae^{-i(\theta-\theta_{LO})}+a^{\dagger}e^{i(\theta-\theta_{LO})}}{\sqrt{2}}$ represents a generalized quadrature of the signal beam. The output of the homodyne detector is given by X.

The assumptions of a strong LO with the same spatial profile as the signal beam and the balance of the 50:50 splitter are important for accurately determining the quadrature term. Otherwise, the system will introduce loss or excess noise from extra terms in the output. We study the effect of these parameters later.

In our system, we have a two-mode squeezed state, and we care about the joint quadrature measurement instead of just a single beam quadrature. As seen earlier, the joint quadrature is just a linear combination of the quadratures of the twin beams. Hence, to measure it, we perform homodyne detection on each beam and then add (with or without an additional phase shift on each homodyne signal) the two output currents (Figure 1.8) [28, 26].

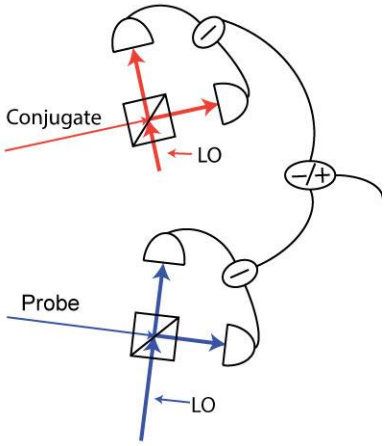

Figure 1.8: Joint homodyne detection setup for two-mode squeezed light.

For our system (assuming no optical loss), we can express the joint quadrature noise using the gain of the 4WM process and quadrature phases of the homodyne detectors on the probe and the conjugate as:

$$\Delta^2 X = -1 + 2G + 2\sqrt{G(G-1)}\cos\left(\theta^{probe} + \theta^{conjugate}\right), \qquad (1.12)$$

where θ^{probe} and $\theta^{conjugate}$ are the phase differences between the probe beam and its LO and likewise for the conjugate beam, respectively. We derive the above equation in Appendix B.

Figure 1.9(a) shows the theoretical simulation of the quadrature noise of lossless two-mode squeezed state of light as a function of probe beam quadrature phase, based on equation (1.11). While in Figure 1.9(b) we put our experimental data of squeezing. We see that the anti-squeezing and squeezing measurements do not have equal magnitudes. This is due to the presence of optical loss or the addition of excess noise from the experimental setup or from the generation process itself which we discuss in a later chapter. But, for the sake of this discussion, we can

see the phase dependence of noise in the theoretical simulation and the experiment as well.

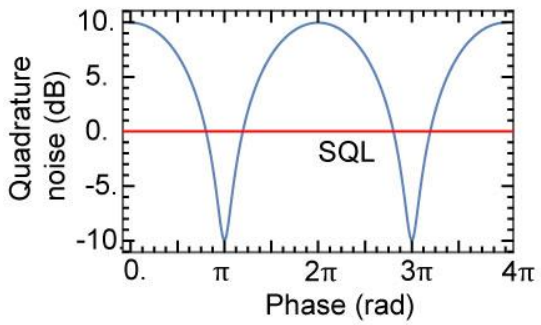

Figure 1.9a

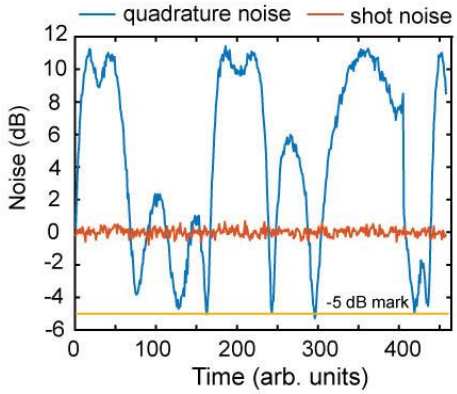

Figure 1.9b

Figure 1.9: (a) Theoretical simulation of the joint quadrature noise for a lossless two-mode squeezed state, (b) experimental observation of quadrature noise in our setup. The x-axis is time, and the phase changes irregularly due to experimental fluctuations. The data was taken by letting the phase of the beam freely run.

Having discussed the basic ingredients of squeezing and its measurement, we now discuss the factors affecting the measurement of squeezing, both in general and specific to our experimental setup.

2 Factors affecting the measurement of the squeezing of the noise

In this chapter, we examine the factors affecting the measurement of squeezing and some of the technical improvements made to the experimental 4WM setup.

Some of the main contributors affecting the squeezing measurement are the optical loss in the system and the imperfections in the detection system.

2.1 OPTICAL LOSS IN THE SYSTEM

As the probe and the conjugate beams traverse the system and the optical elements, they suffer the loss. The optical loss can happen through the process of scattering, absorption, or the change in polarization due to reflection or refraction through the optics. Loss reduces the correlations between the probe and the conjugate photons and hence reduces the measured squeezing. In our system, a major optical loss comes from the nonlinear medium itself. The probe beam in our system is close to an atomic resonance, as shown in Figure 2.1, falling within the doppler width, leading to an excess absorption on the beam.

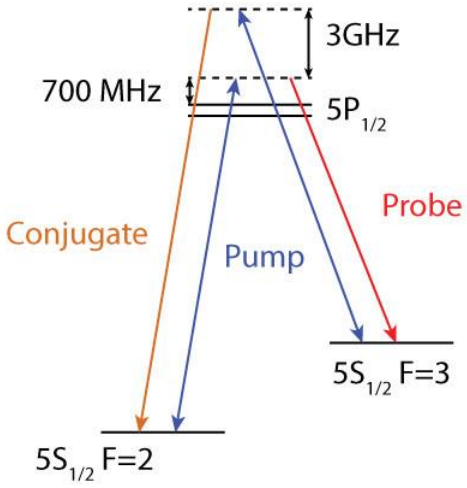

Figure 2.1: Energy level diagram for Rb-85.

Adding loss on the beams, the noise is given by

$$\Delta^2 X = -1 + (G-1)\eta^c + (G-1)\eta^p + 2\sqrt{G(G-1)}\cos(\theta^p + \theta^c) \qquad (2.1)$$

Here η^p and η^c are the transmittances of the probe and the conjugate beams respectively. The main effect of loss is to reduce the squeezing in the experiment, though it doesn't cause as much reduction in the anti-squeezing resulting in a squeezing plot which is not symmetric around the SNL (Figure 2.2). In this case, there is ≈5% extra loss on the probe beam than on the conjugate, this is because the probe frequency is closer to the atomic resonance.

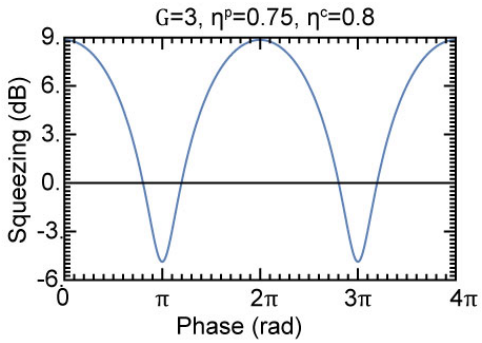

Figure 2.2: Joint quadrature noise in a lossy medium with the probe and the conjugate beam losses as indicated.

The important characterization here is the behavior of squeezing with the loss in the system. Figure 2.3 shows the variation of squeezing as a function of loss on the probe beam (the loss on the conjugate beam is 5% less, a typical experimental value). We can see reduction of squeezing as the loss in the system increases (transmittance decreases). In fact, optical loss is one of the biggest issues that limits the measured squeezing.

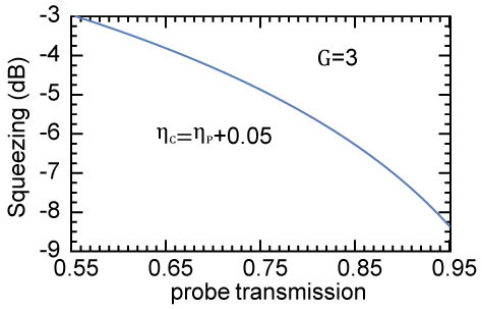

Figure 2.3: Squeezed quadrature noise as a function of optical loss on the probe beam.

The other source of loss is the detection loss. Sometimes a photon incident on a diode does not trigger an electron-hole pair, leading to the loss of the photon without detection. This can happen due to the reflection of the photon from the diode or transmission of the photon through the diode. In our experiment, we use

a diode with a responsivity $\rho \approx 0.626$ A/W at the wavelength of 795 nm. This translates to a detection efficiency of $\eta_{DE} \approx 0.98$ at this wavelength.

In a detector circuit, the current (i) produced in a diode, with a responsivity (ρ), by a light field with power (P) is given by:

$$i = \rho * P \tag{2.2}$$

The responsivity (ρ) of the diode is related to the detection efficiency (η_{DE}) of the diode by the expression:

$$\rho = \eta_{DE} * e * \frac{\lambda}{h * c} \tag{2.3}$$

where λ is the wavelength of light, c is the speed of light and h is Plank's constant.

2.2 IMPERFECTIONS IN HOMODYNE DETECTORS

As already seen, a homodyne detector gives a signal proportional to the quadrature of the signal beam and amplified by the amplitude of the LO. Experimentally, there are many things in a homodyne detector that one must account for to get an accurate result. We will now discuss those details.

2.2.1 50:50 beam splitter ratio

To measure the quadrature noise in our twin beams, we make a homodyne detector. As described earlier, in a homodyne detector, we overlap the signal beam (whose quadrature we want to measure) with a strong LO with the same frequency and spatial mode as the signal beam on a 50:50 beam splitter as shown in Figure 2.4. We detect the two beams thus obtained on two photodiodes and

subtract their photocurrent to obtain a signal proportional to the quadrature of the signal beam [18].

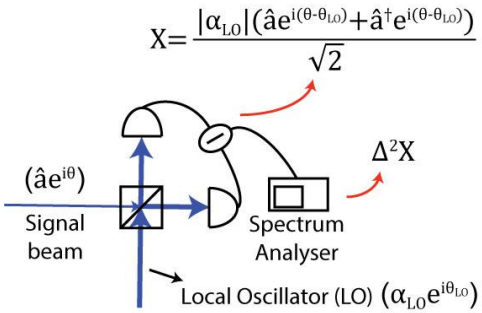

Figure 2.4: Homodyne detection set up as described in Figure 1.7.

Ideally, the beam splitter ratio should be 50:50, imperfections in the ratio add excess noise to our measurements of the squeezed quadrature. The excess noise added to the measurement can be represented by,

$$\Delta N = 1 + 16\delta^2\left(\frac{\Delta^2 A_{\text{probe LO}} + \Delta^2 A_{\text{conjugate LO}}}{\Delta^2 X_{\text{sig}}}\right), \qquad (2.4)$$

here $\Delta^2 A_{\text{probe LO}}, \Delta^2 A_{\text{conjugate LO}}$, $\Delta^2 X_{\text{sig}}$, and δ are the amplitude noise of the probe LO, the conjugate LO, the squeezed quadrature noise of the signal beam compared to the shot noise level (SNL), and the beam splitter imbalance, respectively. We derive equation (2.4) in Appendix A.

In our experiment, we use local oscillators generated using the same 4-wave mixing process as the twin beams. The process gives thermal (or at least pseudo-thermal) statistics to the photons in the LO beams. The thermal beams have higher noise compared to a coherent beam (shot noise level), and it depends on the gain

of the 4WM process. The amplitude quadrature noise of a thermal beam generated using the 4WM process and the 4WM gain (G) are related as,

$$\Delta \mathrm{X}_{\mathrm{amp}}^{2} = \Delta^{2}\mathrm{A} = 2\mathrm{G} - 1. \qquad (2.5)$$

The amplitude noise of the probe and the conjugate LOs, i.e., $\Delta^{2}\mathrm{A}_{\mathrm{probe\ LO}}$ and $\Delta^{2}\mathrm{A}_{\mathrm{conjugate\ LO}}$, are the same as their amplitude quadrature noise, i.e., $\Delta \mathrm{X}_{\mathrm{amp}}^{2} = \Delta^{2}\mathrm{A}_{\mathrm{probe\ LO}}$, and similarly for the conjugate LO. For our typical values of gain, the thermal beams have ≈7 dB excess noise over the SNL. Further, we can achieve a quadrature noise squeezing of ≈5 dB below the SNL in our setup. The difference in the thermal beam noise and the squeezed noise sets the ratio $\left(\frac{\Delta^{2}\mathrm{A}_{\mathrm{probe}} + \Delta^{2}\mathrm{A}_{\mathrm{conjugate}}}{\Delta^{2}\mathrm{X}_{\mathrm{sig}}}\right)$ in equation (2.4) to be ≈12 dB. We use this ratio to analyze the excess noise added to the squeezed quadrature as a function of beam splitter imbalance δ.

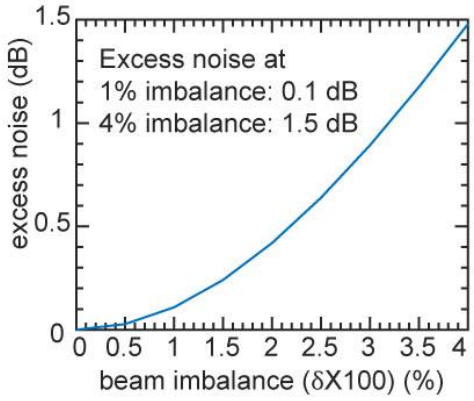

Figure 2.5: Excess noise in the joint squeezed quadrature as a function of imbalance of the probe and the conjugate beams. We used the same imbalance for both homodyne detectors.

Figure 2.5 shows that a 4% beam splitter imbalance can add an excess noise of ≈1.5 dB, while an imbalance of 1% or less does not affect the squeezing measurement significantly. As a precautionary note, the above simulation assumes 7dB excess noise in LO and nearly 5 dB of expected squeezing on the twin beams. If the experimental parameters change significantly, the above estimates may not be valid.

2.2.2 Imbalance in the LO oscillator power of the probe and the conjugate

To measure the joint quadrature of our twin beams we use individual balanced homodyne detectors for both the probe and the conjugate beams, and then we take their combination. The output of each homodyne detector is given by $A^pX(\theta)^p$ and $A^cX^c(\phi)$, where A^p and A^c are the amplitudes of the probe and the conjugate LOs, and $X^p(\theta)$ and $X^c(\phi)$ are the corresponding quadrature operators, respectively. Adding the photocurrents of the two homodyne detectors, we obtain

$$X^j = \frac{A^pX^p(\theta) + A^cX^c(\phi)}{\sqrt{2}} \qquad (2.6)$$

Now it is evident from equation (2.6) that to extract the joint quadrature we need $A^p = A^c$, i.e., the amplitudes of the two LOs should be equal.

One way to adjust the ratio of A^c and A^p is to use an electronic attenuator instead of adjusting the optical powers of the two LOs. We can electronically attenuate the homodyne signal with the larger LO power (usually probe homodyne detector in our system) to match the two signals.

One of the reasons, we study this here is that we produce our local oscillators using the same 4WM process used to produce the probe and the conjugate beams. To produce the LO, the 4WM process amplifies a weak seed in the probe beam path to produce the probe LO and simultaneously produces the conjugate LO. Since we seed the probe LO beam, there is always more power in the probe LO than the conjugate LO, the difference being equal to the power of the seed beam. When the 4WM gain is small, this difference could be significant compared to the powers of the LO beams, and thus can affect the measurement of squeezing substantially.

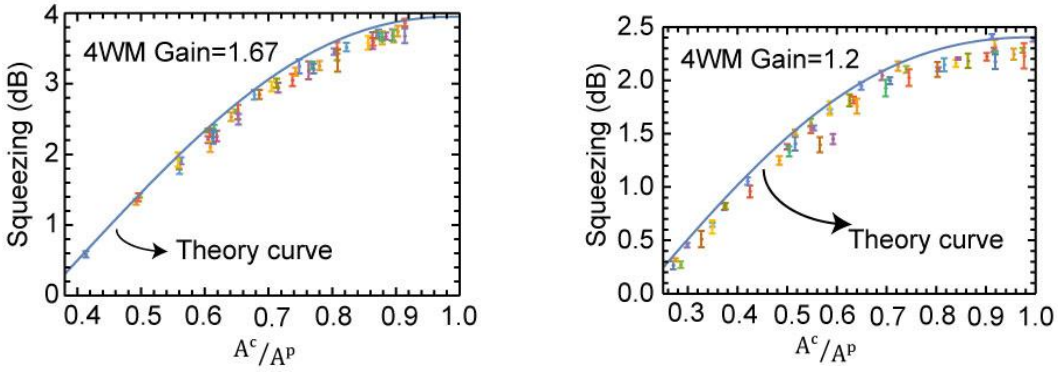

a b

Figure 2.6: Experimental data showing the variation of squeezing as a function of the difference between the powers of the two LOs.

Figure 2.6 shows the effect of the imbalance in power between the two local oscillators on the two-mode squeezing. We adjusted the $\frac{A^c}{A^p}$ ratio electronically to map the fall off in squeezing with imbalance. The data fits very well with theoretical estimations using the measured values for 4WM gain, the probe beam and the conjugate beam loss. Though one point to note here is that the theoretical plot lies

at the extreme end of the data. This is because measuring the squeezing requires our homodyne detectors to be locked to measure the phase quadrature of each beam. Noise in the locking gives extra fluctuations in the measurement of squeezed noise. The theoretical curves include only the gain and the loss parameters, but not the fluctuations due to the lock. Thus, the theory curves show the maximum possible squeezing at the present experimental conditions.

2.2.3 Electronic noise of the detector circuit

We use photodiodes to detect light. A diode produces a photo-current when light hits it, later this electric current goes through an electronic circuit which includes electrical elements, and then the signal passes through an amplifier, and finally, we measure the potential across a load.

Even with no incident light diodes produce some current. This “dark current” is the result of the random generation of electron-hole pairs in the depletion region of photodiodes. Another source of noise is the thermal noise of resistors in the detector circuit (Johnson noise). Both these noise sources are amplified and appear as the electronic noise in our measurement [29].

Additionally, some measuring devices like oscilloscopes themselves can have a bigger electronic noise floor than the photodetectors, adding to the overall noise, while RF spectrum analyzers usually have a very low noise floor. The addition of the noise from the two sources gives the total electronic noise floor.

This electronic noise floor adds excess noise to the quadrature noise and hence acts to reduce the measured value of squeezing [30]. The relationship between

this added measurement noise ($\Delta^2 N^{ele}$) and the separation of the electronic noise floor of the device from the measured signal (sep) is given by:

$$\Delta^2 N^{ele} = 10 * \mathrm{Log}_{10}\left(1 - 10^{-\frac{sep}{10}}\right) \mathrm{dB}. \quad (2.7)$$

Thus, the addition of this excess noise is independent of the 4WM process or the etangled beams and depends solely on the separation of the quadrature noise from the electronic noise floor. As can be seen in Figure 2.7, for our setup, a separation of ≈15 dB from the electronic noise is enough to make its contribution negligible.

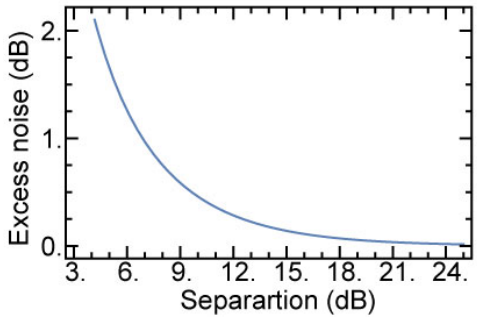

Figure 2.7: Excess noise added to the quadrature noise versus the separation of the measured quadrature noise from the electronic noise floor.

While one could increase the separation from the electronic noise floor by lowering the electronic noise of the detectors or the oscilloscopes, but this is difficult. Alternatively, the separation can be increased by increasing the optical powers in the two LO beams. The output of the homodyne detector is proportional to the amplitude of the LO beam. In our experiment, given the noise floor of the detectors and the other electrical circuits involved, ≈1 mW of optical power in both the probe

and the conjugate LO beams keeps the squeezed quadrature noise ≈15 dB above the electronic noise floor.

2.2.4 Visibility in the homodyne detectors

In a homodyne detector, we overlap the signal beam with a strong LO. We want the LO to have the same spatial mode as the signal beam to get the best matching. But in experiments, it is a difficult task to get identical modes. We mentioned earlier that we produce our LO in the same ^{85}Rb cell as the probe and the conjugate under very similar conditions. This ensures that the modes of the probe and the conjugate are similar to the modes of their LOs allowing us to achieve 98% fringe visibility in both of our homodyne detectors. We will see later that this efficiency (98%) limits the maximum squeezing in our experiment.

Homodyne detector visibility is a critical parameter in our experiments. Imperfect homodyne detector visibility is equivalent to an optical loss [20], in the same way as it is regarded in a Mach-Zehnder interferometer [31]. We can define homodyne detector visibility (ν) in terms of an equivalent optical transmission (η_{vis}) as

$$\eta_{\mathrm{vis}} = \nu^2. \qquad (2.8)$$

This can be incorporated with the loss in the rest of the optical system by the equation $\eta_{\mathrm{total}} = \eta_{\mathrm{rest}}\eta_{\mathrm{vis}}$, here η_{total} is the total optical transmission in the setup and η_{rest} denotes the transmission unrelated to visibility loss. Visibilities achieved in other squeezed light systems range from 0.99 to 0.997 [20, 27, 32, 33], although all these visibility values are for OPO systems, where the signal beam and the LO are both defined by a cavity.

Equation (2.8) holds under the assumption that the signal beam in the homodyne detector is a single spatial mode, i.e., the portion of the LO that is not overlapped with the signal beam coincides with vacuum only. In optical parametric oscillators (OPO), the squeezed light is produced from a cavity, and hence the light is spatially single mode, so equation (2.8) holds very well for an OPO system [20, 27, 32].

Although our 4WM system produces spatially multimode squeezing, i.e., the probe and the conjugate beams have multimode spatial structure, a single spatial mode on the probe beam is correlated with a specific spatial mode of the conjugate beam with no correlations with the other conjugate beam modes. Thus, if the overlap between the probe and its LO is not 100%, then the un-overlapped portion of the LO may encompass other spatial modes of the probe beam. These other modes of the probe will not be correlated with the conjugate modes overlapped with the conjugate LO. Moreover, these probe modes are thermal and have higher noise than vacuum. This results in excess noise in the quadrature measurement, which makes the situation worse than the case of a single mode squeezed beam from an OPO.

Now we analyze the effect of the excess noise due to reduced homodyne detector visibility on the squeezing measurement. Figure 2.8 shows how the squeezing in a two-mode squeezed state varies with the homodyne detector visibility for the case of vacuum coupling and independent thermal beam coupling in the parts of LO not overlapped with the probe and the conjugate. Clearly squeezing is lost much faster with visibility reduction if the probe and the conjugate beams are

surrounded by other thermal modes, i.e., in a multimode source like ours. The effect is unique to our experimental setup and not necessarily found in OPOs.

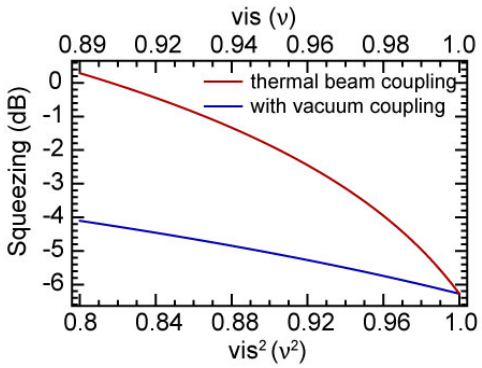

Figure 2.8: Squeezing as a function of loss due to visibility ($\nu^2 = \eta_{vis}$) for the two-mode squeezed light with thermal beam coupling (red) and vacuum coupling (blue) with the parts of the LO not overlapped with the probe and the conjugate beams. The plot assumes equal visibility in both the probe and the conjugate homodyne detectors.

We tried to experimentally verify the theory mentioned above. We made an experimental setup where we could change the visibility in the probe homodyne detector while keeping the conjugate homodyne detector visibility constant. We measured the two-mode squeezing as we changed the visibility of the probe homodyne detector. In the experiment, we use a mirror with three piezoelectric actuators to tilt the mirror in three different directions and hence change the visibility of the homodyne detector (Figure 2.9).

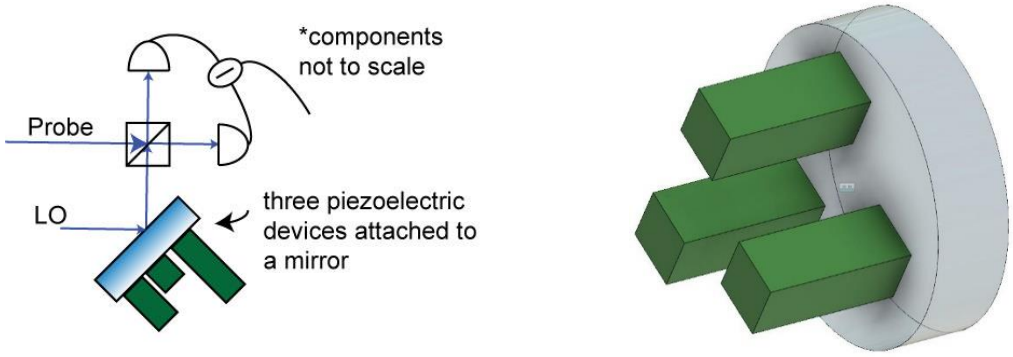

Figure 2.9: (a) Experimental setup for changing the visibility in a balanced homodyne detector. (b) A design of a 3-axis piezoelectric mirror

Before discussing the data from our experimental setup, we can understand a little more about our assumptions here. Earlier, we have said that any part of the LO which is not overlapped with the probe, overlaps other thermal modes uncorrelated with the conjugate beam. This causes excess noise in a joint quadrature measurement, and hence reduces the squeezing. The presence of other thermal modes in the probe homodyne detector should not affect the probe quadrature noise, as the entirety of the LO still overlaps with thermal modes with the same noise. Taking data for just the probe quadrature noise is much easier and less prone to experimental instabilities as the noise is independent of the phase in the homodyne detector.

Figure 2.10 shows the probe beam quadrature noise as we change the visibility in the detector by displacing the beam along different directions using the three piezos. We find that the quadrature noise is reduced as the visibility decreases. The orange curve on each plot shows the quadrature noise reduction as we change the visibility when assuming that the part of the LO not overlapped with the

probe beam couples to vacuum. The orange curves use the same experimental parameters (4WM gain, the probe and the conjugate beam losses) as were present when taking data. The change in experimental data is much slower than that of the orange curve, coupling only the vacuum. We can conclude that the part of the LO that doesn't overlap with the probe beam either overlaps with thermal modes that have less noise than the probe mode, or overlaps with a combination of thermal and vacuum modes. We understand the assumption about a lesser noise thermal mode by discussing our 4WM experimental setup. In our setup the pump beam is a Gaussian beam with spatially varying intensity profile. The different spatial parts of the pump beam produce distinct gains and hence probe beam modes with disparate noises.

We tried to understand the probe beam noise by obtaining plots where we assumed that the part of the LO not overlapped with the probe covers a combination of vacuum and a thermal mode with the same noise as the probe beam mode. The blue curves in Figure 2.10 are obtained with this assumption. We used the same experimental parameters as were kept for experimental data. The δ value in each of the figures represents the fraction of the thermal mode in the combination of the thermal and vacuum modes, which is almost 0.8, along every direction we displaced the beam to change the visibility.

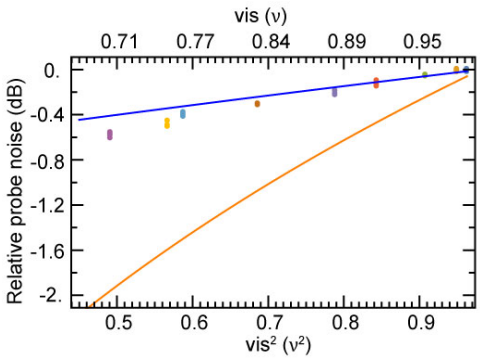

Piezo 1: $\delta = 0.75$

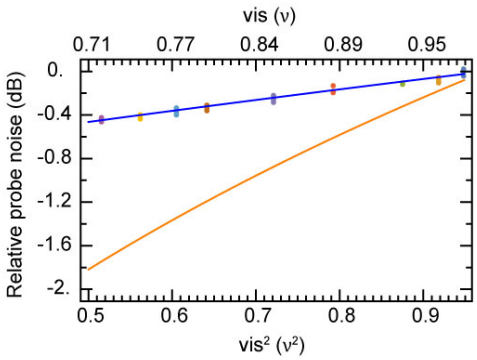

Piezo 2: $\delta = 0.8$

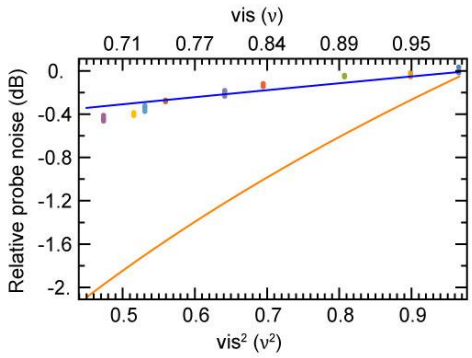

Piezo 3: $\delta = 0.75$

Figure 2.10: Probe beam quadrature noise as a function of visibility^2 in the homodyne detector, along three different directions of piezo tilt. The dots represent the experimental data points as we change the visibility of the probe homodyne detector. The blue curve is a theory fit with a δ fraction of the LO not overlapped with the probe beam coupling an independent thermal mode and the rest coming from vacuum. The orange part shows theory curve with vacuum coupling in the part of the LO separated from the probe beam.

After observing the probe quadrature noise, we move our attention to the squeezing in the joint quadrature. We take the squeezed quadrature noise data by changing the visibility of the homodyne detector in the same way mentioned earlier. We show our data in Figure 2.11. The left side figures are the absolute

noises of the squeezed quadrature taken from a spectrum analyzer (Keysight N9320), and the right side shows the squeezing below the shot noise level. To put a theory curve on the data, we use the assumption made earlier. We consider that the part of the LO not overlapped with the probe beam, because of less than unity visibility, covers a combination of vacuum and thermal modes uncorrelated to the conjugate beam. We place a theory curve on the absolute quadrature noise using the experimental parameters, the value of δ obtained from Figure 2.10, and a multiplicative factor to consider the total LO power (we find the multiplicative factor through a fitting algorithm). We find the theory fits very well with the data. Then we use the experimental parameters and the δ parameter to place a curve on the squeezing plots. The plot goes through the extreme end of the range of data points. This happens for the same reason mentioned in explaining the Figure 2.6. The squeezed quadrature noise is obtained by locking the homodyne detectors to measure the joint phase sum quadrature. The locking gives an extra error in the measurement and hence a slightly smaller value of the squeezing. The theory curves do not incorporate the locking error and hence show squeezing associated with the experimental parameters and the value of δ. The absolute noise plot, on the other hand, fits perfectly due to the use of the multiplicative factor.

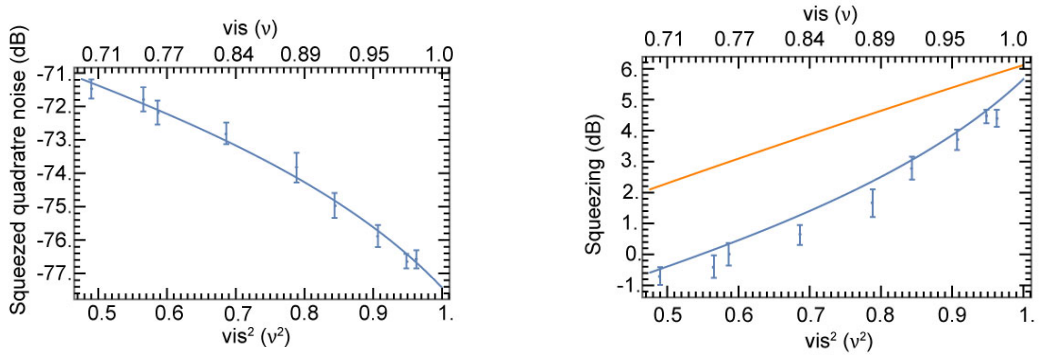

Piezo 1

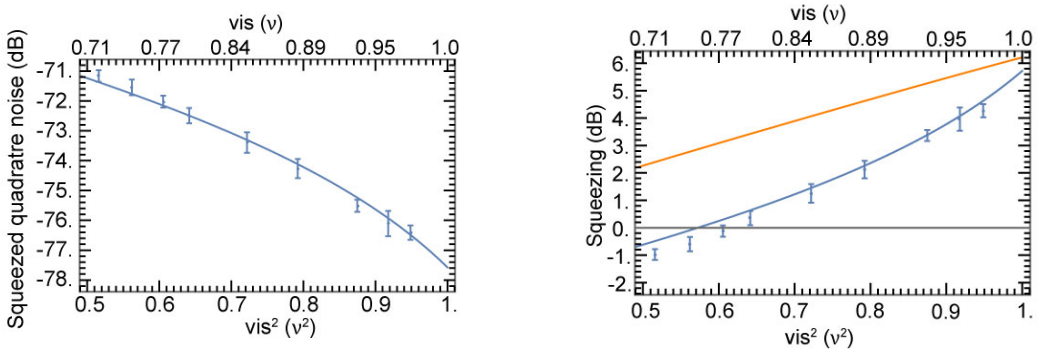

Piezo 2

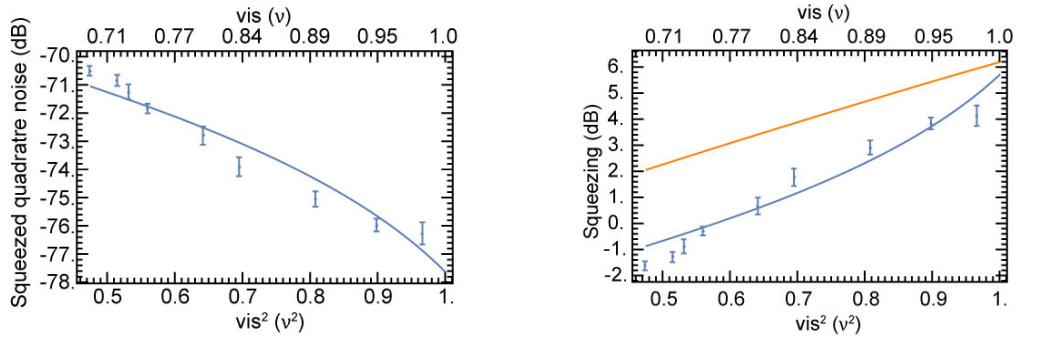

Piezo 3

Figure 2.11: Squeezed quadrature absolute noise (left figures) and squeezing (right) as a function of visibility^2, changed by piezo displacement in three different directions. The squeezing increases as we go up in the plots. The blue plot is a theoretical fit with a fraction (δ) of the LO that doesn't overlap with the probe beam coupling an independent thermal mode and the rest of the portion coupling vacuum. For each of the above plots, we estimate the value of the fraction δ using the experimental data in Figure 2.10 for the probe homodyne detector noise with the visibility in the detector, where we change the visibility by tilting the corresponding piezo electric device in a 3-axis piezo electric mirror. The visibility in the conjugate homodyne detector was maintained at 98%, and we assumed a coupling of an independent thermal mode in the part of the LO not overlapped with the conjugate beam. The orange curves show a theory where we couple vacuum in part of the LOs not overlapped with the probe beam and the conjugate beam in the two homodyne detectors. In calculating the theory curves, we used the experimentally estimated values of the 4WM gain and the optical loss.

The plots in Figure 2.10 and Figure 2.11 convincingly show that the loss of visibility in our homodyne detectors is far more detrimental to squeezing than it is in OPO systems. We simulate squeezing as a function of 4WM gain in Figure 2.12. We plot the expected squeezing at visibilities of 98% in both the probe and the conjugate homodyne detectors, with a coupling of uncorrelated thermal modes in the 2% part of the LO beams not overlapped with the probe and the conjugate beams (red curve). The blue curve has a coupling of 80% uncorrelated thermal mode and 20% vacuum in both the homodyne detectors, the proportions found in Figure 2.10 and Figure 2.11. The green curve considers perfect visibility in both the homodyne detectors and shows a monotonous increase in squeezing with the 4WM gain. Both the red and blue curves show a minimum noise (maximum squeezing) and then start to roll off. The maximum squeezing shown by the blue plot is very close to the best we have observed in our laboratory, as shown in Figure 1.9(b) in Chapter 1. We use a 15% loss on the probe and 10% on the conjugate beam while simulating these plots.

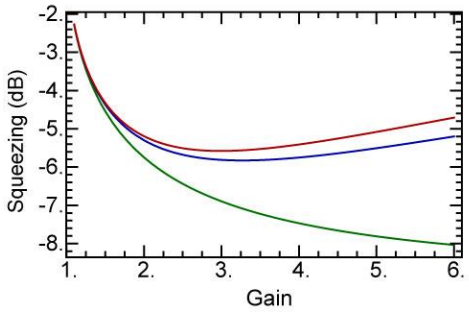

Figure 2.12: Squeezing as a function of gain. (Red) At a visibility of 0.98 in both the probe and the conjugate homodyne detector and considering only uncorrelated thermal beam coupling in the part of the LOs not overlapped with the probe and the conjugate beams. (Blue) Same as the red curve but with 80% coupling for the uncorrelated thermal modes and remaining 20% with vacuum modes, (Green) At perfect visibility.Here, we have taken the probe and the conjugate beam transmissions as: $\eta^{p} = 0.85$ and $\eta^{c} = 0.9$.

With due attention to our results, we can say that increasing the squeezing in our system requires us to improve the overlap of beams in our homodyne detectors. In a later section, we will discuss certain methods we have tried in our laboratory to increase the visibility in our detectors.

2.2.5 Phase noise in homodyne detectors

Another factor in measuring squeezing is the relative phase noise between the signal beam and its LO. We have seen that the different quadratures have different noises, which in a homodyne detector means that the relative phase between the LO and the signal beam affects the measured noise. If the relative phase in our detection is set to measure the squeezed quadrature, the presence of phase fluctuations will add excess noise from the anti-squeezed quadrature. If the measurement rate is slower than the phase noise, the output will be an average noise which is bigger than the squeezed noise and hence less squeezing.

Many groups performing squeezed light experiments with an OPO have reported phase noise in their experiments. Takeno et al. [20] reported a phase noise of ≈3.9^{o} in their detector, and they corrected it to ≈1.5^{o} which helped them increase their squeezing from 7 dB to 9 dB [20]. Suzukia et al. [33] reported a phase noise of 3.9^{o}. Vahlbruch et al. [27] have reported a phase of ≈1.7 mrad (=0.1^{o}), where they achieved a squeezing of ≈15 dB with their OPO system.

The effect of phase noise on two-mode squeezing can be derived from equation (2.1) and is given by

$$\Delta N = \left(X_{antSq} - X_{Sq}\right)\left(\frac{\Delta\theta^{p} + \Delta\theta^{c}}{4}\right). \quad (2.9)$$

where X_{antSq} and X_{Sq} are the noises of the anti-squeezed and the squeezed quadratures, and $\Delta\theta^{p}$ and $\Delta\theta^{c}$ are the phase noises in the probe and the conjugate homodyne detectors respectively. Equation (2.9) shows that the effect of phase noise rises with the difference between the noises of the squeezed quadrature and the anti-squeezed quadrature, which in turn is proportional to the gain and loss in the system. For many situations $X_{antSq} \gg X_{Sq}$, hence we can approximate equation (2.9) by

$$\Delta N = \left(X_{antSq}\right)\left(\frac{\Delta\theta^{p} + \Delta\theta^{c}}{4}\right). \quad (2.10)$$

Thus, the excess noise due to the phase fluctuations is mostly dependent on the anti-squeezed quadrature. Equation (2.9) can also be re-written in terms of gain and loss in the system as

$$\Delta N = \sqrt{G(G-1)}\eta^{p}\eta^{c}(\Delta\theta^{p} + \Delta\theta^{c}), \quad (2.11)$$

where G, η^{p}, and η^{c} are the 4WM gain, the probe, and the conjugate beams transmissions respectively.

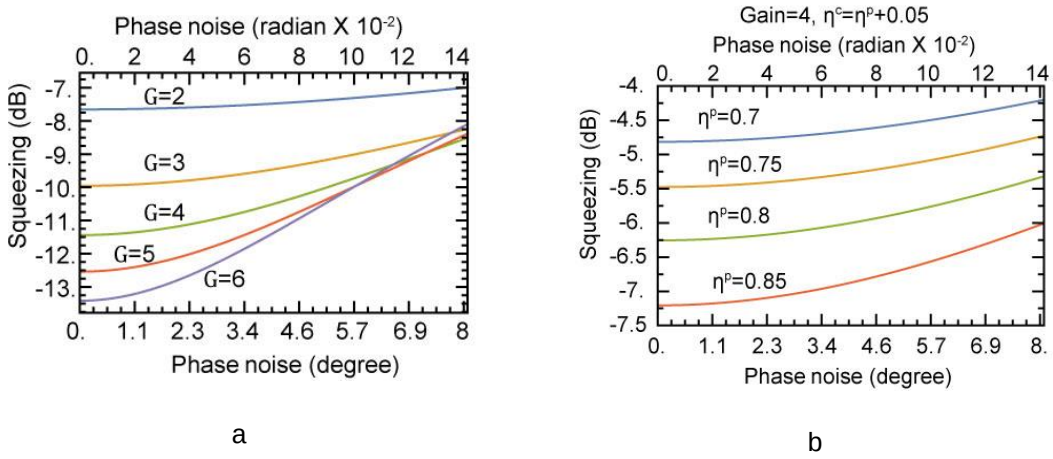

Figure 2.13: Variation of squeezing of two-mode squeezed light with phase noise, (a) for different 4WM gains and no optical loss, (b) at gain=4, and different losses on the twin beams with $\eta^c = \eta^p + 0.05$.

The effect of phase noise on squeezing (Figure 2.13 (a)) is far greater at high 4WM gain (resulting in higher anti-squeezed quadrature noise) than at lower values. At a 4WM gain of 4, a typical value in our experiment, we see the effect of phase noise with different levels of loss (Figure 2.13 (b)). This loss could be optical loss or excess noise addition due to the parameters discussed earlier. From both the figures, we see at a squeezing of ≈7 dB, a phase noise of ≈2.3^0 reduces the squeezing by ≈0.5 dB. We will refer to these figures and numbers later when comparing the experimental results.

To see the effect of phase noise in our experiment, we measured the phase fluctuations in our homodyne detectors. We made a homodyne detector with a probe (obtained from a seeded 4WM process) and overlapped it with a LO. To measure the phase noise of the homodyne detector, we lock the detector to the phase quadrature of the probe beam. We take the standard deviation of the output

of the homodyne detector and divide it by the slope of the signal at the phase quadrature, which is equal to the amplitude of the fringe pattern obtained by the overlap of the LO and the probe beam shown in Figure 2.14.

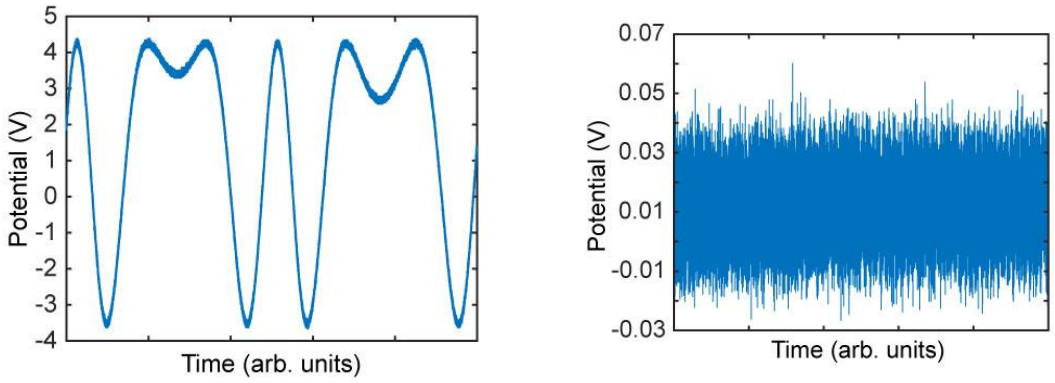

a b

Figure 2.14: (a) Fringes due to the overlap of the probe beam and its LO, while scanning a piezo mirror in the probe homodyne detector. (b) Signal with the homodyne detector locked to measure the phase quadrature of the probe beam.

We took several measurements similar to Figure 2.14 and given the stability of our lock we observe a range of phase noise values. Our best results were ≈0.23°, while poor locking yielded phase noise of ≈0.4° to ≈0.5°. We observe comparable results in the conjugate homodyne detector. Remembering that the joint quadrature noise depends on the sum of phases in the probe beam and the conjugate beam homodyne detectors (equation (2.1)), we found the sum could vary from 0.5° to 1° or a little worse with poor locking. From Figure 2.13 we conclude that even a poor lock does not limit our squeezing.

While many groups have shown [20, 27] that the squeezing in OPO systems is limited by the phase noise in the system, this is not the case for our 4WM system.

In fact, the other parameters the parameters are more important to our squeezing than this one.

One thing I would like to note here, while calculating the phase noise we did not subtract the thermal noise of the probe beam from the noise of the phase quadrature signal. That subtraction would have further (slightly) reduced our phase noise value, but because of our low phase fluctuations we ignored it. We can measure the thermal noise by blocking the seed of the 4WM process and taking the homodyne detector output. We can subtract the variance of thermal noise from the variance of the phase quadrature signal of the seeded probe to get the exact phase noise.

2.3 HELPFUL TECHNICAL MODIFICATIONS IN THE SETUP

Having discussed some of the technicalities that affect our squeezing and we now present improvements to get better noise squeezing.

2.3.1 Beam displacement due to piezo motion

As mentioned earlier, good squeezing requires good visibilities in our homodyne detectors. In our homodyne detectors, to control the phase of the light, we use a piezo controlled mirror.

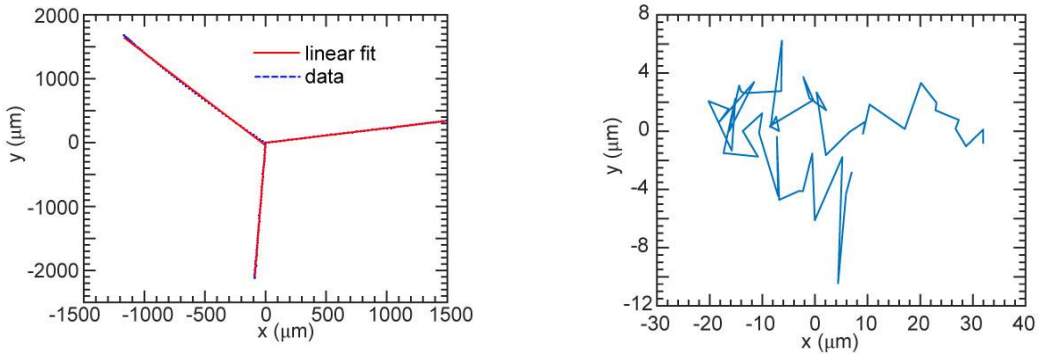

(a) (b)

Figure 2.15: Transverse displacement of the beam as the potential is applied to the three piezo actuators, shown in Figure 2.9, (a) individually, (b) potential applied to the three piezo together to minimize the orthogonal plane motion.

In our initial setup, we placed a piezoelectric mirror which had only one piezo actuator connected to the center of the mirror. While scanning we found it would tilt the beam causing the LO and the signal beam to separate which reduced the visibility and hence decreased the measured squeezing. The tilting or steering of the beam in transverse direction could happen due to deformations in the piezo causing a tilt in the mirror [34]. Despite our best efforts, this mirror driven by a single piezoelectric actuator could reduce our visibility from ≈98% to something below 93% which is not adequate for our purposes.

To reduce or eliminate this beam deflection, we used a mirror [34] with three piezoelectric actuators and applied potentials to the three of them together to minimize the deflection of the beam. Figure 2.15 (a) shows the movement of the beam in the cross-sectional plane, ≈1 m from the piezo mirror as we apply a potential across each of the piezos individually. We used this data to calibrate the

motion of the actuators which allows us to reduce the transverse tilt to ≈30 μrad, i.e., ≈30 μm transverse shift at ≈1m from the mirror, over the entire expansion length of the piezo actuators (Figure 2.15 (b)). The residual tilt is due to the small nonlinearity of the piezo actuators with the applied potential. We found that using the three-axis piezoelectric mirror with the correct proportions of potential kept the visibility within 1% across the entire range of motion.

2.3.2 Thermal fluctuations

We heat the ^{85}Rb cell to ≈120 ^{o}C to produce ^{85}Rb vapor inside the cell. The cell is insulated except for windows through which the light passes. This causes fluctuations in the temperature of the air around the windows and random changes in the refractive index of the air. This random variation in the index of refraction deflects the beam propagation direction randomly which in turn, varies the visibility in the homodyne detectors and hence changes the squeezing with time.

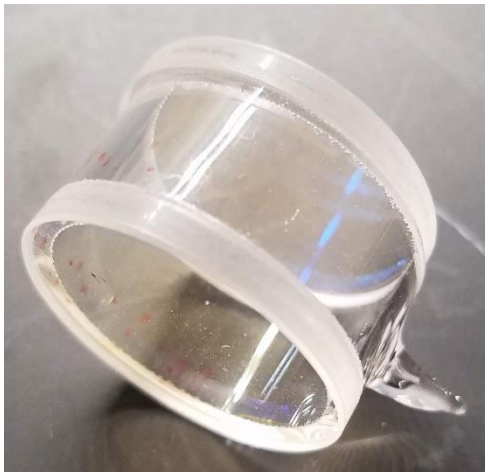

a

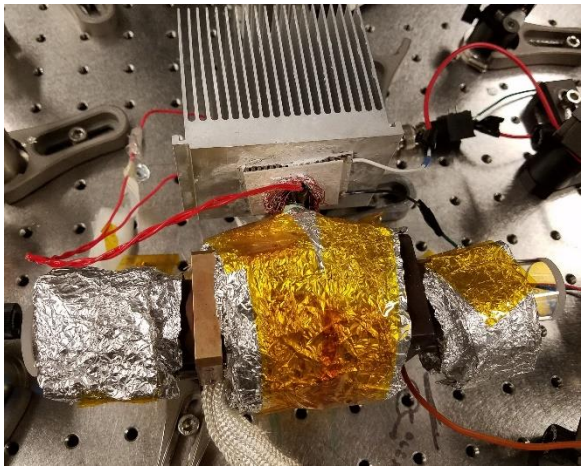

b

Figure 2.16: (a) The ^{85}Rb cell. (b) The ^{85}Rb cell with insulation and a temperature stabilizer keeping the temperature of the stem of the cell at a constant temperature, cooler than the windows of the cell.

We tried different geometries of insulation and heating in the cell and quantified the beam propagation fluctuations in those configurations. Here we present only four of those configurations including the one that worked the best. To examine the effect of thermal air currents around the cell, we pass a laser through each configuration and measure the transverse position of the beam at a distance of ≈0.5 m from the cells (Figure 2.18). As a baseline, we measured the beam path fluctuations in the transverse plane due to other optics in the system.

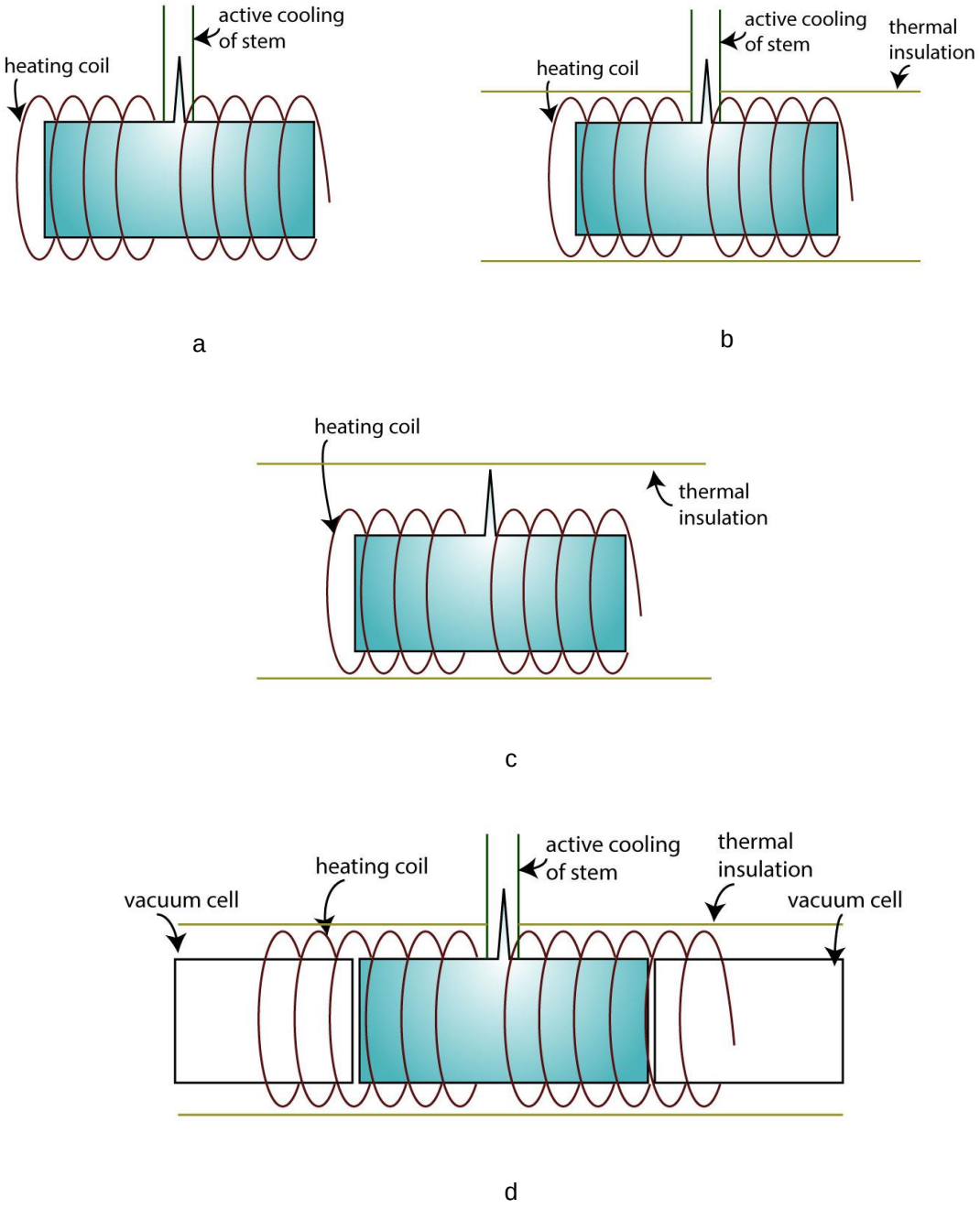

Figure 2.17: Configurations of cell placement in the setup. (a) Cell being heated with a heating coil and active cooling of the stem of the cell to keep Rb from getting deposited on the windows. (b) The cylindrical cell is insulated from the surrounding. (c) The lateral cell body is insulated from the surrounding, and there is no active cooling of the stem. (d) There are empty (with vacuum) cells on either side of the Rb cell and heating coil completely covering the air gaps between the cells.

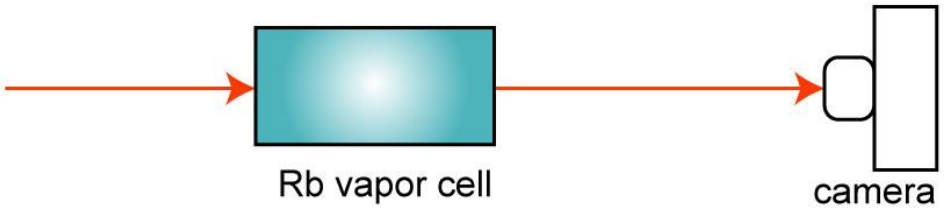

Figure 2.18: Experimental setup for measuring the beam propagation fluctuations around the vapor cell.

Table 1 shows the standard deviation of the beam motion. We see that insulation significantly reduces the random motion. Also, adding the vacuum cells to insulate the ^{85}Rb cell windows reduces the beam motion to the baseline level with no ^{85}Rb cell in the beam path. Figure 2.19 shows an example of the motion of the laser on a camera after it passes through the hot cell.

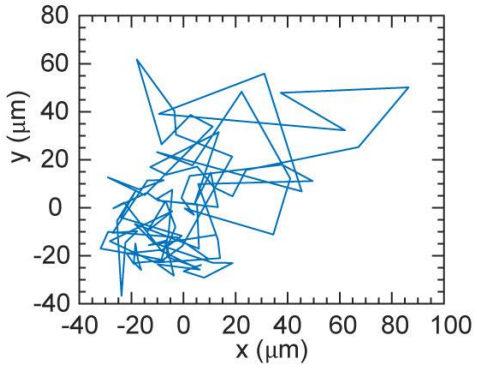

Figure 2.19: Random motion of beam in the cross-sectional plane as measured on a camera at ≈0.5 m from the ^{85}Rb cell.

Table 1: Standard deviations (one sigma) of random beam fluctuations along the two transverse directions for different configurations of cell wrapping, as shown in Figure 2.17. The uncertainties represent the one sigma error in the standard deviation.

	Temp. (^{o}C)	Stem Temp. (^{o}C)	ΔX (μm)	ΔY (μm)
No vapor cell		N/A	1.6(0.1)	1.6(0.1)
Configuration a (with active cooling of stem)	125	68	33.8(2)	24.8(3)
Configuration b (with active cooling of stem and thermal insulation)	120		6.2(0.8)	9(0.6)
Configuration c (no active cooling of stem)	135	N/A	7.8(0.6)	6(0.6)
Configuration d (with vacuum cells on the ends)	127	68	2.8(0.6)	2.4(0.4)

We also measured the effect of the cell temperature on the beam fluctuations for the configurations b and d in Figure 2.17 and found that the fluctuations increase with the temperature as expected (Figure 2.20).

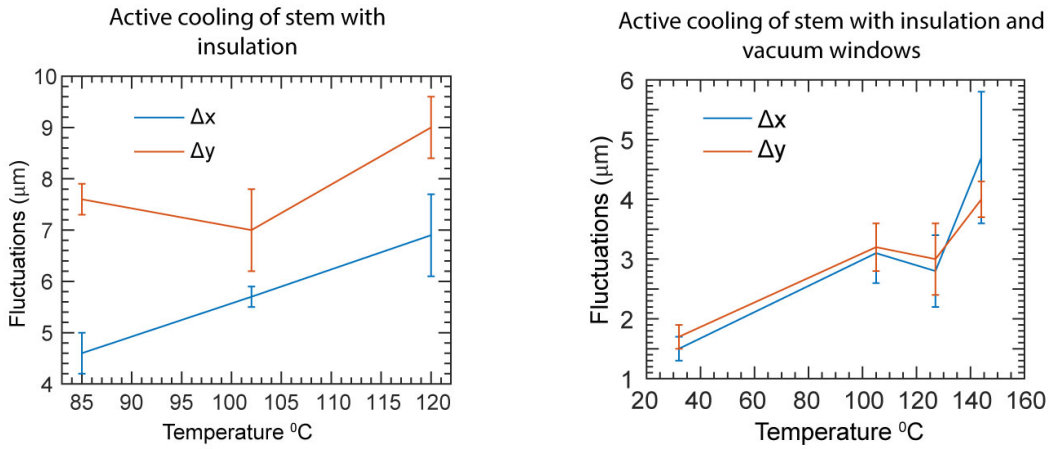

a b

Figure 2.20: Variation of the random motion of beam in the $x - y$ plane with temperature using cell wrapping (a) configuration b from Figure 2.17, and (b) configuration d from Figure 2.17.

The main takeaway here is that to reduce the random motion in the beams, we should insulate every surface of the cell. The vacuum cells of configuration d insulate the ^{85}Rb cell windows and hence provide the most beam stability compared to the other tested configurations. A downside of the configuration d is that it adds extra surfaces to the beam paths and increases optical loss, which reduces squeezing. We anti-reflection coat the surfaces to reduce the optical loss, to a total of ≈3% excess loss from 4 surfaces after the ^{85}Rb cell. Ultimately, adding a vacuum cell to get more stability at the expense of a little less squeezing is a tradeoff which depends on the application requirements. Another possibility would be to put the cell in a vacuum [35], which would eliminate the surrounding air and hence improve stability.

2.4 VISIBILITY IMPROVEMENT

As low visibility reduces our measured squeezing, and our best visibility was ≈98%, we saw that our squeezing was limited to less than 5.5 dB. To get better visibility, our probe beam (and the conjugate) should match the LO(s), both in phase front and in intensity profile. We tried a few approaches to make the beams similar in shape.

2.4.1 Mode shaping of beam with an SLM

One was to correct the shape of the beam using a spatial light modulator (SLM). Our earliest rationale was to disturb as little as possible the initial setup and do the beam correction. Correcting the shape of a beam with an SLM involved two different things, 1. Wavefront correction, 2. Intensity pattern correction.

2.4.2 Wavefront shaping of the beam

To do the beam correction, first we measured the Zernike modes of both the interfering beams. Zernike modes describe the various wavefront defects present in the beam wavefront using orthogonal mathematical terms. We used a Shack-Hartmann wavefront sensor to measure the wavefront of light and estimate the Zernike coefficients. We did this for both the beams and tried to match the Zernike modes of the LO beam to those of the probe beam using an SLM. Much of literature exists on similar techniques of wavefront correction [36, 37, 38, 39].

Before correcting the beam wavefront using an SLM, we first characterized the SLM, and then attempted to controllably modify the beam profile in the way we desired. The methodology to characterize the phase retardation imparted by the

SLM is in Appendix A. Just to put the number here, the total phase retardation provided by our SLM was 1.82π, the value is less than the desired value of 2π which is required for phase wrapping, i.e., applying a phase greater than 2π in multiples of 2π. Since we were correcting only a small amount of phase, we thought it was worth trying to use this SLM.

It is important to calibrate the phase put on the beams via the SLM using our wavefront sensor. We characterize the relationship between the Zernike coefficients induced by the SLM and the corresponding value given by the wavefront sensor. Since different Zernike polynomials are independent of each other, we can adjust a Zernike coefficient independently of other modes. We see this behavior in Figure 2.21 (a), where a change in 'vertical trefoil', a third order Zernike polynomial on the SLM, gives a change in the corresponding Zernike coefficient on the wavefront sensor. Though, if we look closely, we do find a small change in 'horizontal coma' and 'vertical astigmatism,' which are 3rd and 2nd order Zernike polynomials respectively. We attribute this mostly to the low resolution of the wavefront sensor and to some error in finding the exact image plane in the 4f imaging system due to the imperfections in the lenses. Figure 2.21 (b) shows the change in Zernike coefficient value on the wavefront sensor as we put the corresponding phase on the SLM. Though the behavior seems very linear, there is a small difference between the absolute slope of the 2nd order (three decreasing curves) and the 3rd order (four increasing curves) Zernike coefficients, this could again be attributed to the low resolution of the wavefront sensor and its comparatively smaller sensitivity towards higher order Zernike coefficients. The

reduced sensitivity of the wavefront sensor towards higher order Zernike coefficients is again shown in Figure 2.21 (c), where we find a slight decrease in the absolute slope of two of the 4^{th} order Zernike coefficients compared to the four 3^{rd} order coefficients.

Once we have characterized the phase retardation of the SLM, and found the relationship between the Zernike polynomial coefficients set on the SLM and those measured by the wavefront sensor, we correct the phase on an actual beam. To match the phasefronts of the probe and the LO, we reflect the LO off the SLM and detect both the LO and the probe beam on the wavefront sensor at the same place. The SLM plane forms an image at the wavefront sensor. The imaging allows us to feed the difference between the probe and the LO phases on the wavefront sensor directly to the SLM. We tried to follow this protocol by making two different setups, which we explain.

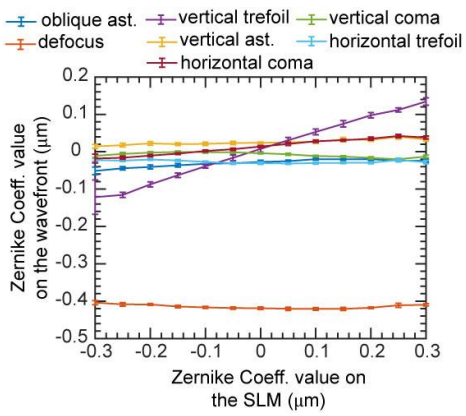

a

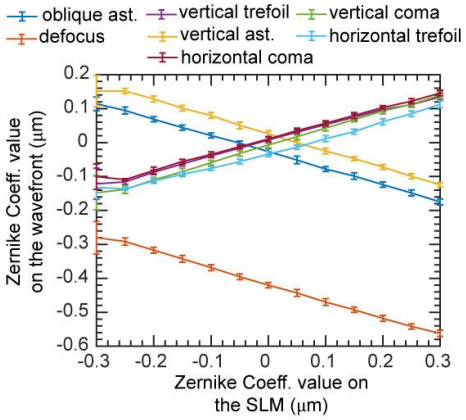

b

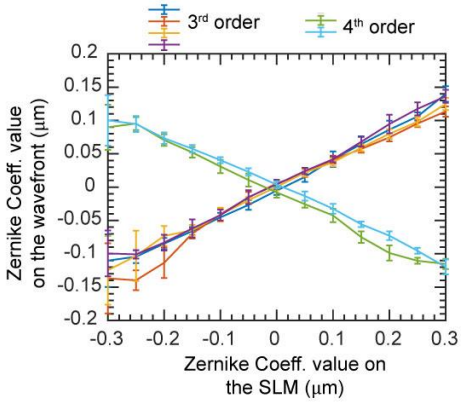

c

Figure 2.21: Calibration of the SLM and the wavefront sensor with the Zernike polynomials. (a) Coefficients of different Zernike modes measured on the wavefront sensor as we change the phase on the SLM by changing the coefficient of the 'vertical trefoil' term. (b) Variation of the coefficients of 2nd and 3rd Zernike modes observed on the wavefront sensor as we change the phase on the SLM by changing the coefficient of the corresponding Zernike mode. The coefficients of the 2nd order modes show a monotonic decrease whereas the coefficients of the 3rd order modes increase monotonically as we change the coefficients of the modes on the SLM. (c) Same as part (b), but for the 3rd and two of the 4th order Zernike modes. The curves display a slightly less sensitivity of the wavefront sensor in measuring the 4th order Zernike modes. The less sensitivity is shown by the reduced absolute slopes of the curves representing the 4th order modes compared to the curves of the 3rd order modes.

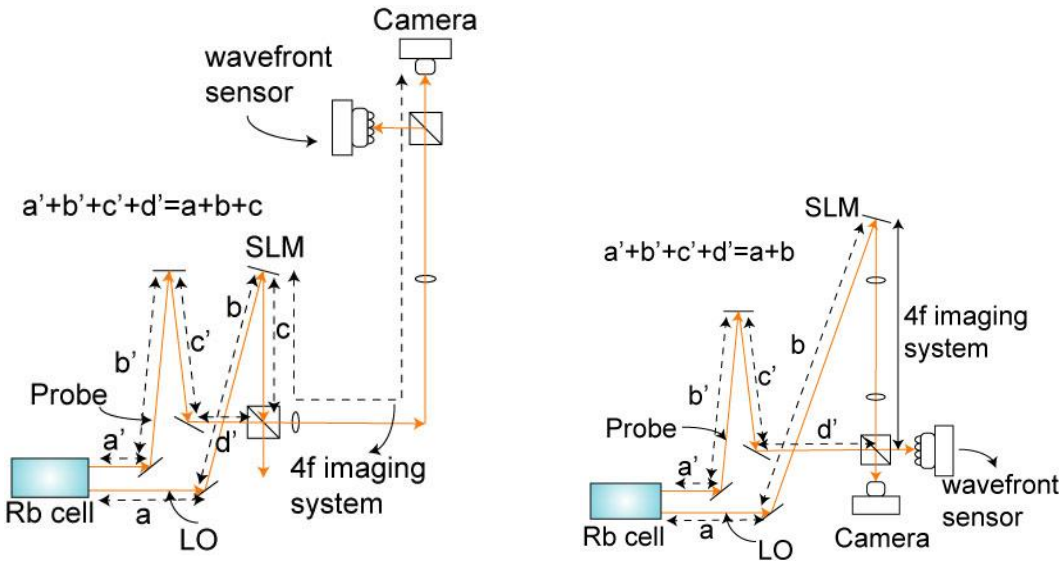

a b

Figure 2.22: Experimental setup for beam shaping with an SLM. (a) The path of the probe beam and the LO from the Rb cell to the 50:50 beam splitter are equal, and they are colinear after the beam splitter. The 4f imaging system images the beam shape at the SLM to the camera and the wavefront sensor. Here the length c is made large, and the focal lengths of the lenses placed for the 4f imaging system were 1m. (b) The path of the probe beam from the Rb cell to the 50:50 beam splitter is equal to the path traveled by the LO from the Rb cell to the SLM. The 4f imaging system images the beam shape at the SLM to the 50:50 beam splitter location. The camera and the wavefront sensor are placed right after the beam splitter.

As our first method of correction, we tried to avoid any distortion to our setup of homodyne detection. We made a 4f imaging system as shown in Figure 2.22(a). Here we image the SLM plane on the wavefront sensor. We place the two lenses of the imaging system after the 50:50 beam splitter where the LO coming from the SLM overlaps with the probe beam. The process avoids adding deformation due to the lenses and preserves the existing visibility of ≈97% with the probe. We measure the difference between the phase fronts of the probe and the LO at the

wavefront sensor and then feed the difference back to the SLM. We calculate the difference in terms of the Zernike coefficients and then feed them to the SLM. We repeat this process a few times until we get a minimum separation between the two wavefronts limited by the sensitivity of the system.

Figure 2.23 (a) shows the difference in the wavefronts of the LO and the probe beam as we iterate through successive corrective shapes on the SLM. The blue stems show the Zernike coefficient differences between the LO and the probe beam without any corrective pattern on the SLM. We must note that the surface of the SLM is never flat and introduces deformations of its own. Normally, one can correct for these deformations by forming a compensating pattern on the SLM. Since in our case, we did not have full 2π phase modulation from the SLM, we couldn't make such a compensating pattern. We kept our beam size much smaller than the SLM head and placed the beam near the center of the SLM head to reduce the deformation of the beam. In any case, the differences in Figure 2.23 (a) fluctuate around 0 as we make successive corrections. This is limited by the accuracy of the wavefront sensor. Figure 2.23 (b) shows the Zernike coeffcients of the pattern on the SLM, which becomes steady after a few iterations.

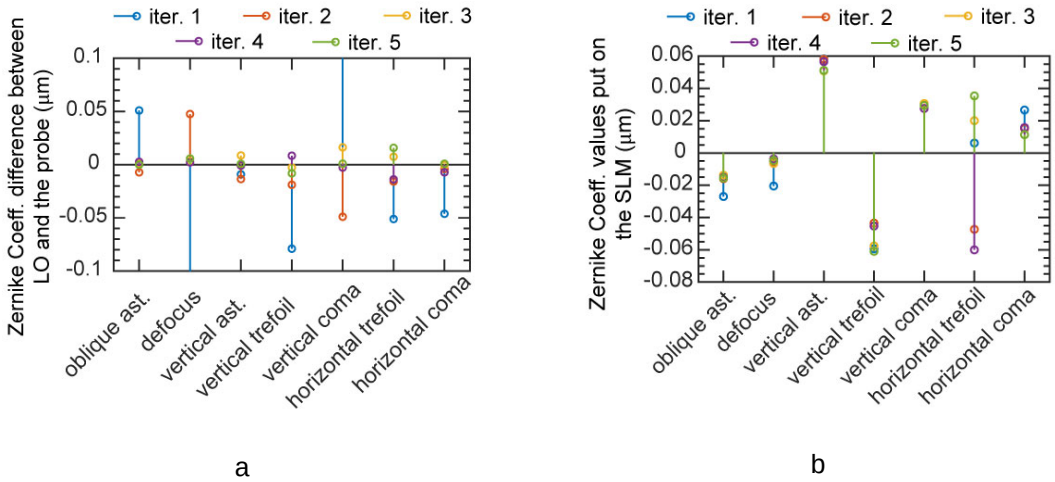

Figure 2.23: (a) Plot showing the difference in the Zernike coefficients of two beams at different iterations of the run. The blue stems are the first iteration showing the difference in the wavefronts of the two beams without any correction. (b) Stems showing the Zernike coefficient put on the SLM at different iterations. The colored stems indicate the iteration number in the adaptive algorithm.

Despite the convergence in our methodology, we didn't get much improvement in the visibility, and we didn't cross our threshold of 98 % which we achieve in the lab without any phase correction. Though we weren't sure exactly what stopped us from getting an improvement in visibility, we narrowed it down to some possibilities. One possibility was the use of the setup Figure 2.22(a) instead of Figure 2.22(b). In Figure 2.22(a), we made a 4f imaging system in which the beam splitter was placed at the very beginning of the imaging system. In the setup of Figure 2.22 (b), we know that the phase of the light is correct at the beam splitter as we provide our feedback by taking wavefront data right at that position. This setup too did not give us anything beyond 98% visibility, though we, again, were able to converge the Zernike coefficients as in Figure 2.23.

2.4.3 Intensity profile shaping of beam

The next possibility of not getting the improvement is due to the intensity pattern mismatch. So far, we had only matched the phase front of the beams and not the intensity pattern. Now, we will focus on just the intensity pattern modification. We used the methodology explained in Bagnoud et al. [40] to perform the intensity shaping. Here we use a phase-only SLM to create phase grating which is periodic along one direction with a period Λ and amplitude ϕ, as shown in Figure 2.24. The grating can be written as a convolution of a train of delta pulses with a rectangular function. $\otimes$ represents the convolution operator.

$$E = E_0 \sum_n \delta(x - n\Lambda) \bigotimes \mathrm{rect}_{\frac{\Lambda}{2}}(x) \exp j\phi_1,$$

and

$$E = E_0 \sum_n \delta(x - n\Lambda) \bigotimes \mathrm{rect}_{\frac{\Lambda}{2}}\left(x - \frac{\Lambda}{2}\right) \exp j\phi_2.$$

Here, $\mathrm{rect}_{\frac{\Lambda}{2}}(x)$ is a rectangular function with width $\frac{\Lambda}{2}$, and centered at $x = 0$. We observe the field at the focal point of a lens where it is given by the summation of the Fourier transforms of the above fields

$$E = E_0 \,\mathrm{sinc}\left(\frac{\pi\Lambda\nu}{2}\right) \cos\left(\frac{\Delta\phi}{2} + \frac{\phi\Lambda\nu}{2}\right) \exp\left(\frac{\phi_1 + \phi_2}{2} + \frac{\pi\Lambda\nu}{2}\right) \sum_n \delta\left(\nu - \frac{n}{\Lambda}\right). \qquad (2.12)$$

We place a pinhole at the center of the Fourier plane and allow only the central mode to pass. The field after the pinhole is given by

$$E = E_0 \operatorname{sinc}\left(\frac{\pi \Lambda \nu}{2}\right) \cos\left(\frac{\Delta\phi}{2}\right) \exp\left(\frac{\phi_1 + \phi_2}{2} + \frac{\pi \Lambda \nu}{2}\right), \qquad (2.13)$$

from which we can see that the amplitude of the field is modulated by the cosine term, i.e., $\cos\left(\frac{\Delta\phi}{2}\right)$. We note that, the methodology described here relies on the fact that we are removing the power from our initial state and never adding any extra power to it. This adds a constraint that we must start with a bigger beam than the final state.

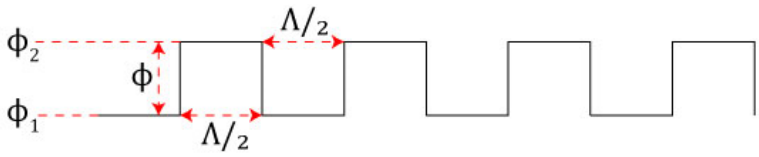

Figure 2.24: Phase grating for intensity modulation.

One more point we must note is that this method can be used for phase adjustment in addition to the intensity profile shaping. The phase adjustment can be performed by setting the desired value of $\frac{\phi_1+\phi_2}{2}$ while maintaining the required value $\Delta\phi$ for intensity profile shaping.

Though this method provides a way to modulate the phase and the intensity of a beam simultaneously and independently, one must understand its limitations. If we apply the above scheme using a spatial phase modulator, which produces a phase modulation from 0 to a value ϕ, then to get a full amplitude and phase profile shaping, the SLM should be able to satisfy the following minimum requirements

$$\left(\frac{\Delta\phi}{2}\right) \geq \frac{\pi}{2},$$

$$\frac{\pi}{2} \leq \frac{\phi_1 + \phi_2}{2} \leq \frac{5\pi}{2}. \qquad (2.14)$$

Solving the equations, we find that $\phi_2|_{\min} = 3\pi$, and $\phi_1|_{\min} = 1.5\pi$. This means that $\phi_{\min} = 3\pi$, i.e., an SLM should be able to provide a phase modulation of at least 3π.

We used the methodology described above to modulate the intensity of our beam and change its shape to the desired form. We obtained some positive results with regard to changing the shape of the beam, as shown in Figure 2.25. We shaped the LO intensity profile, shown in Figure 2.25 (a) to match the probe beam in Figure 2.25 (b). Our results are shown in Figure 2.25 (c, d, and e), where we show the final shape of the LO, and the convergences of the beam diameter to the values close to those of the probe beam.

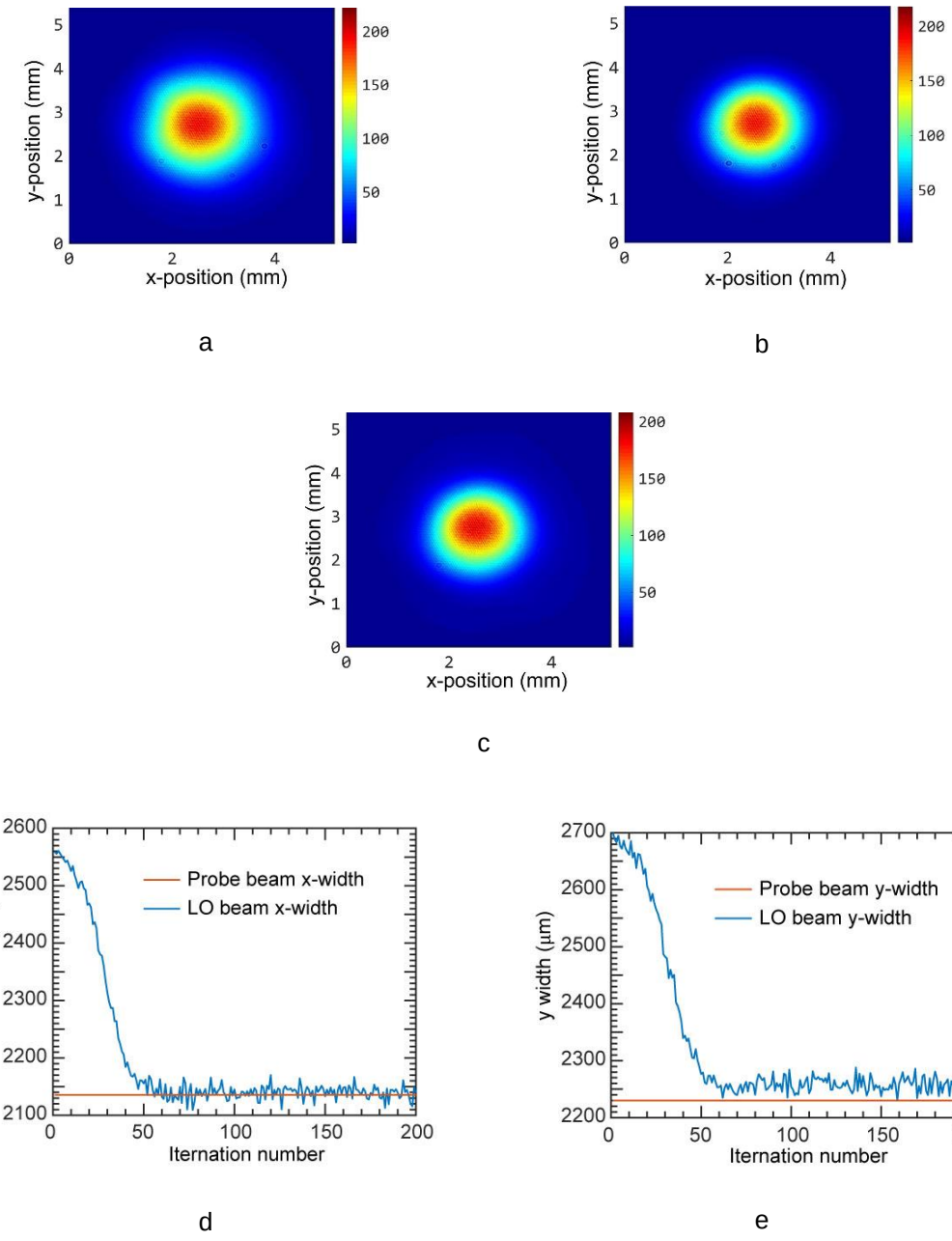

Figure 2.25: (a) The initial intensity pattern of the LO beam. (b) The intensity profile of the probe beam, this is the shape we want to match by shaping the LO. (c) The intensity pattern of the LO after the shaping of the beam with the method described earlier. (d) The convergence of the beam diameter of the LO along the x-direction, the orange curve shows the x-diameter of the probe beam. (e) The convergence of the beam diameter of the LO along the y-direction, the orange curve shows the y-diameter of the probe beam.

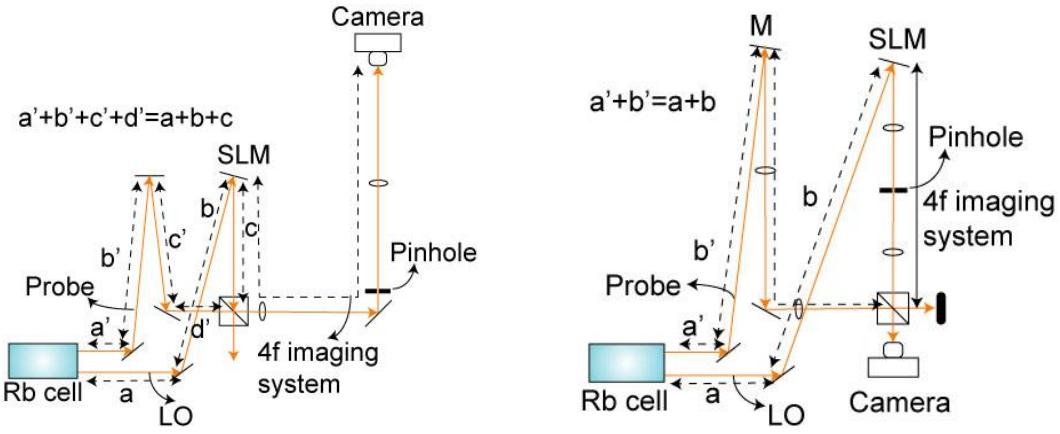

Figure 2.26: Experimental setups for intensity pattern correction. (a) The path of the probe beam and the LO from the Rb cell to the 50:50 beam splitter are equal, and they are colinear after the beam splitter. The 4f system images the beam shape at the SLM to the camera. (b) The path of the probe beam a'+b' is equal to the path traveled by the LO from the Rb cell to the SLM, i.e., a+b. The 4f system images the beam shape at the SLM to the 50:50 beam splitter location. There is a 4f system on the probe beam that images the mirror M on the 50:50 beam splitter, this considers any residual phase mismatch between the probe and the LO because of the imaging systems. The camera is placed right after the beam splitter.

Having successfully achieved the intensity shaping, we tried to incorporate this into our homodyne detector to observe any visibility improvement. We built our homodyne detectors using the two designs shown in Figure 2.26, similar to Figure 2.22. The first setup maintains the original homodyne detector apparatus and introduces the 4f imaging system and a pinhole for intensity shaping after the 50:50 beam splitter. The second assembly puts the 4f imaging system before 50:50 beam splitter. We make the 4f imaging system on both the probe and the LO to compensate for any residual imperfection from the lens system on both the beams. Though we achieved proper intensity shaping with both the beams, we

could not achieve a visibility better than 98% with just the intensity shaping with either of the setups.

The third step in shaping the beam was to combine both the intensity profiling and the wavefront correction of the beam simultaneously.

2.4.4 The simultaneous intensity and phase profiling

We applied both the intensity and the phase pattern correction, but we were not successful in increasing the phase visibility of our homodyne detectors. Here we will see the possible things that must be tried to improve the beam shaping. We show the wavefront difference between the LO and the probe beam in Figure 2.27 (a), by aligning them such that the phase difference between the two is minimized. We also show in Figure 2.27 (b) the intensity pattern of the two beams when we minimized the phase difference between the two beams. We see that, at the minimum phase difference position, the peaks of the two intensities are not aligned. We couldn't explain this behavior in our beams very well. Though with the algorithm presented earlier it is possible to correct any phase and intensity aberration, the imperfections present in our SLM (inability to provide 2π phase modulation) limit us from performing the phase and intensity modulation to the fullest extent. We have already shown that the minimum modulation necessary to achieve a full beam shaping with the algorithm is 3π without phase wrapping. When we tried to put a phase modulation requiring more than 2π phase shift using our SLM, it deformed our beam shape, and hence never gave any improvement in visibility.

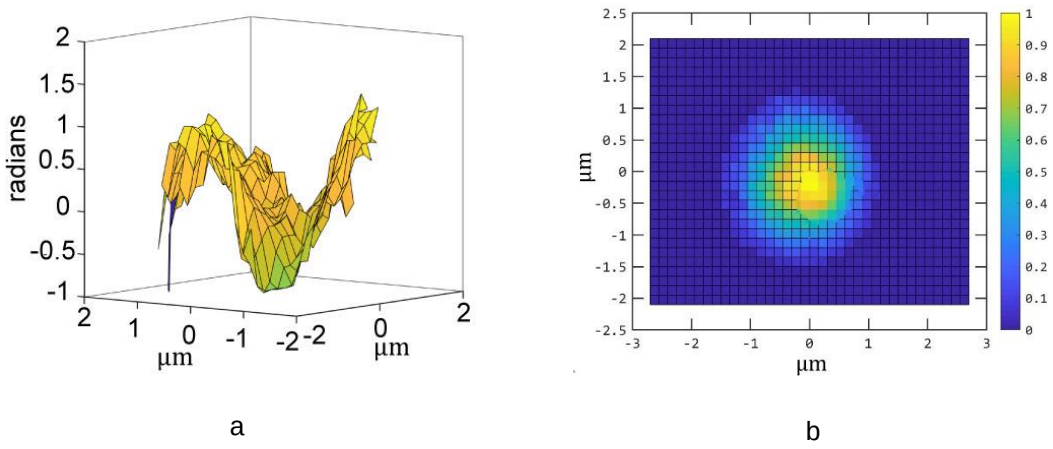

a b

Figure 2.27: (a) Wavefront difference between the LO and the probe beam. (b) Intensity pattern of the two beams when the wavefront difference between the two beams is minimized. The pattern with grid lines is for the LO beam, and the pattern without the grid lines is for the probe beam.

From our results we think, a better SLM should help get us improvement in beam shaping. Moreover, having a better resolution wavefront sensor would also help, as we have already seen in Figure 2.21 that the sensitivity of the wavefront sensor starts to fall for the 3rd or higher order Zernike polynomials. Also, it would be desirable to try more algorithms for matching the beam shapes and phase fronts [41, 42, 43].

3 Phase sensing with two-mode squeezed light

3.1 PHASE SENSING WITH A TRUNCATED SU(1,1) INTERFEROMETER

In this chapter, we will discuss the application of squeezed light in phase sensing, but first we will discuss phase sensing. Phase sensing has significant usage in biological applications and gravitational wave detection [2, 1]. Interferometers are used for phase sensing purposes. They are characterized by their phase sensitivities ($\Delta\phi$) defined by the smallest possible phase measurement that can be seen with the interferometer. It can also be defined as the uncertainty in a phase measurement with the interferometer. The phase sensitivity of an interferometer is limited by the number of photons (n) present inside the interferometer in a given measurement time interval. For a Mach-Zehnder interferometer, with a coherent beam with mean photon number n as input, the sensitivity is given by $\Delta\phi = 1/\sqrt{n}$ [3]. Figure 3.1 (b) shows the fringe pattern and associated noise in the measurement. The noise in the fringe pattern causes uncertainty in the phase measurement.

The sensitivity of the interferometers can be improved using quantum states such as squeezed states of light [3, 4, 5] and other resources, for instance, Fock states [6, 7, 17]. The quantum state is injected into these interferometers for improvement in phase sensitivity. Figure 3.1 (c) shows a Mach-Zehnder interferometer with a squeezed light input. The fringe pattern of the interferometer is shown in Figure 3.1(d), displaying reduced noise in the phase quadrature. The reduced noise allows improved phase sensitivity.

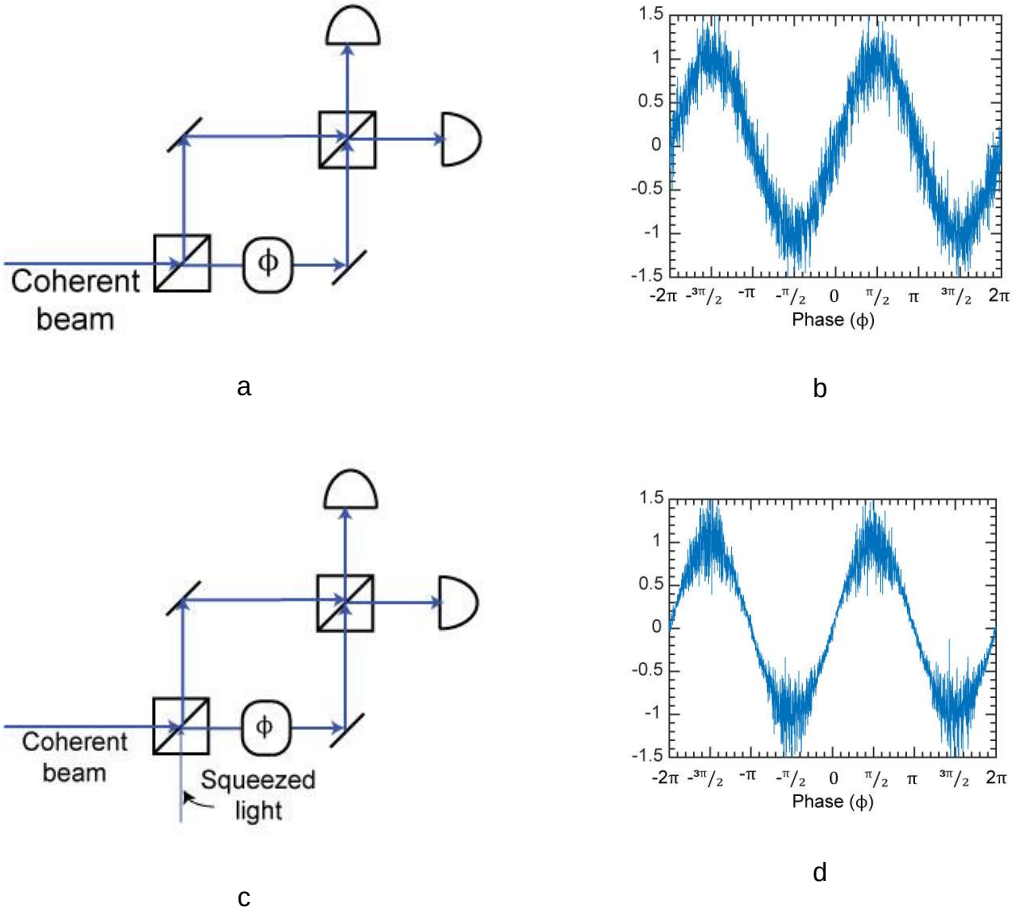

Figure 3.1: (a) Schematic of a Mach-Zehnder interferometer, (b) the power distribution measured at one of the detectors as a function of phase ϕ in a Mach-Zehnder interferometer. (c) A Mach-Zehnder interferometer with one of its inputs as phase quadrature squeezed light, (d) the fringe pattern of a Mach-Zehnder interferometer with the phase quadrature squeezed light input.

There is another class of interferometers where, instead of injecting squeezed light into the interferometer, a squeezed state is prepared inside the interferometer. An SU(1,1) interferometer, suggested by Yurke et al. [8] is one such kind of interferometer. An SU(1,1) interferometer is formed by replacing the beam splitters in a Mach-Zehnder interferometer with two nonlinear media [8], as shown in Figure 3.2. We mentioned earlier, the operations of an SU(1,1) interferometer can be described by the geometric transformations (rotation and Lorentzian boost) of

the operators acting as generators of SU(1,1) group. Hence the name SU(1,1) interferometer. See Appendix B for a brief Mathematics of the process.

The ultimate sensitivity of an interferometer can be quantified by the quantum Cramer-Rao bound (QCRB) [44, 45], which is given by $\Delta\phi \geq \frac{1}{\sqrt{\mathcal{F}_{\mathrm{Q}}}}$, where $\mathcal{F}_{\mathrm{Q}}$ is the Fisher information of the state inside the interferometer. Fisher information is a measure of the information in a statistical random variable and is used for estimating a parameter [46]. Given a quantum state, we can also define an upper bound on the Fisher information of an observable. We call this the quantum Fisher information (QFI) of the state, $\mathcal{F}_{\mathrm{Q}}$ [47]. The QFI depends only on the quantum state present inside the interferometer and the phase on the quantum state, and not on the detection scheme. The sensitivity of an interferometer depends on the chosen detection scheme as well as the QCRB of the internal quantum state. Given a detection scheme (and a measurement) the sensitivity of a device is limited by the classical Cramer-Rao bound (CCRB), given by $\Delta\phi \geq \frac{1}{\sqrt{\mathcal{F}_{\mathrm{c}}}}$, where $\mathcal{F}_{\mathrm{c}}$ is the classical Fisher information (CFI). The CFI depends on both the detection scheme and the quantum state of the light. For any detection scheme, the CFI is always less than or equal to the QFI of the quantum state that is used, i.e., $\mathcal{F}_{\mathrm{c}} \leq \mathcal{F}_{\mathrm{Q}}$.

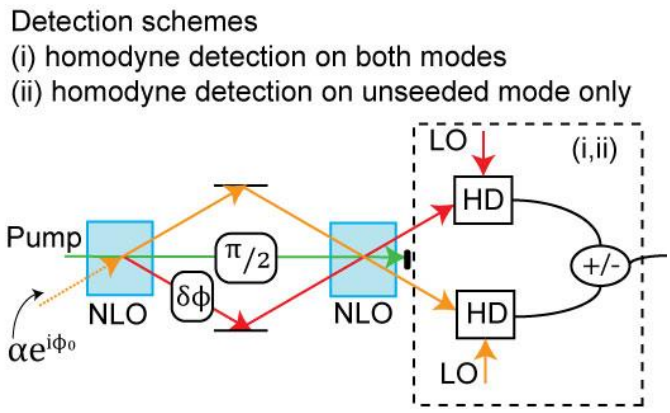

a

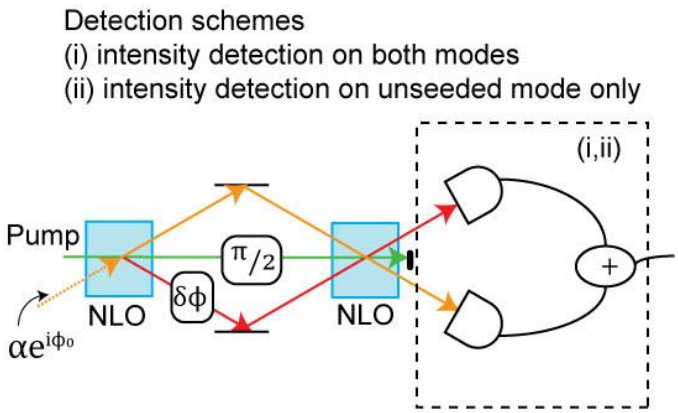

b

Figure 3.2: Schematics of an SU(1,1) type interferometer. A coherent state with amplitude α and phase ϕ_o, and a vacuum state $|0\rangle$ are mixed with a strong pump beam in a nonlinear optical (NLO) medium to produce a probe and a conjugate beam. The probe and the conjugate together form a two-mode squeezed state. A phase shift $\delta\phi$ is applied to the seeded arm, and the two beams are mixed with a pump beam in a nonlinear medium similar to the first one. The output of the 2nd nonlinear medium is measured, which is used to estimate $\delta\phi$. (a) The output after the 2nd NLO is measured with homodyne detection, (b) the output after the second NLO medium is measured using direct detection of power.

Since the above discussion tells us that the chosen detection scheme for an interferometer determines whether the phase sensitivity of the device reaches the

QCRB, we analyze different detection schemes for an SU(1,1) interferometer. Before probing the various detection schemes, we would like to understand the QFI of the quantum state present inside the SU(1,1) interferometer.

For a Gaussian state, the QFI can be calculated just with the information present in the covariance matrix of the state [48, 49]. For our experimental setup, we have a two-mode squeezed state system as our nonlinear medium in the SU(1,1) interferometer, shown in Figure 3.1. The NLO medium has two input modes, one of which we seed with a coherent beam with amplitude α and a mean photon number of $|\alpha|^2 \gg 1$, and the other one we leave empty, i.e., the vacuum mode goes through it. Under such situations, the output of the NLO is a two-mode squeezed state. For such a state, the QFI is given by equation (3.1) [50].

$$\mathcal{F}_{\mathrm{Q}} = 2\cosh^2(\mathrm{r})\left[(2|\alpha|^2 + 1)\cosh(2\mathrm{r}) - 1\right] \qquad (3.1)$$

Here r is related to the gain (G) of the NLO medium by $\mathrm{G} = \cosh^2 \mathrm{r}$. The output of the NLO medium is an amplified seed beam known as the probe, and in the other port, there is a conjugate beam. In the limit of $|\alpha|^2 \gg 1$, the mean probe photon number is given by $\mathrm{G}|\alpha|^2$ and that in the conjugate beam is given by $\mathrm{G}|\alpha|^2 - |\alpha|^2$. The two modes are quantum correlated or form a two-mode squeezed state when the gain is greater than 1, i.e., $\mathrm{G} > 1$ or $\mathrm{r} > 0$. The probe beam goes through a phase object, which puts a small phase offset on the beam, and then reaches the second NLO medium, similar to the first one. The conjugate directly goes to the second medium where it mixes with the probe and a strong $\frac{\pi}{2}$ phase-shifted pump beam. The output in the two modes after the second NLO medium depends on a

combination of the phases of the probe, conjugate and the pump beam acquired between the two NLO media. The phase combination is given by $\phi = 2\phi_{\text{pump}} - (\phi_{\text{probe}} + \phi_{\text{conjugate}})$. After the 2nd NLO medium, we measure the output using either direct detection or homodyne detection, and determine the phase shift $\delta\phi$ on the probe beam inside the interferometer. The limit of the phase uncertainty can be calculated using the QFI in equation (3.1), and the QCRB.

The phase sensing capacity of a device depends on the QFI of the state that senses the phase shift [50, 51]. We can consider the 2nd NLO medium as part of the detection system, as shown in Figure 3.3 which simplifies the setup of an SU(1,1) interferometer. We analyzed a setup where we could remove the 2nd NLO medium and still get the same sensitivity as the original SU(1,1) interferometer. We show one such setup in Figure 3.4 and compare the phase sensing capabilities of various detection methods below.

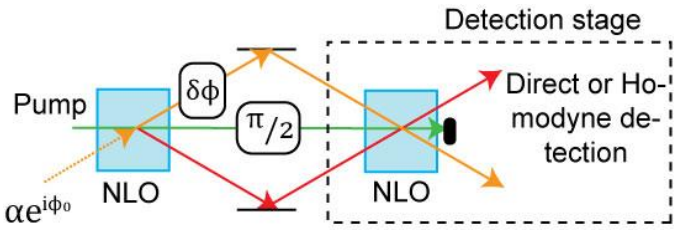

Figure 3.3: SU(1,1) interferometer displayed with the 2nd NLO medium as a part of the detection scheme. After the 2nd NLO medium, the beams can be measured either through the direct detection or using homodyne detectors.

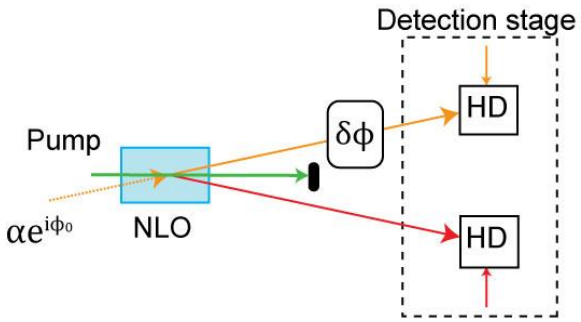

Figure 3.4: Truncated SU(1,1) interferometer with the 2nd cell replaced by homodyne detection on the probe and the conjugate beams.

Before analyzing the phase sensitivities of the various detection schemes, we can go through a few things about the classical Cramer-Rao bound. For Gaussian states (states with a Gaussian distribution in phase space), and Gaussian measurements (measurements with Gaussian distribution in outcomes), the CFI is given [48]:

$$\mathcal{F}_c = \frac{\left(\partial_\phi \langle \mathrm{M} \rangle\right)^2}{\Delta^2 \mathrm{M}} + \frac{2\left(\partial_\phi (\Delta \mathrm{M})\right)^2}{\Delta^2 \mathrm{M}}, \tag{3.2}$$

where $\partial_\phi \langle \mathrm{M} \rangle$ is the derivative of the mean of the measurement operator, $\partial_\phi (\Delta \mathrm{M})$ is the derivative of the standard deviation of the observable, and $\Delta^2 \mathrm{M}$ represents the error or variance in the measurement. In our setup, we have a two-mode squeezed state, which is a Gaussian state. Equation (3.2) is applicable for all the Gaussian measurements (like homodyne detection) on our two-mode squeezed state of light. Photon number measurement is not a Gaussian measurement and hence equation (3.2) is not applicable in this case. The above equation gives a method to determine the phase sensitivity of a device using a Gaussian state and making a Gaussian measurement.

3.2 STANDARD QUANTUM LIMIT

Before moving to various detection schemes, we define the standard quantum limit (SQL) against which we will compare our quantum improvements. We define the SQL as the sensitivity of a Mach-Zehnder interferometer with the same number of photons going through the phase object as in our device. For a Mach-Zehnder interferometer with n photons going through the phase object, the phase sensitivity is given by:

$$\Delta\phi = \frac{1}{2\sqrt{\mathrm{n}}}. \qquad (3.3)$$

3.3 DETECTION SCHEMES USING TWO-MODE SQUEEZED LIGHT

There are two different configurations of an SU(1,1) interferometer, (i) a coherent beam seeded interferometer, and (ii) a vacuum seeded interferometer. We will discuss different detection schemes in both configurations.

3.3.1 Seeded interferometry

We put a coherent seed in the 1st NLO medium, which gives a pair of twin beams. The NLO medium amplifies the seed to give a probe beam, and a conjugate beam is produced in the process. Together these beams form a two-mode squeezed state. We send the probe beam through a phase object giving it a small phase shift $\delta\phi$. Later, the probe is mixed with the conjugate beam and a pump beam in another NLO medium similar to the first medium. The output after the 2nd NLO medium depends on the combined phase of the twin beams and the pump, given by $\Delta\phi = 2\phi_{\mathrm{pump}} - (\phi_{\mathrm{probe}} + \phi_{\mathrm{conjugate}})$. We use the output of the 2nd NLO medium to

determine the phase shift $\delta\phi$ on the probe. We can perform number detection on either one or both of the beams. Otherwise, we can also perform a joint quadrature measurement on the beams to determine the phase.

Before talking about different measurements, we represent the state of light at various points in the interferometer using different annihilation (and creation) operators, as shown in Figure 3.5. We derived the analytical expressions for the different operators involved in an SU(1,1) interferometer in Heisenberg picture using the formalism described in [52, 53]. See Appendix B for more details. We used the analytical expressions thus derived in estimating the phase sensitivities of different detection methods in an SU(1,1) interferometer. We note here that in all the following discussions we keep the gain of the 2nd NLO medium the same as the first unless otherwise specified.

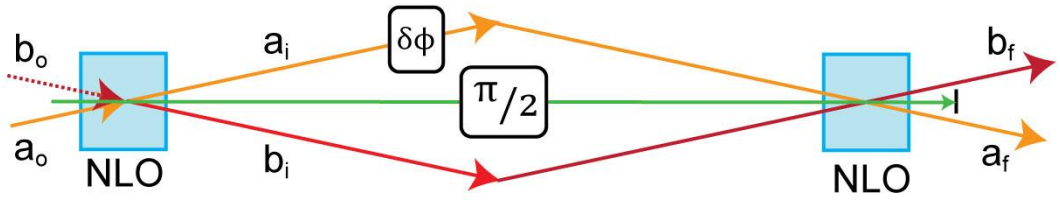

Figure 3.5: Schematic of an SU(1,1) interferometer with the operator representation of various states of light.

3.3.1.1 Photon number measurement

We can measure the total photon number after the 2nd NLO medium to estimate the phase. We represent the measurement by $M_N = a_f^\dagger a_f + b_f^\dagger b_f$. The phase sensitivity of the detection method can be expressed by [53]:

$$\Delta^2\phi = \frac{\cosh^4(2r)\left[\cosh(8r)\sec^2\left(\frac{\phi}{2}\right) + \csc^2\left(\frac{\phi}{2}\right)\right] - 8}{4|\alpha|^2}, \tag{3.4}$$

where r is the squeezing parameter of the NLO, related to the gain of the medium by $G = \cosh^2(r)$, ϕ is the acquired phase inside the interferometer, represented by $\phi = 2\phi_{pump} - \phi_{probe} - \phi_{conjugate}$, and $|\alpha|^2$ is the mean photon number in the coherent seed. Using equation (3.4), we find that the phase ϕ for minimum uncertainty is given by:

$$\phi_{opt} = 2\cot^{-1}\left[\sqrt[4]{\cosh(8r)}\right], \tag{3.5}$$

where the optimal sensitivity is

$$\Delta^2\phi_{opt} = \frac{\left[2\cosh(4r) + \sqrt{\cosh(8r)} - 1\right]\cosh^4(2r)}{2|\alpha|^2}. \tag{3.6}$$

We plot equation (3.4), normalized by the seed photon number $|\alpha|^2$, as a function of phase ϕ in Figure 3.6. We see the phase sensitivity with the measurement of M_N optimizes at a certain phase point ϕ. Unfortunately, Figure 3.6 does not show any quantum improvement with the measurement of M_N. We plot the optimal sensitivity of the operator M_N with the 4WM gain in Figure 3.7 where we find that the optimal sensitivity with M_N beats the SQL (solid black line) only with a 4WM gain greater ~4.5. Additionally, we also observe that the sensitivity using the total photon counting operator, M_N, never reaches the QCRB (solid red line) of a two-mode squeezed state for any 4WM gain. Hence, we can say that the total photon number, i.e., M_N is a non-optimal measurement for phase sensing in a seeded SU(1,1) interferometer.

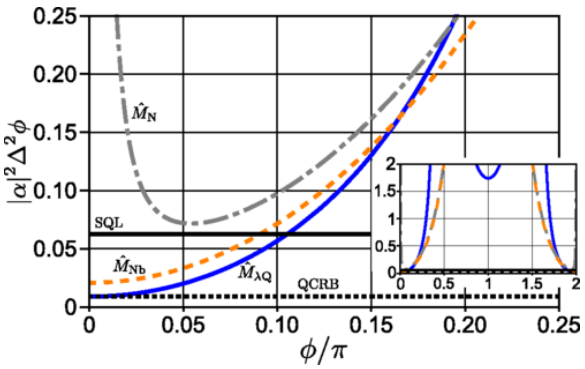

Figure 3.6: Normalized sensitivity of a lossless SU(1,1) interferometer with the phase ($\phi = 2\phi_{\text{pump}} - \phi_{\text{probe}} - \phi_{\text{conjugate}}$) of the interferometer with various detection schemes. The black dotted line is the quantum Cramer-Rao bound for the two-mode squeezed state. The solid black line represents the SQL. The gray dashed-dotted line shows the sensitivity of the measurement M_N in equation (3.4), the solid blue curve shows the phase sensitivity for the optimized quadrature measurement $M_{Q\lambda}$. The sensitivity of the photon number measurement in the b_f mode, i.e., M_{Nb}, is given by the orange dashed curve.

Another detection method is to measure the photon number only in one of the output modes. We can measure either the photon numbers in the a_f or the b_f mode. Both the outputs individually depend on the phase inside the interferometer. We represent the two measurements by $M_{Na} = a_f^\dagger a_f$ and $M_{Nb} = b_f^\dagger b_f$.

For the detection scheme, M_{Nb}, the phase uncertainty in measurements is given by

$$\Delta^2\phi_{Nb} = \frac{\cosh(4r)\cosh^2(r)\,\text{sech}^2(r)\sec^2\left(\frac{\phi}{2}\right) - 8}{4|\alpha|^2}. \qquad (3.7)$$

As the phase $\phi \to 0$, the limit of $\Delta^2\phi$ reaches a well-defined value given by

$$\Delta^2\phi_{Nb}|_{opt} = \frac{\cosh^2(2r)}{|\alpha|^2} \qquad (3.8)$$

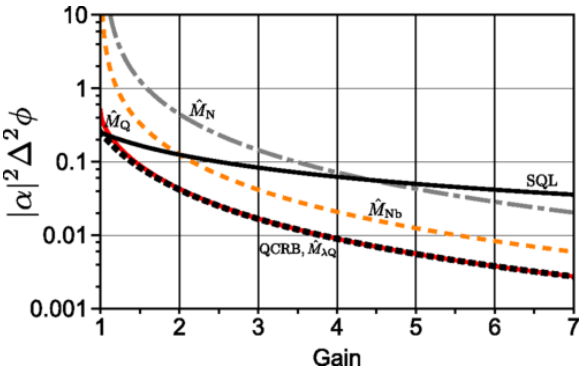

Figure 3.7: Optimal sensitivity as a function of gain for different detection schemes in a lossless SU(1,1) interferometer and a lossless truncated SU(1,1) interferometer. The sensitivity is normalized to the input seed. The gray dashed curve and the orange dashed curve represent the sensitivities of the operators $\mathrm{M_N}$ and $\mathrm{M_{Nb}}$ in a full SU(1,1) interferometer. The solid red plot shows the sensitivity of a truncated SU(1,1) interferometer and that of a full SU(1,1) interferometer with homodyne detection. The black dashed curve represents the QCRB for a two mode squeezed state as well as the sensitivity of the optimized operator $\mathrm{M_{Q\lambda}}$ in both a truncated and a full SU(1,1) interferometer. The λ value that saturates the QCRB in a full SU(1,1) interferometer are different from the values that saturate the QCRB in a truncated version. The black solid line corresponds to the SQL.

The value in the equation (3.8) is also the minimum of $\Delta^2\phi_{\mathrm{Nb}}$ among all the phase points, as shown in Figure 3.6. Figure 3.7 shows that the measurement $\mathrm{M_{Nb}}$ has better sensitivity than the total photon number measurement $\mathrm{M_N}$, and has the potential to beat the SQL at a comparatively lower 4WM gain. Though we must note that the conjugate photon number measurement, like the observable $\mathrm{M_N}$, also does not saturate the QCRB at any 4WM gain value and hence is not the most optimal measurement.

The above discussion is only for a lossless SU(1,1) interferometer. In the presence of loss, the above equations get modified. The important point to note here is that

the operating point $\phi \to 0$, does not remain optimal for phase sensing in a lossy interferometer. In fact, in the presence of loss, the phase uncertainty as $\phi \to 0$ becomes infinite, i.e., the point is not sensitive to phase. In presence of loss, the optimal phase sensing point moves a little away from the $\phi = 0$ point and depends on the amount of optical loss and the gain of the two NLO media in the interferometer. We will discuss the loss in an SU(1,1) interferometer in detail in a later section.

Before ending this discussion, we point out that the phase sensitivity of the probe photon number measurement, M_{Na}, does not saturate the QCRB and hence we do not discuss it here.

3.3.1.2 Homodyne detection

Another detection scheme uses homodyne detection to measure the joint quadrature of a_f and b_f modes, where the joint quadrature operator is given by $M_Q = e^{i\theta_a} a_f^\dagger + e^{-i\theta_a} a_f + e^{i\theta_b} b_f^\dagger + e^{-i\theta_b} b_f$. The phases θ_a and θ_b are the LO phases of the modes a_f and b_f. We can set the phase θ_b to measure the phase quadrature of the conjugate mode and replace the phase θ_a with the phase ϕ, defined earlier. Under these conditions, the phase uncertainty for an SU(1,1) interferometer with the joint quadrature measurement is given by

$$\Delta^2\phi = \frac{\sec^2(\phi)\,[1 - 2\tanh(r)\cos(\phi) + \tanh^2(r)]}{2|\alpha|^2}. \qquad (3.9)$$

This phase uncertainty is minimized when $\phi \to 0$, where the optimal phase sensitivity is given by

$$\Delta^2\phi_Q|_{min} = \frac{[\tanh(r) - 1]^2}{2|\alpha|^2}. \quad (3.10)$$

Figure 3.6 shows that the minimum uncertainty, given by equation (3.10), is obtained when $\phi \to 0$. Moreover, we can see that the phase sensitivity also approaches the QCRB as $\phi \to 0$. Figure 3.7 shows that the sensitivity of the joint quadrature measurement M_Q approaches QCRB for most 4WM gain values except the very small ones. Thus, we can say that M_Q is an optimal measurement for phase sensing in an SU(1,1) interferometer for most 4WM gain values.

As already mentioned, we can consider the 2nd NLO medium in an SU(1,1) interferometer as part of our detection scheme. Based on this, we tried to simplify the SU(1,1) interferometer setup. We removed the 2nd NLO and replaced everything after that with a joint homodyne detector on the two modes, as shown in Figure 3.4. We call this configuration the truncated SU(1,1) interferometer. We can call our measurement $M_Q = e^{i\theta_a}a_f^\dagger + e^{-i\theta_a}a_f + e^{i\theta_b}b_f^\dagger + e^{-i\theta_b}b_f$, here again, the parameters θ_a and θ_b represent the LO phases for the two modes a_f and b_f. We have used the same notation as that for the joint quadrature measurement with a conventional SU(1,1) interferometer because of their identical phase sensitivities. The phase uncertainty and the optimal sensitivity of a truncated SU(1,1) interferometer with the measurement M_Q are represented by the same equations that describe the sensitivities for a coventional SU(1,1) interferometer with the corresponding measurement, i.e., the equations (3.9) and (3.10).

We note that the sensitivity of an SU(1,1) interferometer and the truncated version are the same; they both saturate the QCRB for most 4WM gain values except very

small ones. Moreover, they both beat the SQL defined with the same number of photons passing through the phase object as in the two interferometers. Based on this observation, we built a truncated SU(1,1) interferometer and experimentally showed an improvement in phase sensing capacity over the SQL. Before moving to the experimental description, we will discuss the effect of losses on the sensitivity of a truncated SU(1,1) interferometer.

3.3.2 Sensitivity in a Lossy truncated SU(1,1) interferometer

In an experimental setup, there is always some form of optical loss. Therefore, the above equations for a lossless system will not be applicable for experimental work. We derived the equations for sensitivity including losses on the two modes [50]. For simplicity, we assumed equal losses on the two modes generated from the NLO medium. The uncertainty in the phase measurement with a lossy truncated SU(1,1) interferometer is given by:

$$\Delta^2\phi = \frac{2\eta + (1-2\eta)\,\mathrm{sech}^2(r) - 2\eta\,\sin(\phi_p)\tanh(r)}{2\eta|\alpha|^2\sin^2(\phi_p)}, \qquad (3.11)$$

where ϕ_p is the LO phase of the probe homodyne detector, and we set the conjugate LO to measure the phase quadrature of the conjugate beam. η is the transmission of the probe and the conjugate mode. η ranges between 0 (total loss) and 1 (no loss). Using equation (3.11), we can show that the optimal sensitivity is observed when we measure the phase quadrature of the probe beam.

3.3.3 Experimental work on a truncated SU(1,1) interferometer

We built a truncated version of an SU(1,1) interferometer with our 4WM system [53]. The schematic of our interferometer is shown in Figure 3.8. We seeded the 4WM process with a coherent beam of amplitude $|\alpha|$ and phase ϕ_o. The process amplifies the seed to give a probe beam and produces another beam known as the conjugate. As discussed in Chapter 1, the twin beams are quantum mechanically correlated and form a pair of two-mode squeezed states. We perform homodyne detection on both the beams. And measure the joint quadrature of the two beams. We put an electro-optic phase modulator (EOM) in the path of the LO beam in the homodyne detector on the seeded arm of the setup. The modulator serves as a phase object, which modulates the phase of the LO beam at a frequency of 1 MHz. We measure the signal and the associated noise using a spectrum analyzer.

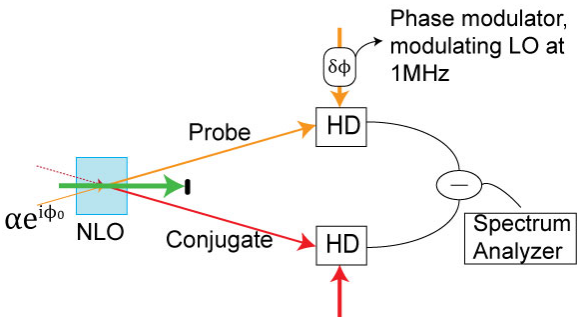

Figure 3.8: Experimental setup for a truncated SU(1,1) interferometer.

In each of the homodyne detectors, we overlap the signal (probe or conjugate) beam with its LO and subtract one output of the 50:50 beam splitter from the other. The process generates a signal dependent on the phase difference between the signal and the LO, as shown in Figure 3.9. We split the signal between a DC

component (<30 KHz) and an AC component (>30 KHz). We use the DC component to lock the homodyne detector to measure the phase quadrature of the signal beam. The AC part is used to measure the phase modulation put on by the EOM.

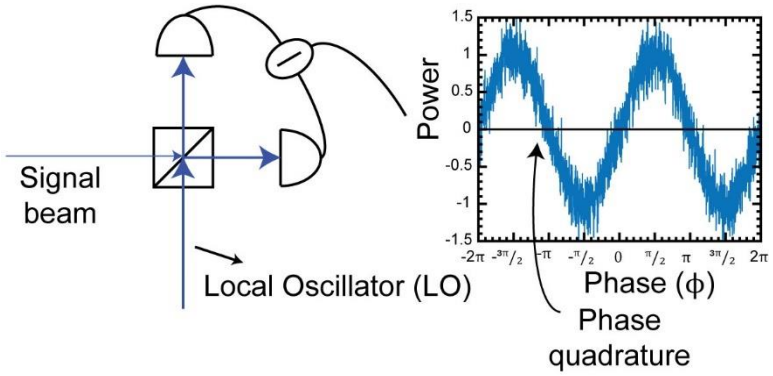

Figure 3.9: A schematic of a homodyne detector and the associated interference fringe, as we scan the phase difference between the two beams

We also compare the signal to noise ratio (SNR) of the measurement with the SQL. We measure the SQL by turning off the 4WM mixing process by blocking the pump beam, and we set the coherent seed equal in power to the probe beam. We show our experimental data in Figure 3.10. The solid blue plot shows the signal and noise for the phase measurement with the squeezed state of light, and the red plot represents corresponding measurements with the coherent beam. We obtained an improvement of ≈4dB in SNR over the SQL using the squeezed state.

We also measured the SNR with squeezed state at different operating points on the probe homodyne detector, i.e., by measuring different quadratures of the probe beam. Figure 3.11 shows the measured SNR data while we lock the probe homodyne detector to measure different quadratures of the probe beam. The solid

red line in the plot shows the theoretical fit for the data with the equation (3.11). The best fitting parameters were found to be 4WM gain G=3.3 and the loss parameter η=0.65. The experimental value for the gain was G=2.7.

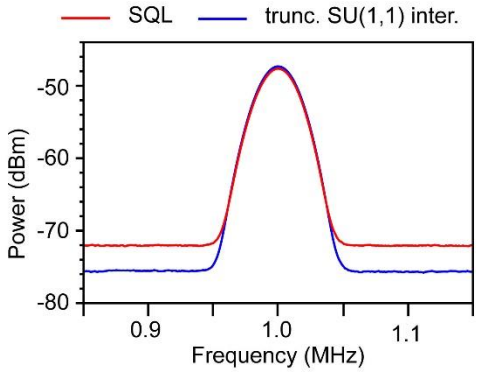

Figure 3.10: Measured SNR for the truncated SU(1,1) interferometer (solid blue) and the SQL (dotted red). We measured the SQL by blocking the pump beam to the 4WM mixing process and making the seed beam equal in power to the probe beam.

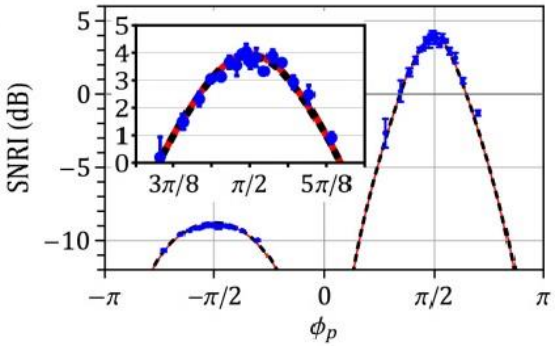

Figure 3.11: SNR data (blue dots with an error bar) measured with the squeezed state in our truncated SU(1,1) interferometer at different points on the probe homodyne detector fringe, i.e., while measuring different quadratures of the probe beam. The uncertainties are standard deviations from 10 independent measurements.

We also compared our SQL measurement with the theoretical value using the experimental parameters. For a sinusoidal phase modulation $\phi(t) = \sqrt{2}\delta\phi \sin(2\pi ft)$, the SNR for SQL measurement is given by:

$$\mathrm{SNR}_{coh} = \frac{2\eta_{coh}\rho P(\delta\phi)^2}{eB} \qquad (3.12)$$

where η_{coh} is the loss parameter for the coherent beam passing through the phase object, ρ is the responsivity of the detector, P is the power of the coherent beam going through the phase object, B is the measurement bandwidth, and e is the electronic charge. In our experiment, we had an optical power of $400(20)$ nW. The loss on the coherent beam was ≈20%, i.e., $\eta = 0.8$. The loss is different from the one expected on the squeezed beam, this happens because the loss on the squeezed beam incorporates the loss in state preparation. In our experiment, we used $\delta\phi = 1.7(0.2)$ mrad. Using the above mentioned parameters, we find a theoretical value of $\mathrm{SNR}_{coh} \approx 22.5$ dB. The value matches with our experimental observation given the uncertainties in our parameter values. If we remove all the losses from the SQL measurement, the SNR_{coh} will increase by ≈1 dB. This will still give an improvement of ≈3dB in SNR using our truncated SU(1,1) interferometer setup.

Summarizing some of the sources of loss and excess noise in our system: homodyne detection visibility: ≈98%, the electronic noise separation from the shot noise: ≈18 dB, and the detection efficiency of our balanced detectors: ≈98%. Although in Anderson et al. [53], we had mentioned 90% detection efficiency, we calibrated diodes later and found the detection efficiency to be 98%. The reduced

loss could be compensated by the equivalent excess noise from the homodyne detector visibilities which we discovered later.

3.4 OPTIMIZED MEASUREMENTS FOR SATURATING THE QCRB

As just mentioned a truncated SU(1,1) interferometer saturates the QCRB for a two-mode squeezed state, but saturation happens only for large values of the 4WM gain (Figure 3.7). Figure 3.12 shows an expanded version of relevant sensitivities from Figure 3.7. To saturate the QCRB at small gain values, we try another measurement given by $\mathrm{M_{Q\lambda}} = \mathrm{X_p} + \lambda \mathrm{X_c}$ [50, 54]. Here $\mathrm{X_p}$ and $\mathrm{X_c}$ represent the phase quadrature of the probe and the conjugate modes, and the parameter λ is an attenuation parameter with values between 0 and 1. The operator $\mathrm{M_{Q\lambda}}$ adds a scaled value of $\mathrm{X_c}$ to the probe quadrature $\mathrm{X_p}$. The solid blue line in Figure 3.12 shows the sensitivity of the measurement $\mathrm{M_{Q\lambda}}$. We see that the sensitivity using this measurement saturates the QCRB, shown with the dashed green line. The value of λ that allows $\mathrm{M_{Q\lambda}}$ to saturate the QCRB depends on the gain and the loss in the interferometer. For a lossless truncated SU(1,1) interferometer, the value of optimal λ is

$$\lambda_{\mathrm{opt}} = \tanh(2\mathrm{r}), \tag{3.13}$$

where r is the squeezing parameter, related to the 4WM gain $\mathrm{G} = \cosh^2(\mathrm{r})$.

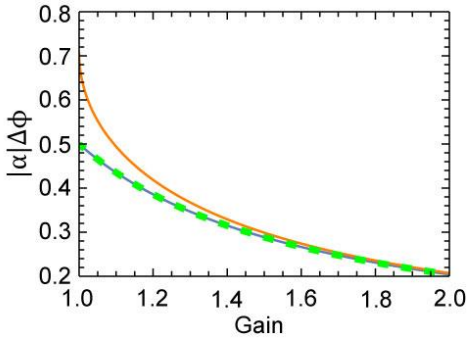

Figure 3.12: Theoretical peak sensitivity, multiplied by the amplitude ($|\alpha|$) of the coherent seed beam of the interferometer, achieved by an ideal lossless truncated SU(1,1) interferometer as a function of gain in the 4WM process. The solid orange curve shows the phase sensitivity of the observable M_Q and the solid blue curve represents the phase sensitivity of the observable $M_{Q\lambda_{opt}}$(as defined in the text). The thick dashed green curve indicates the QCRB for the two-mode squeezed state.

We note that we put our phase object in the probe beam and the operator $M_{Q\lambda}$ puts an attenuation on the conjugate quadrature. Thus, adjusting the λ does not change the signal from the phase object, and only changes the noise in the measurement. Hence, to observe the change in SNR as we modify the attenuation, it is sufficient to monitor the noise floor of the measurement. We show in Figure 3.13 (a), the noise of the measurement $M_{Q\lambda}$ as we change the attenuation λ for a lossless truncated SU(1,1) interferometer. We plot the noise values for different 4WM gain. We see that the noise minimizes at a value of λ which we call λ_{opt}, and the value of λ_{opt} changes as we change the gain. Figure 3.13 (b) shows the variation of λ_{opt} as a function of the 4WM gain, at different transmissions of the probe and the conjugate. We assume the same losses on each of the twin beams for simplicity. We can also note that the value of λ_{opt} saturates to 1 as we increase the 4WM

gain, but the optical losses delay the saturation to larger gain values. Similar to equation (3.13), we can analytically define the optimal value of λ in a lossy interferometer.

$$\lambda_{opt} = \frac{\sqrt{\eta_p \eta_c}\sinh(2r)}{1 - \eta_c + \eta_c \cosh(2r)}, \tag{3.14}$$

where η_p and η_c are the transmissions of the probe and the conjugate beams.

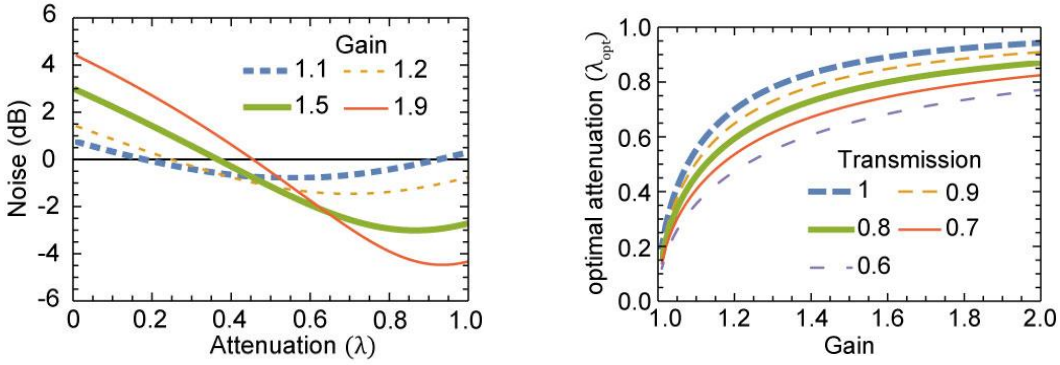

a b

Figure 3.13: (a) Noise of the measurement $M_{Q\lambda}$ as a function of attenuation parameter λ at various 4WM gains. (b) Variation of λ_{opt} as a fucntion of 4WM gain at different losses in the interferometer.

The enhancement in absolute phase sensitivity also means a relative improvement over the SQL. As mentioned earlier, we define the SQL as the phase sensitivity of a Mach-Zehnder interferometer (MZI) with the same number of photons going through the phase sensing arm of the MZI as the number that go through the phase object in our truncated SU(1,1) interferometer. We can measure the SQL in our setup by replacing the probe and the conjugate beams with the coherent beams having the same number of photons. Just to note, what actually matters here is that we send the same number of coherent beam photons only in the probe arm,

which has the phase object. The conjugate arm photon number doesn't matter, as the signal from the conjugate homodyne detector is independent of photon numbers in the arm. This setup has the same sensitivity as a standard Mach-Zehnder interferometer.

Above, we mentioned that while measuring the SQL, it didn't matter what number of coherent beam photons went through the conjugate arm, as the quadrature noise of a coherent beam is independent of the mean photon number in the beam. We can say that the conjugate arm homodyne detector, while measuring the SQL, only adds noise and hence worsens the SNR. If we remove the conjugate arm homodyne detector, while measuring the SQL, we will get a better coherent beam SNR. We can call this another definition of SQL, but a very stringent one. We can refer to this definition of SQL as SQL2. We call the former definition of the SQL, where we consider both the homodyne detectors in our measurement of the SQL, as SQL1.

We can relate the SNR improvement over the SQL to the sensitivities of the measurements using the formula

$$\mathrm{SNRI} = -10\mathrm{Log}_{10}\left(\frac{\Delta^2\phi_{\mathrm{tSU}}}{\Delta^2\phi_{\mathrm{SQL}}}\right), \qquad (3.15)$$

where $\Delta^2\phi_{\mathrm{tSU}}$ and $\Delta^2\phi_{\mathrm{SQL}}$ are the phase uncertainties of the measurement with the truncated SU(1,1) interferometer and with the coherent beam. We show in Figure 3.14 the improvement in SNR over the SQL1 (right side y-axis) and the SQL2 (left y-axis). We change the attenuation of the conjugate homodyne detector,

λ, and theoretically compute the SNR improvement over the two definitions of the SQL at different 4WM gains. We can see the optimized λ value that maximizes the SNR improvement. Additionally, we can also point out that at the gain of ~1.1 the SNR doesn't beat the SQL2 with the measurement of $\mathrm{M_Q}$, i.e., $\lambda = 1$, but at the optimized value of λ, the sensitivity of $\mathrm{M_{Q\lambda}}$ operator goes beyond the SQL2.

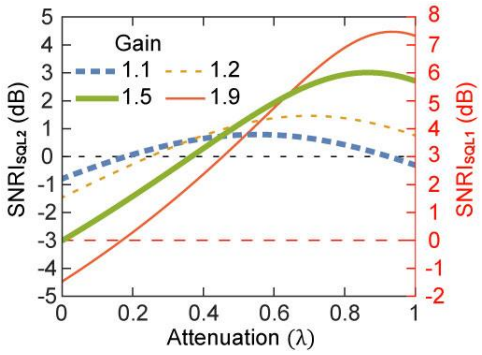

Figure 3.14: SNR improvement over the SQL1 (right y-axis, red color), and the SQL2 (left side y-axis), as defined above, for a lossless truncated SU(1,1) interferometer.

3.4.1 Experimental demonstration

We made an experiment similar to the one shown in Figure 3.8, but with a modification, as shown in Figure 3.15 [54]. We put an electrical attenuation on the conjugate homodyne detector output before adding its signal to the probe homodyne detector. The process gives a measurement of the operator $\mathrm{M_{Q\lambda}} = \mathrm{X_p} + \lambda \mathrm{X_c}$. As in the setup of Figure 3.8, we put an electro-optic phase modulator in the LO in the probe homodyne detector, which puts a sinusoidal modulation on the LO. As mentioned earlier, in this experiment, we put the attenuator on the conjugate homodyne detector output and the phase modulator in the probe homodyne detector. Thus, we do not affect the signal produced as a result of phase

modulation and only affect the noise floor of the measurement when we change the attenuation λ. Hence, in this experiment, we observe the noise floor of the measurement and do not worry about the signal due to the phase modulator.

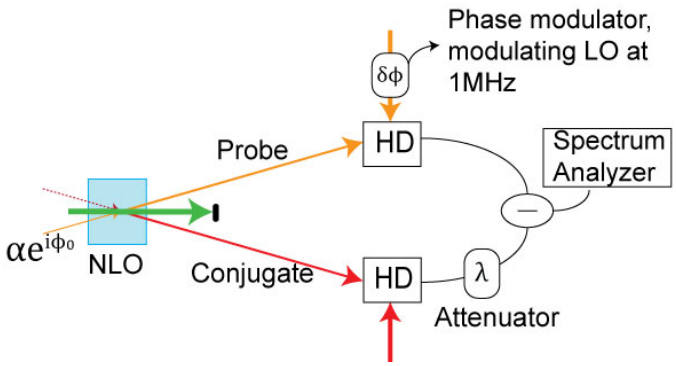

Figure 3.15: Experimental setup for the phase measurement with the operator $M_{Q\lambda}$. We apply an electrical attenuation on the output of the conjugate homodyne detector before combining it with the output of the probe homodyne detector to get $M_{Q\lambda} = X_p + \lambda X_c$.

We present our experimental data on the measurement of noise in the operator $M_{Q\lambda}$ in Figure 3.16. Figure 3.16 (a) shows the absolute noise of the joint homodyne detector which gives an output of $|\alpha_{LO}|M_{Q\lambda}$, i.e., the joint quadrature operator scaled by the amplitude of the LO beams. We fit a theoretical curve through the data points. We use the 4WM gain, the optical losses on the two beams and a scaling factor as free parameters. We put 3% extra loss on the probe beam due to its proximity to the ^{85}Rb transition in the Doppler-broadened medium. We verified this extra loss experimentally. The scaling parameter considers the LO power, which acts like an electronic gain in the homodyne detector. The red curves in the two plots show the theoretical fits. The values of the free parameters we obtain

match our experimental values very well within uncertainties. The parameter values are provided in the caption of Figure 3.16.

The plots in Figure 3.16 (b) show the SNR improvement over the two definitions of the SQL for the measurements made in Figure 3.16 (a). The right-side axis (red color) shows the improvement over the SQL1, the left side (black) represents the improvement over the more stringent definition of the SQL, i.e., SQL2. We calculate the theoretical curves in these plots using the gain and the losses obtained from Figure 3.16 (a). We see that in both the plots the theoretical curves pass through the higher end of the experimental data. This happens because we take the experimental data by locking our homodyne detectors to measure the phase quadrature of each beam. The locking errors present in our system degrades our measurement and decreases our improvement over the SQL. The theoretical curves consider only the 4WM gain and the optical loss in the interferometer and not the locking errors. Hence, the theory curves represent the maximum possible improvement for our setup.

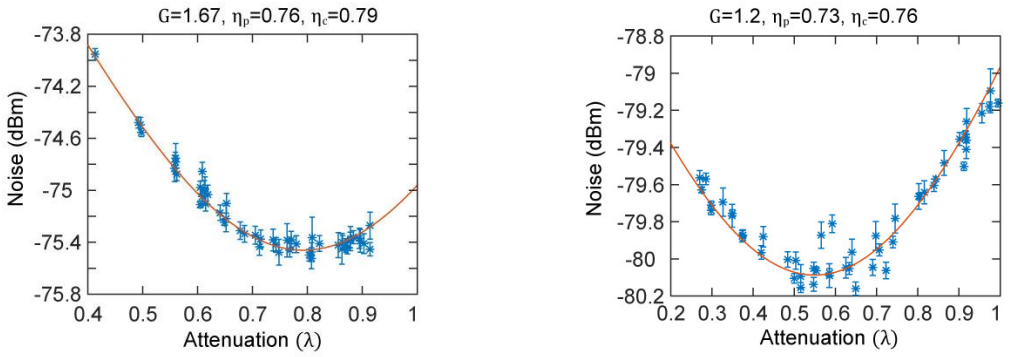

a

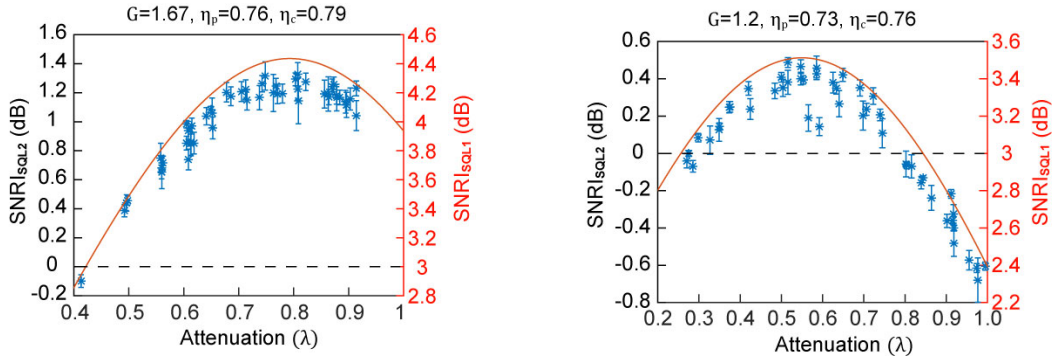

b

Figure 3.16: Measurements of $M_{Q\lambda}$. (a) Noise in the measurement of $M_{Q\lambda}$ in our truncated SU(1,1) interferometer versus the attenuation parameter λ. (b) Improvement in the SNR as a function of the attenuation λ with the measurements $M_{Q\lambda}$ over the SQL1 ($SNRI_{SQL1}$) and the SQL2 ($SNRI_{SQL2}$). The left and right side plots have estimated 4WM gains, probe and conjugate transmissions as indicated. The gain and the loss values were estimated from the theoretical fit of the data. The fits used 3% less transmittance for the probe beam than the conjugate beam, which we measure experimentally.

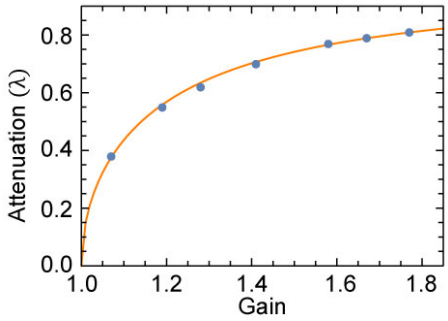

Figure 3.17: λ_{opt} as a function of the 4WM gain. The points are experimental measurements determined from plots like those in Figure 3.16. A theoretical curve is generated using a probe beam transmission of 74.5% and a conjugate beam transmission of 77.5%. These values represent the typical losses in our system.

We estimated λ_{opt} from the plots in Figure 3.16. We took similar data at other 4WM gain values and estimated λ_{opt} from those plots. We plot all those λ_{opt} values in Figure 3.17 against the respective 4WM gain values. We also plot a theoretical curve using the typical losses present in our experiment. The theoretical curve fits very well with the experimental data, as shown in Figure 3.17.

3.4.2 $M_{Q\lambda}$ measurements in a full SU(1,1) interferometer

In the past sections, we have discussed only the truncated SU(1,1) interferometer, where we performed optimized measurements of $M_{Q\lambda}$ to saturate the QCRB for two-mode squeezed light. We mentioned earlier in the text that the sensitivity of the operators M_Q is the same for both the full and the truncated versions of the SU(1,1) interferometer. The results for the M_Q operators in Figure 3.7 and Figure 3.12 represent both the truncated and the full SU(1,1) interferometers. Similarly, the operator $M_{Q\lambda}$ also represents both the interferometers, where the sensitivities of the interferometers saturate the QCRB of the two-mode state at all

4WM gains. The only difference here is the value of λ that optimizes the measurement. The λ value that saturates the QCRB for the truncated SU(1,1) interferometer could be different from the one that is optimal for the full SU(1,1) interferometer.

In the last sections, our discussion has included the interferometers where we seed the NLO medium in our interferometer with a coherent seed. In another configuration, we can do interferometry with only vacuum seeds in the NLO medium of the interferometers. We describe the vacuum seeded interferometry in the following section.

3.5 VACUUM SEEDED CONFIGURATION

We refer to Figure 3.5 again. We remove the coherent seed in the a_o mode and replace it with a vacuum seed, as shown in Figure 3.18. The first NLO medium produces a two-mode vacuum squeezed state and we send the a_i mode through a phase object. We mix the a_i mode after the phase object and the b_i mode directly from the 1st NLO medium in another similar NLO medium, with a pump beam. The output of the 2nd NLO medium is given by a_f and b_f.

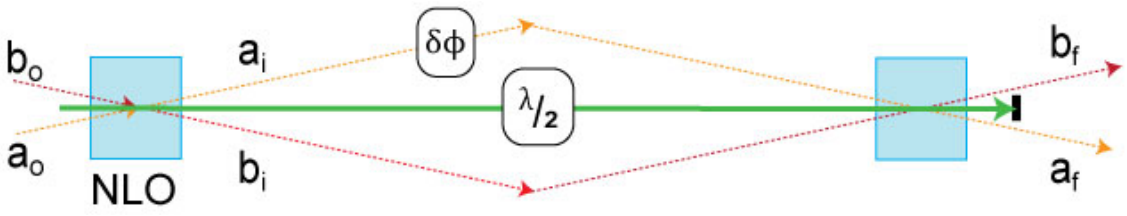

Figure 3.18: Schematic of a vacuum seeded SU(1,1) interferometer with the operator representation of various states of light.

As in the coherent seeded interferometry, here again, we can have different types of detection. We first consider the direct detection of the two modes a_f and b_f. We consider the total photon number, $M_N = a_f^\dagger a_f + b_f^\dagger b_f$. We can again use the Heisenberg approach, discussed in the Appendix B, to get the analytical expressions for the sensitivity of the observable M_N, which is given in equation (3.16) as a function of operating point ϕ for a lossless SU(1,1) interferometer.

$$\Delta^2\phi = \coth^2(2r)\sec^2\left(\frac{\phi}{2}\right) - 1, \qquad (3.16)$$

where all the parameters represent the same physical quantities they represented earlier. We can use the equation (3.16) to get the best operating point, where the phase uncertainty $\Delta^2\phi$ is the smallest. We can see that as the phase $\phi \to 0$, $\Delta^2\phi$ reaches a minimum given by

$$\Delta^2\phi_{min} = \cosh^2(2r). \qquad (3.17)$$

We plot the optimal phase sensitivity with M_N, i.e., equation (3.17) in Figure 3.19. We find that the phase sensitivity of M_N saturates the QCRB for a two-mode vacuum squeezed state. Therefore, we can say that the total photon number M_N is an optimal measurement for a vacuum seeded SU(1,1) interferometer. We must remember, unlike here, the total photon number M_N (or the photon number measurement in mode b_f, i.e., M_{Nb}) was not an optimal measurement for the coherent seeded SU(1,1) interferometer and did not saturate the QCRB for a bright two-mode squeezed state.

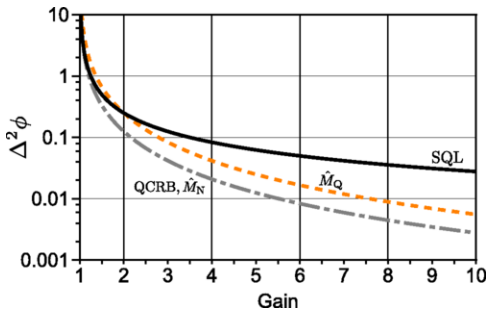

Figure 3.19: Sensitivity of a vacuum seeded interferometer for different detection schemes. The solid black line represents the SQL, the dashed orange curve is the sensitivity of the joint quadrature measurement, and the gray dashed-dotted curve shows the phase uncertainty of the total photon number M_N, which also coincides with the QCRB for two-mode vacuum squeezed light.

As we mentioned in the seeded configuration, in the presence of loss, the $\phi = 0$ point does not show any phase sensitivity. The phase sensitivity maximizes at a point away from $\phi = 0$, and depends on the gain of the NLO media and the optical losses.

Homodyne detection

Another detection scheme is joint homodyne detection. Similar to the seeded case, we represent it by $M_Q = e^{i\theta_a} a_f^\dagger + e^{-i\theta_a} a_f + e^{i\theta_b} b_f^\dagger + e^{-i\theta_b} b_f$. The phases θ_a and θ_b are the LO phases of the modes a_f and b_f. Without losing generality, we can set the phase θ_a to measure the phase quadrature of the a_f mode, since ϕ can take care of the LO phase in the a_f mode. The sensitivity of the quadrature measurement is given by

$$\Delta^2\phi = \frac{\left(\partial_\phi \Delta M_Q\right)^2}{\Delta^2 M_Q^2} \qquad (3.18)$$

here, ΔM_Q is the standard deviation in the measurement of the joint quadrature operator M_Q, and the quantity $\Delta^2 M_Q^2$ is the noise on the noise of the measurement M_Q [50]. For a Gaussian signal, the fourth moment and the second moment are related, and hence the above quantity can be re-written as

$$\Delta^2\phi = \frac{\left(\partial_\phi \Delta M_Q\right)^2}{2\left(\Delta^2 M_Q\right)}. \tag{3.19}$$

We can use the above equations to analytically calculate the phase uncertainty in the measurement of M_Q as a function of ϕ given by

$$\Delta^2\phi = \frac{1}{2}\csc^2(\phi - \theta_b)[2\cos(\phi - \theta_b) + \tanh(r) + \coth(r)]^2 . \tag{3.20}$$

We find that as

$$\phi - \theta_b \to \pi - \tan^{-1}(\operatorname{csch}(2r)), \tag{3.21}$$

$\Delta^2\phi$ optimizes to the minimum uncertainty value given by

$$\Delta^2\phi = 2\operatorname{csch}^2(2r). \tag{3.22}$$

We plot equation (3.22) in Figure 3.19 as a function of NLO medium gain, where we find that the sensitivity of M_Q beats the SQL but it doesn't saturate the QCRB. This is in contrast to the coherent seeded interferometry where the joint quadrature measurement M_Q for most gains (and modified measurement $M_{Q\lambda}$ for all gains) saturates the QCRB. We do not plot any theoretical results for $M_{Q\lambda}$ for vacuum seeded interferometry, as we found that anything other than $\lambda = 1$ just degrades the sensitivity.

3.5.1 Vacuum seeded truncated SU(1,1) interferometer

For the vacuum seeded case, like the seeded interferometer, we can remove the 2nd NLO medium and replace it with two homodyne detctors, one on each mode. We can measure the joint quadrature of the two output modes, given by $M_Q = e^{i\theta_a}a_f^\dagger + e^{-i\theta_a}a_f + e^{i\theta_b}b_f^\dagger + e^{-i\theta_b}b_f$. The phases θ_a and θ_b are the LO phases of the modes a_f and b_f. Again, like the seeded interferometry, M_Q operator for the vacuum seeded truncated SU(1,1) interferometer has the same sensitivity as that of the conventional SU(1,1) interferometer. Equations (3.20), (3.21), and (3.22) are also applicable for the measurement of M_Q in a truncated SU(1,1) interferometer.

Although we can see from Figure 3.19 that the joint quadrature measurement is not optimal for phase measurement in a truncated or a conventional SU(1,1) interferometer, the photon number measurement is not practical for our experimental setup.

3.5.2 Experimental demonstration

We built a truncated SU(1,1) interferometer similar to the one shown in Figure 3.8, but with vacuum seeds in both the input ports, as shown in Figure 3.20. In this experiment, we collect data showing the phase dependence of the quadrature noise. We can collect the quadrature data from an oscilloscope or get the quadrature noise data from a spectrum analyzer. We use equations (3.18) and (3.19) to caluculate the phase sensitivity of the measurement using the experimental data. Since equation (3.18) is a more intutive definition, and the equation (3.19) is a derived equation based on Gaussian measurement properties,

we verify the sensitivity of our experiment with both the equations. Equation (3.19) gives us the freedon to measure only one quantity to get the phase sensitivty of the measurement instead of the two quantities in equation (3.18).

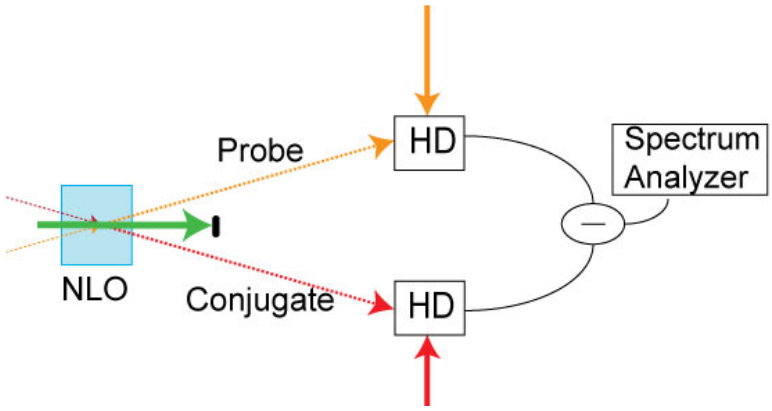

Figure 3.20: Experimental setup for the vacuum seeded truncated SU(1,1) interferometer.

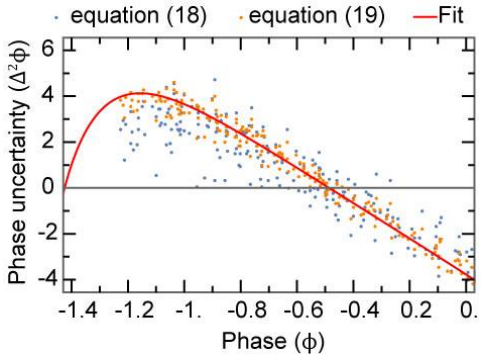

Figure 3.21: Experimental data verifying the agreement of equation (3.18) (blue dots) and equation (3.19) (orange dots). Red curve is the theoretical fit for the given measurement.

We collect the quadrature data with an oscilloscope for different phase shifts in the joint homodyne detector. We calculate the noise of the data at various homodyne phases. We fit the data to a sinusoidal function of the quadrature phase to get the slope of the data with respect to the quadrature phase. We calculate the quantity $\Delta^2 M_Q^2$ to get the noise on the quadrature noise, and finally we use the estimated

slope and $\Delta^2 M_Q^2$ to get the phase sensitivity at various quadrature phase operating points. We show one such estimation in Figure 3.21, where the red dots in the plot show the estimation of phase sensitivity using equation (3.18). We also show the phase sensitivity calculated using equation (3.19) (blue dots) in Figure 3.21. For the calculation with equation (3.19), we fit the quadrature noise to a sinusoidal function of the quadrature phase. We estimate the slope of the quadrature noise with respect to the phase using the theoretical plot, and finally use the slope and the quadrature noise to calculate the phase sensitivity. We find from Figure 3.21, that sensitivity estimation using both the equations agree with each other.

We present the estimation of phase sensitivity of vacuum seeded SU(1,1) interferometer using our experimental data in Figure 3.22. Figure 3.22 shows only a fraction of the data we have taken at different 4WM gain settings. We can see that we are almost 1-2 dB away from the SQL. Depending on the gain and the squeezing in the apparatus, we come as close as within 0.5 dB of the SQL.

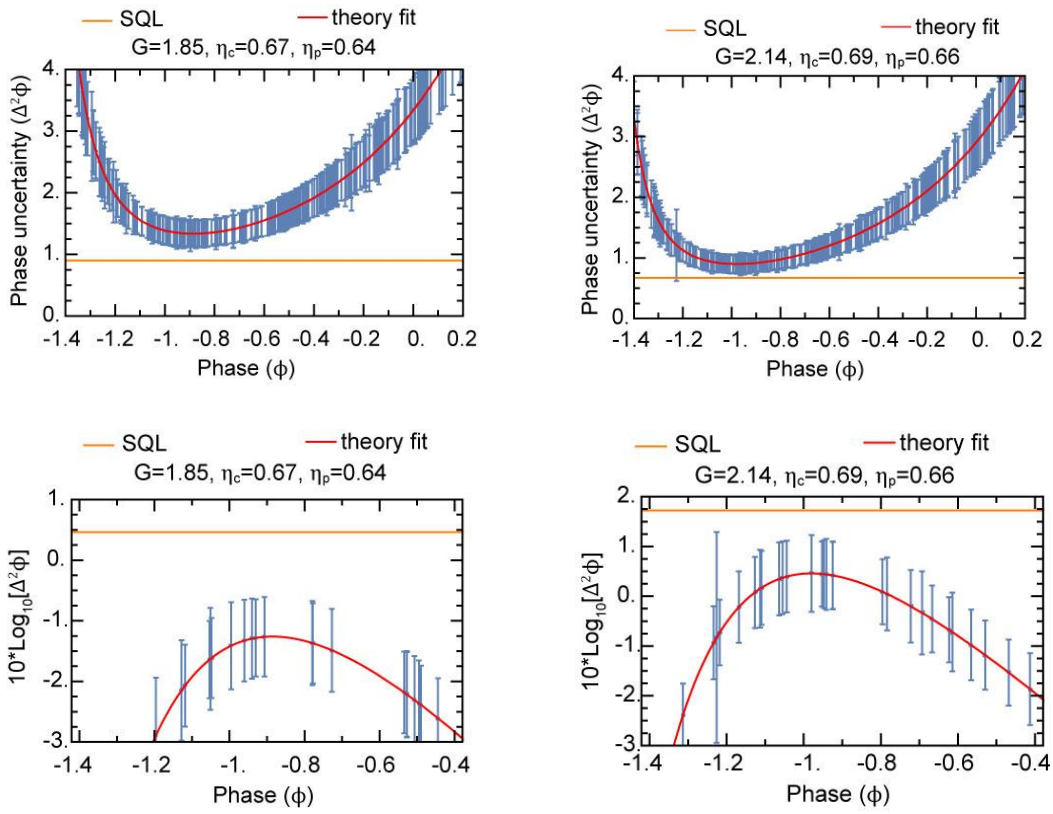

Figure 3.22: Experimental data for the sensitivity of the operator M_Q in a truncated SU(1,1) interferometer. The upper plots show the phase uncertainty ($\Delta^2\phi$) as a fucntion of the phase ϕ. The lower plots show a few points near the best sensitivity point, on the log scale which can be directly translated to the SNR. We see from the lower plots, the phase sensitivity of our data is still worse than the SQL by ~1-2 dB. This depends on the gain of the 4WM. For a variety of gain values, we are away from the SQL by at least 0.5 dB.

The reasons that we do not beat the SQL are numerous. The most important reason is the degree of quantum mechanical squeezing, we will understand more of this later. Other reasons include, experimental instability, which we tried to remove by bringing in the specially designed Rb vapor cells, and by using 3-axis piezo mirrors for better phase locking the homodyne detectors. We dedicated significant discussion to them in Chapter 1. Next, we will examine the experimental requirements specific to our apparatus to get phase sensitivities beyond the SQL.

Since we could not beat the SQL with our vacuum seeded truncated SU(1,1) interferometer, we give some necessary conditions to go beyond the SQL. In Figure 3.23, we show a theoretical simulation of SNR improvement over the SQL using the vacuum seeded truncated SU(1,1) interferometer. The plot demonstrates improvement over the SQL at a given 4WM gain and squeezing. In other words, we can say that the simulation shows the amount of squeezing required at a given gain to beat the SQL. Since squeezing is highly dependent on loss or any excess noise in the system, the plots also put an upper bar on loss or excess noise that is tolerable for beating the SQL. We can see that at a reasonable gain of ~3, we require over 5 dB squeezing to go beyond the SQL, which is a little beyond the capacity of our current system.

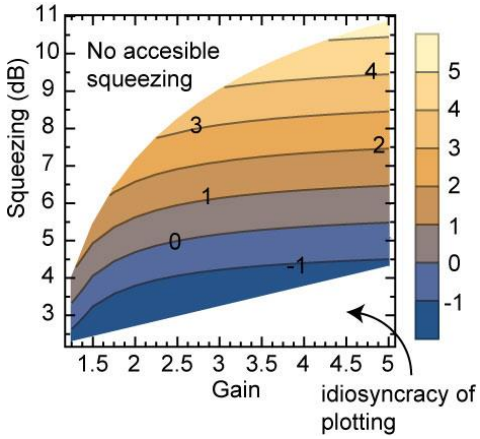

Figure 3.23: Theoretical plot showing the potential SNR improvement over the SQL with the 4WM gain and the squeezing available in our system. The positive contour line means higher SNR than the SQL. For a given gain, the squeezing is changed by varying the amount of optical loss on the probe and the conjugate beams. In the simulation, we have always kept the probe beam loss 5% greater than the conjugate beam loss.

We have seen many suggestions on improving the squeezing in our 4WM system in Chapter 1. Some of which we have tried after we obtained the above results.

So far, we have talked about multiple detection schemes in the coherent beam seeded and vacuum seeded configurations of the SU(1,1) interferometer. Some of the detection schemes were optimal in saturating the QCRB and some were not. In Table 2 we provide a summary of the performance of different detection schemes in a conventional and a truncated SU(1,1) interferometer. Much of this discussion is also available in our publication [50].

Table 2: Summary of phase sensitivities for different detection schemes compared to the QCRB.

SU(1,1) interferometer		
Detection scheme	**Coherent seeded**	**Vacuum seeded**
M_N	Suboptimal	Saturates QCRB
M_{Nb}	Suboptimal	Saturates QCRB
M_Q	Saturates QCRB for large G	Suboptimal
$M_{Q\lambda}$	Saturates QCRB	Suboptimal
Truncated SU(1,1) interferometer		
M_Q	Saturates QCRB for large G	Suboptimal
$M_{Q\lambda}$	Saturates QCRB	Suboptimal

Before closing the discussions on phase measurement with a full or a truncated SU(1,1) interferometer, we would like to give a small description of the usefulness

of a conventional SU(1,1) interferometer over a truncated SU(1,1) interferometer. A conventional SU(1,1) interferometer is detection loss tolerant [9, 55, 56, 50].

We define the internal loss in an SU(1,1) interferometer as the loss on the probe and the conjugate in between the NLO media. The external loss means any loss on the beams after the 2nd NLO medium. We can compensate for any external loss in an SU(1,1) interferometer by increasing the gain of the 2nd NLO medium. We show in Figure 3.24, the variation of the normalized phase sensitivity of an SU(1,1) interferometer as a function of the 2nd NLO medium gain. We use the total photon number operator M_N for the phase sensitivity calculations. We see that increasing the gain of the 2nd NLO medium decreases the phase uncertainty. We can also find that if the external loss is high, it takes a larger 2nd NLO medium gain to compensate for the loss.

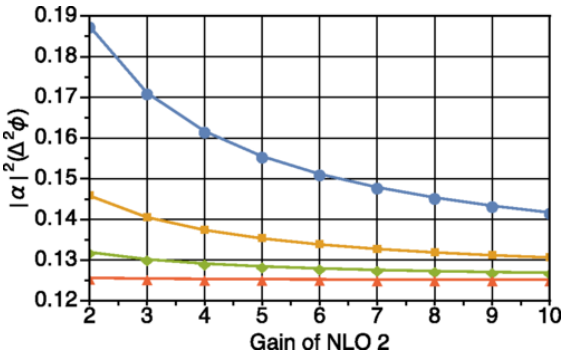

Figure 3.24: Sensitivity versus gain of NLO 2 for intensity detection, M_N, of the conventional SU(1,1) interferometer, optimized over ϕ. NLO 1 has a gain of 2 and there is no internal loss. The blue circles, yellow squares, green diamonds, and orange triangles represent external transmissions of 0.5, 0.75, 0.9, and 0.99, respectively.

Manceau et al. [9] have recently performed an experiment demonstrating the robustness to detection loss in a vacuum seeded SU(1,1) interferometer built using

a χ^2 nonlinear medium for the generation and mixing of quantum states. They used the total photon number operator $\mathrm{M_N}$ as their detection scheme. In our system, we can perform a similar experiment using a joint homodyne detector.

We must note one point before proceeding further, the 2nd NLO medium gain does not compensate for any internal loss in the interferometer. Increasing the gain of the 2nd NLO medium will not improve the sensitivity degraded by internal loss.

4 Quantum phase tracking

In the previous chapter, we discussed phase measurement with squeezed state of light. We talked about measuring a small phase fluctuation around a fixed or known phase. The process is known as phase sensing. In such a situation, the system can be linearized about a fixed phase, and we can think only about improving the signal to noise ratio of the measurement [57, 31].

In another kind of measurement, we measure a completely unknown phase. Unlike the previous experiment, we do not have a known locked phase around which we measure the small phase modulation. Contrary to phase sensing, where a system can be linearized around a fixed phase [57, 31], here the measurement requires non-trivial adaptive algorithms to perform the unknown phase estimation [58, 59, 60, 61, 62, 63, 64, 65]. There is some experimental work to beat the SQL in an unknown phase measurement in a homodyne detector [14, 15, 66, 16] and with photon number detection, though with post-selection of data [67]. Recently, there has been some work, where the phase measurement has been performed within 4% of the Heisenberg limit using adaptive techniques [68].

Adaptive algorithms can be used for various kinds of phase measurement. Figure 4.1 shows a schematic of an experiment for the measurement of an unknown phase. Here, an unknown phase (large or small) is applied in one arm of the interferometer. The unknown phase could be large or small, DC [67, 16] or AC [15, 64, 65] in nature. The process here is to put a controllable phase device in the other arm of the interferometer. The output of the interferometer depends on the difference between the unknown phase and the controllable phase. The output is

used to apply feedback on the controllable phase to track the unknown phase. The feedback is provided such that the output stays at the most phase sensitive point on the interferometer fringe.

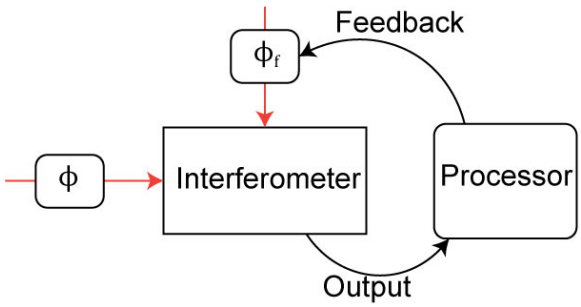

Figure 4.1: Schematic for a measurement of an unknown phase in an interferometer. An unknown phase is placed in one of the arms of the interferometer. A controllable phase is put in the other arm. The output of the interferometer depends on the phase difference between the unknown phase and the controllable phase. The output passes through a processor which sends feedback to the controllable phase to track the unknown phase.

In this work, our goal is to track an unknown AC phase, which has the form of a stochastic waveform, with an accuracy better than the SQL. We do phase tracking using our truncated SU(1,1) interferometer with a two-mode squeezed state, as discussed in Chapter 3. We build homodyne detectors for each mode, i.e., the probe and the conjugate. We put a phase noise on the probe beam and try to track the noise using the probe LO beam. We put a stochastic waveform in our experiment [15, 65, 66, 69], given by

$$\phi = \sqrt{\kappa} \int_{-\infty}^{t} e^{-\lambda(t-s)}\, dV(s), \qquad (4.1)$$

where $dV(s)$ is a classical Weiner process, λ is the bandwidth of the stochastic waveform, and κ defines the amplitude of the waveform, and is of the order of unity. We can take a time derivative of the above equation to get

$$\dot{\phi}(t) = -\lambda\phi(t) + \sqrt{\kappa}dV(t), \tag{4.2}$$

where $\dot{\phi}(t)$ is the time derivative of $\phi(t)$. Equation (4.2) is a more useful form for the present work.

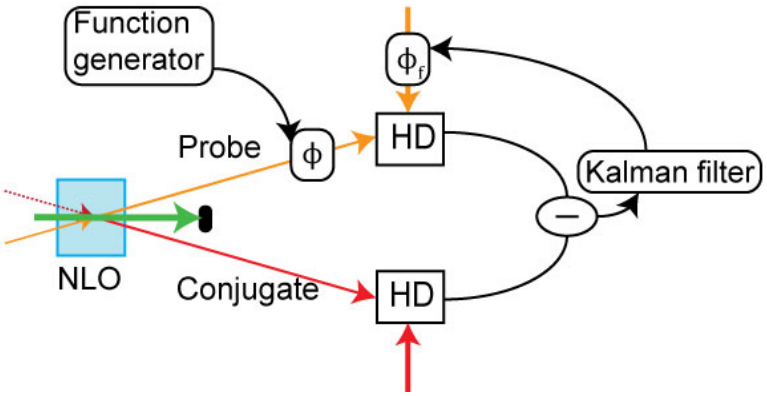

Figure 4.2: Schematic of phase tracking setup.

In our experiment, as shown in Figure 4.2, we place a phase modulator in the probe beam path and one in the path of the probe LO. We put a stochastic phase waveform on the probe beam phase modulator and track the waveform using the controllable phase modulator in the LO beam path. We take the joint homodyne detector signal and pass it through a Kalman filter, which generates a feedback signal for the phase modulator in the LO beam path. We describe the Kalman filter in Appendix C. We have mentioned in the previous chapter that our truncated interferometer behaves in the most sensitive way when we measure the joint phase sum quadratures of the probe and the conjugate beams, i.e., the phase

quadrature of each of the beams (and sum them). Hence, in our interferometer, we lock the phase of the conjugate beam homodyne detector to measure its phase quadrature. In the probe beam homodyne detector, we apply a feedback from the Kalman filter to the phase modulator on the LO beam. The feedback tries to change the phase of the LO beam such that we come close to measuring the phase quadrature of the probe beam.

If we can track the phase of the probe beam properly with the LO using the feedback algorithm, then the output current of the joint homodyne detector can be written as [64, 15]

$$I(t)dt = 2|\alpha|\big(\phi(t) - \phi_f(t)\big)dt + \sqrt{R_{sq}}dW(t), \tag{4.3}$$

$$R_{sq} = \sigma_f^2 e^{2r_{asq}} + \big(1 - \sigma_f^2\big)e^{-2r_{sq}}. \tag{4.4}$$

Here, σ_f^2 is the phase variance (or error) of tracking process, given by $\sigma_f^2 = \langle\phi(t) - \phi_f(t)\rangle^2$, $\phi_f(t)$ is the feedback on the phase modulator in the LO path. R_{sq} represents the noise of the joint homodyne detector as a result of the error in phase tracking, where $e^{2r_{asq}}$ and $e^{-2r_{sq}}$ are the noises of the anti-squeezed and the squeezed quadratures respectively. $\frac{dW(t)}{dt}$ corresponds to a Gaussian white noise. We have used different parameters r_{asq} and r_{sq} for the anti-squeezed and the squeezed noise, respectively, to consider optical loss or excess noise in the system causing a difference in the values of the two parameters.

We can use equations (4.2) and (4.3) with a Kalman filter to obtain an optimized feedback response $\phi_f(t)$ [64, 15]. A Kalman filter is considered the minimum mean

squared error estimator given the state equations of the form in equations (4.2) and (4.3) [64, 15, 70]. We describe the Kalman filter in Appendix C.

In a feedback loop, the analytical expression for steady state error is given by [64, 15],

$$\sigma_f^2 = \frac{\lambda R_{sq}}{4|\alpha|^2}\left(\sqrt{1+\frac{4\kappa|\alpha|^2}{\lambda^2 \overline{R}_{sq}}}-1\right). \tag{4.5}$$

The steady-state feedback signal is given by

$$\phi_f(t) = \Gamma \int_{-\infty}^{t} I(s) e^{-\lambda(t-s)} ds, \tag{4.6}$$

where Γ, known as the Kalman gain, is shown in equation (4.7),

$$\Gamma = -\lambda + \sqrt{\lambda^2 + \frac{4\kappa|\alpha|^2}{\overline{R}_{sq}}}. \tag{4.7}$$

We present in Figure 4.3 some theoretical simulations of the system using the phase tracking algorithm. We provide the algorithm in Appendix C. Figure 4.3 (a) shows a simulation of the feedback phase (blue) applied to the LO in response to the original stochastic phase (orange) applied on the probe beam. The plots show the working of the tracking algorithm on the simulated data of the homodyne detector and the stochastic waveform.

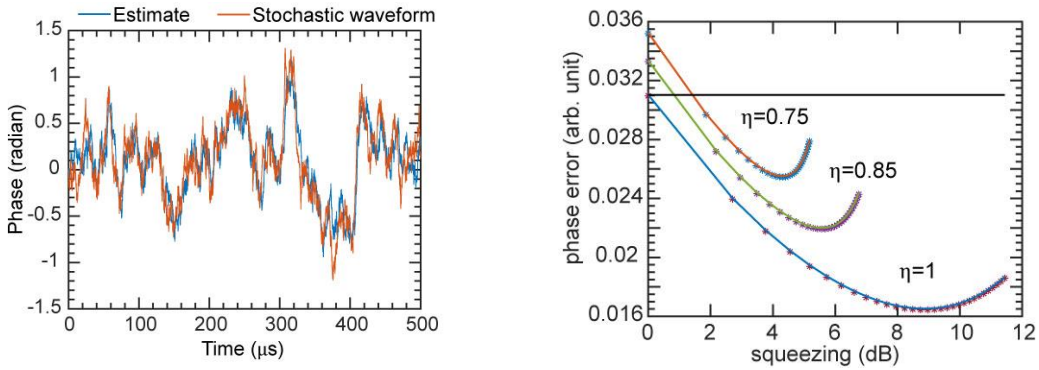

a b

Figure 4.3: (a) A sample simulation of the system, the orange curve is the simulated stochastic phase put on the phase modulator in the probe beam path, and the blue plot is the estimated feedback on the phase modulator in the LO beam path. (b) Variation of the phase error between the applied phase on the probe beam and the feedback on the LO beam as a function of measured squeezing in the system. The three curves show three different losses η on each of the beam. The lowermost curve is for a lossless system, and the uppermost curve represents a system with 75% transmission on each of the beams.

Figure 4.3 (b) presents the variation of the phase noise with the measured squeezing. Squeezing along the x-axis is increased by increasing the 4WM gain, whereas the three different curves represent the three different losses on the twin beams. The lower most plot represents no loss whereas the uppermost plot has the largest optical loss. The curves represent the results from the analytical equation (4.5). The points on the curves are the numerical analysis of simulated data obtained for the homodyne detectors and the stochastic waveform. The black plot shows the standard quantum limit obtained by replacing the probe and the conjugate beams with the coherent beams of the same power. We define the SQL in terms of the number of photons passing through the phase object placed in the probe beam arm. We see an improvement over the SQL in the tracking error. One

important point to note here is that the peak phase error achieves a minimum as a function of squeezing and further increase in the squeezing raises the error. This happens because the phase error of the tracking mixes the anti-squeezed noise with the squeezed noise in the homodyne detector signal. The process works to give an optimal squeezing for a minimum phase error [15].

In the next section, we discuss our efforts to implement the experiment and describe our progress so far.

4.1 EXPERIMENTAL SETUP

In our experimental setup, shown in Figure 4.4, we have a 4WM process that amplifies a seed beam to produce a probe and a conjugate beam. We perform a joint homodyne detection on the probe and the conjugate beams as part of our truncated SU(1,1) interferometer. In the probe beam homodyne detector, the probe beam and the LO both go through electro-optic phase modulators in their paths. We put a stochastic waveform on the electro-optic phase modulator (EOM) in the path of the probe beam using a function generator. The output of the joint homodyne detector goes through a Proportional-Integral-Differential (PID) filter to produce feedback which we put on the EOM in the path of the LO beam. Meanwhile, we lock the phase of the conjugate beam homodyne detector to measure the phase quadrature of the conjugate beam.

We also lock the probe homodyne detector using a 3-axis piezo-electric mirror to measure the phase quadrature of the probe beam. This lock is made at near dc frequencies, i.e., DC to less than 300 Hz. This is made to make sure we suppress

all the low frequency environmental noise. The bandwidth of this low frequency lock is much less than the bandwidth of the stochastic waveform (10 KHz) that we put on the EOM in the path of the probe beam.

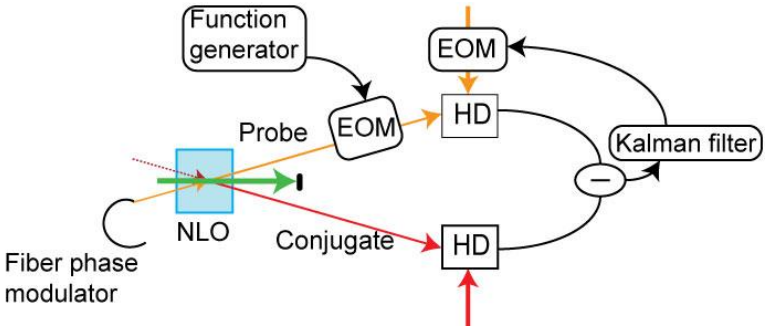

Figure 4.4: Schematic of an experimental setup. A 4WM process amplifies a seed beam to give a probe beam and produces a conjugate beam. The seed probe beam comes from a fiber phase modulator, which produces a single side-band at 1 MHz on the seed probe beam. We perform a joint homodyne detection on the probe and the conjugate beams. In the probe homodyne detector, the probe and the LO both go through electro-optic modulators placed in their respective paths. We put a stochastic waveform on the probe beam phase modulator using a function generator, and we provide a feedback signal on the phase modulator in the path of the LO beam. Meanwhile, the conjugate beam homodyne detector is locked to measure the conjugate beam phase quadrature.

To perform the phase tracking experiment, we put a single sideband on the seed of the 4WM process with a 1 MHz frequency shift from the carrier. We use this sideband frequency for the signal in the joint homodyne detector for the phase tracking. We use the carrier for DC locking of the probe beam homodyne detector. Since the sidebands are 1MHz shifted from the carrier, we electronically demodulate the output of the joint homodyne quadrature at 1 MHz before sending the output to a low pass filter which generates feedback for the EOM in the path of

the LO beam. We generate a sideband at 1 MHz because we can achieve decent quadrature squeezing at that frequency.

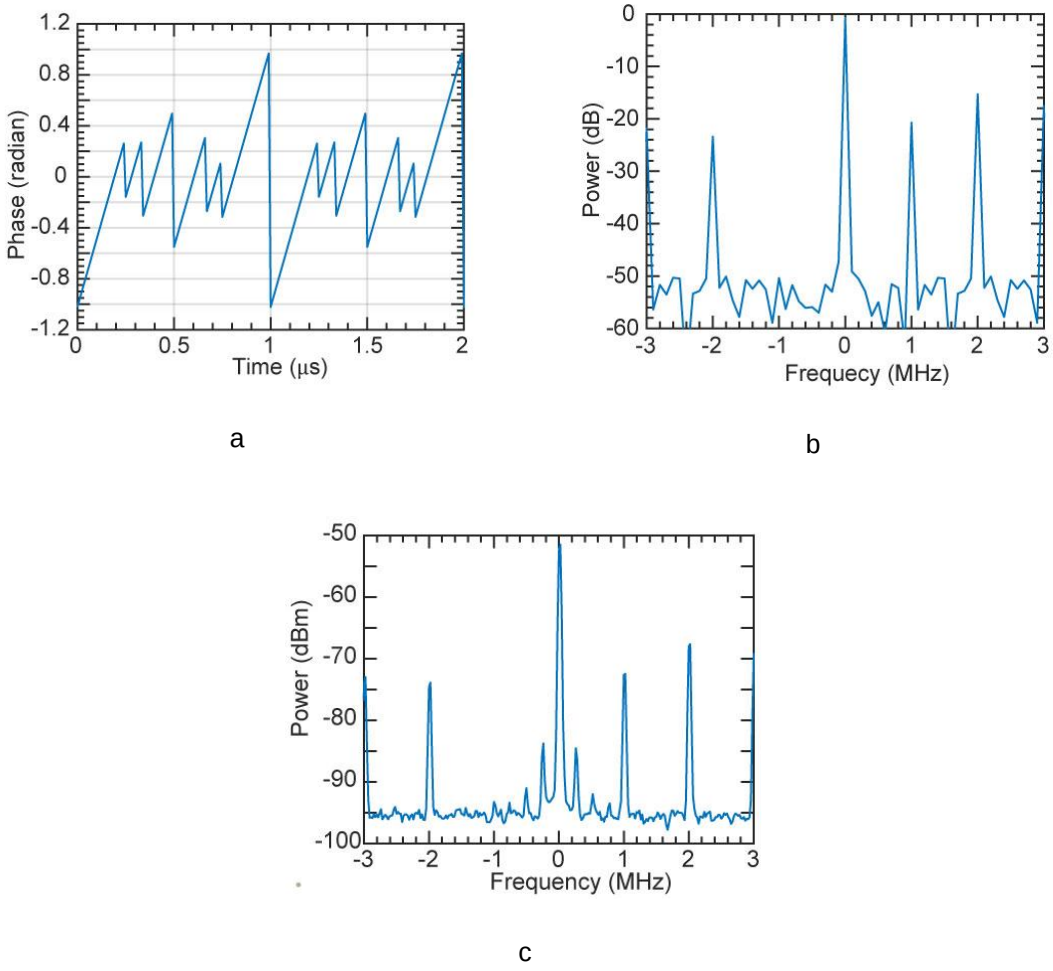

a

b

c

Figure 4.5:(a) Phase pattern put on the fiber phase modulator for single sideband generation at 1MHz. (b) Theoretical power (Fourier) spectrum of the light field after applying the phase pattern in part (a). (c) Experimental data showing the power spectrum of light from the fiber phase modulator modulated with the phase pattern shown in part (a). The power in the sideband at -1 MHz is suppressed by more than 25 dB. We provide the experimental setup for measuring the phase sideband spectrum in Appendix C.

To generate a single sideband, we put the seed through a fiber phase modulator and apply the waveform shown in Figure 4.5 (a). We show the power spectrum of our light in Figure 4.5 (c), the spectrum matches very well with the theoretical expectation shown in Figure 4.5 (b). The phase pattern in Figure 4.5 (a) is a superposition of sawtooth phase patterns with different frequencies (multiples of 1 MHz). Recently, we have been able to use more sophisticated algorithms to obtain phase patterns which give us better control of the ratio of the powers in different sidebands.

Another important task is to measure the power of light in the 1 MHz sideband. We use heterodyne detection for this purpose. We provide a derivation of the relation between the measured optical power to the observed signal to noise ratio (SNR) of the heterodyne detector in Appendix C. Figure 4.6 shows a sample measurement of ~750 fW (femto watt) optical power with a heterodyne detector. Based on the theoretical simulations using our typical experimental parameter (4WM gain and the optical loss) values, we would like to use a sideband power of ~500 fW to experimentally observe the effect of excessive squeezing, shown in Figure 4.3 (b), while beating the SQL.

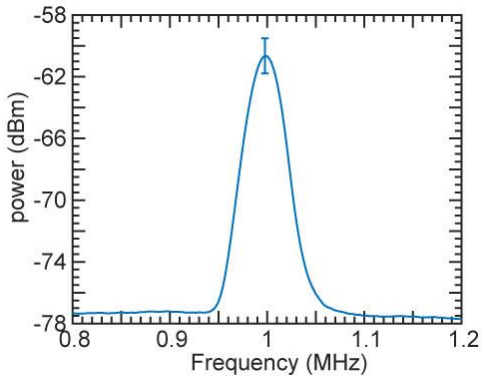

Figure 4.6: Sample heterodyne detector measurement. The SNR represents a power measurement of ~750 femto-watt. The error bar length of ~1.14 dB represents an uncertainty of ~53 fW on either side of the mean, i.e., 750 $\pm$ 53 fW.

4.2 CURRENT STATUS OF THE EXPERIMENT

We have been able to produce a single sideband on a carrier frequency. We are using this frequency to perform the phase tracking experiment. We obtained some results in the experiment regarding tracking the phase of the probe beam with the LO, but we haven't observed anything better than the SQL yet.

Moreover, as mentioned earlier, we used a PID filter instead of the Kalman filter in our experiment. We are also implementing a design of Kalman filter, theoretically which would give a better tracking result over a PID filter. We have finished the software design of the Kalman filter and are trying to implement its hardware on a circuit board.

Our next goals are to observe the results of tracking using a PID filter and then replace the PID filter with our design of the Kalman filter to track the phase of the probe beam. The aim here is to reduce the phase tracking error below the SQL.

5 Conclusion

In this thesis, we studied the generation of a two-mode squeezed state of light in hot ^{85}Rb vapor. We discussed the measurement of squeezing using a homodyne detector. We analyzed various parameters that affect the measurement of squeezing, especially optical losses, and additions of excess noise from various sources. We saw the effects of the imbalance in the transmittance and the reflectance of the 50:50 beam splitter in a homodyne detector, the excess noise due to the electronic noise of the detectors, and the phase noise between the probe and the conjugate beams and their respective LOs. Unlike the OPO system, we ruled out the phase noise as a limiting factor in measuring higher squeezing in our setup.

We studied the addition of destructive excess noise due to imperfect visibility in our homodyne detectors causing coupling of independent thermal modes into the measurement. We concluded, based on our experimental data and theoretical analysis, that the loss of visibility in our homodyne detectors is the main source for limiting the squeezing measured in our experiments. We tried to improve the visibility by mode shaping the LO beams to match the probe and the conjugate. We successfully implemented the independent matching of the phase and the intensity profile of the probe LO with the probe beam using an SLM. Our technique hasn't worked for matching the phase and the intensity profile simultaneously. We showed the imperfection of our SLM, i.e., less than 2π achievable phase modulation, as a cause. Moreover, we also suggested the use of a higher resolution wavefront sensor in performing wavefront matching. We pointed to more

sophisticated algorithms to correct the phase and the intensity profile simultaneously, which should be used with a better SLM.

We also made some technical improvements in our setup by introducing 3-axis piezoelectric mirrors and by reducing the effect of thermal air currents. The techniques helped us to improve the phase locking of the homodyne detectors and to stabilize the measurement of squeezing.

In Chapter 3, we discussed the use of a two-mode squeezed state in interferometry. We explained an SU(1,1) interferometer and the various detection schemes that can saturate the Quantum Cramer Rao bound (QCRB), and hence can theoretically reach the maximum phase sensitivity achievable with a two-mode squeezed state. We suggested a modification in the design of an SU(1,1) interferometer, and we called it a truncated SU(1,1) interferometer. We showed theoretically that the truncated version could achieve the same phase sensitivity as that of a conventional SU(1,1) interferometer, and hence saturate the QCRB for the two-mode squeezed state. We performed an experiment and showed a ~4 dB SNR improvement over the SQL in phase measurement.

We also showed theoretically that the homodyne detections in both the seeded SU(1,1) interferometer and the truncated version saturate the QCRB asymptotically, but not at small 4WM gain values. We suggested a modification in the measurement by introducing a gain factor on the conjugate homodyne detector before combining with the probe homodyne detector output. Theoretically, the scheme was successful in saturating the QCRB at all 4WM gain values. Also, we

experimentally showed an improvement in the SNR measurement with our truncated SU(1,1) interferometer using this scheme.

We also implemented a truncated SU(1,1) interferometer with vacuum seed in both the input ports of our 4WM source. We performed an experiment to measure phase sensitivity with vacuum squeezed light. Experimentally, we are still ~1 dB away from the SQL. This happens because the homodyne detection is not an optimal measurement for phase sensing with a two-mode vacuum squeezed state which we showed theoretically. With theoretical simulations using our experimental parameters, we estimated a minimum requirement of 5.5 dB of measured squeezing to beat the SQL, which is higher than the squeezing we measure in our lab. In the future, our effort would be to use the methods discussed in Chapter 2 to improve the visibility of our homodyne detectors and hence measure better squeezing. Higher squeezing would help us get a phase sensitivity improvement over the SQL.

In Chapter 4, we discussed the measurement of an unknown phase. Unlike Chapter 3, where we measured a small phase modulation around a known fixed phase, here we are trying to measure an unknown phase. The goal is to measure the phase placed in one arm of an interferometer with the help of a controllable phase in the other arm. We apply feedback on the controllable phase to track the unknown phase. We perform the experiment in our truncated SU(1,1) interferometer for tracking an unknown stochastic phase with ~10KHz bandwidth. The goal here is to reduce the phase error below the SQL using our two-mode squeezed state. We described the experimental setup we built for tracking the

phase of light in Chapter 4. We also talked about some necessary preliminary power measurements using heterodyne detectors and a generation of single sideband on a carrier using an electro-optic phase modulator. The next task in the experiment is to align the system properly to measure squeezing and take the first set of data for tracking the stochastic phase of the light.

In the future, instead of measuring the stochastic waveform, we could also try to measure a large fixed phase shift. The experiment would require another adaptive algorithm based on Bayesian analysis [16]. Again, the goal here would be to show an improvement in phase measurement over the SQL using a truncated SU(1,1) interferometer.

List of publications:

1. Prasoon Gupta, Bonnie L Schmittberger, Brian E Anderson, Kevin M Jones, Paul D Lett. Optimized phase sensing in a truncated SU (1, 1) interferometer. Optics Express, vol. 26, issue 1, pages 391-401, 2018.
2. Brian E Anderson, Prasoon Gupta, Bonnie L Schmittberger, Travis Horrom, Carla Hermann-Avigliano, Kevin M Jones, Paul D Lett. Phase sensing beyond the standard quantum limit with a variation on the SU (1, 1) interferometer. Optica, vol 4, issue 7, pages 752-756, 2017.
3. Brian E Anderson, Bonnie L Schmittberger, Prasoon Gupta, Kevin M Jones, Paul D Lett. Optimal phase measurements with bright-and vacuum-seeded SU (1, 1) interferometers. Physical Review A, vol. 95, issue 6, pages 063843, 2017
4. Prasoon Gupta, Travis Horrom, Brian E Anderson, Ryan Glasser, Paul D Lett. Multi-channel entanglement distribution using spatial multiplexing from four-wave mixing in atomic vapor. Journal of Modern Optics, vol. 63, issue 3, pages 185-189, 2016

The work in this thesis is based on the first three publications in the above list and the rest is unpublished work.

Appendix A

A.1 Derivation of the effect of imbalance in 50:50 beam splitter on the squeezing measurement

For a 50:50 beam splitter, the transmittance ($|t_1|^2$) and the reflectance ($|r|^2$) are equal, given by $\frac{1}{2}$. For most real beam splitters this ratio is somewhat off from the perfect value and could be given by $\frac{1}{2}+\varepsilon$, and $\frac{1}{2}-\varepsilon$.

We start with a homodyne detector where a signal beam with an electric field given by, α_{Sig}, overlaps with an LO with amplitude and phase goven by, $\alpha_{LO}e^{i\phi}$. We assume $|\alpha_{LO}| \gg |\alpha_{Sig}|$ in the homodyne detector. We measure the quadrature of the signal beam by taking a difference between the two ports of the beam splitter. Without losing generality, we can define the reflection and the transmittance coefficient of the beam splitter as, $r_1 = r_2 = re^{i\theta}$, and $t_1 = t_2 = t$. For simplicity, we have considered the reflectance and transmittance of the both the ports equal. We consider a small imbalance between the transmittance and the reflectance of the beam splitter, i.e., $|t_1|^2 = |t_2|^2 = |t^2| = \frac{1}{2}-\varepsilon$, and $|r_1|^2 = |r_2|^2 = |r^2| = \frac{1}{2}+\varepsilon$.

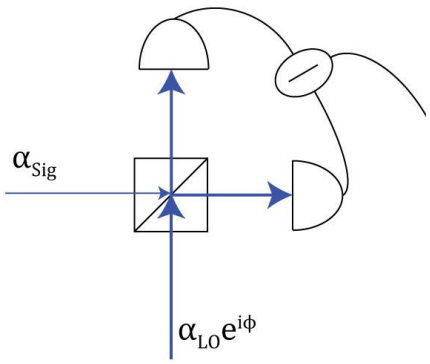

Figure A.1: Homodyne detector with an imbalanced 50:50 beam splitter.

The power in the two ports of the beam splitter are given by

$$P_1 = |r|^2|\alpha_{LO}|^2 + |t|^2\left|\alpha_{sig}\right|^2 + 2|r||t||\alpha_{LO}|\left|\alpha_{Sig}\right|\cos(\phi+\theta)\,, \qquad (A.1)$$

$$P_1 = |t|^2|\alpha_{LO}|^2 + |r|^2\left|\alpha_{sig}\right|^2 - 2|r||t||\alpha_{LO}|\left|\alpha_{Sig}\right|\cos(\phi+\theta)\,. \qquad (A.2)$$

The difference output is given by

$$\Delta P = (|r|^2 - |t|^2)\left(|\alpha_{LO}|^2 - \left|\alpha_{Sig}\right|^2\right) + 4rt|\alpha_{LO}|\left|\alpha_{Sig}\right|\cos(\phi+\theta)\,. \qquad (A.3)$$

For $|\alpha_{LO}| \gg |\alpha_{Sig}|$ and using $|t|^2 = \frac{1}{2} + \varepsilon$, and $|r|^2 = \frac{1}{2} - \varepsilon$,

$$\Delta P = 2\varepsilon(|\alpha_{LO}|^2) + 4\sqrt{\frac{1}{4} - \varepsilon^2}|\alpha_{LO}|\left|\alpha_{Sig}\right|\cos(\phi+\theta)\,. \qquad (A.4)$$

Now, we can separate the LO power into a DC and an AC term, $\alpha_{LO} = \alpha_{LO}^{DC} + \Delta\alpha_{LO}$. The DC term, α_{LO}^{DC}, represents the amplitude and the AC term, $\Delta\alpha_{LO}$, shows the noise on the beam, the amplitude noise.

We can rewrite equation $(A.4)$ with the DC and AC term of the LO beam separated,

$$\Delta P = 2\varepsilon\left(\left|\alpha_{LO}^{DC} + \Delta\alpha_{LO}\right|^2\right) + 4\sqrt{\frac{1}{4} - \varepsilon^2}\left(\left|\alpha_{LO}^{DC}\right| + \Delta\alpha_{LO}\right)\left|\alpha_{Sig}\right|\cos(\phi+\theta)\,. \qquad (A.5)$$

Now for an LO, the DC power is much higher than the amplitude noise on it, i.e., $\left|\alpha_{LO}^{DC}\right| \gg |\Delta\alpha_{LO}|$. We can keep the first order terms in $\Delta\alpha_{LO}$ and rewrite equation $(A.5)$,

$$\Delta P = 2\varepsilon\left(\left|\alpha_{LO}^{DC}\right|^2\right) + 4\varepsilon\left|\alpha_{LO}^{DC}\right|\Delta\alpha_{LO} + 4\sqrt{\frac{1}{4} - \varepsilon^2}\left(\left|\alpha_{LO}^{DC}\right|\right)\left|\alpha_{Sig}\right|\cos(\phi+\theta).$$

Rewriting the above equation

$$\Delta P = 2\varepsilon\left(\left|\alpha_{LO}^{DC}\right|^2\right) + 4\sqrt{\frac{1}{4}-\varepsilon^2}\left(\frac{\varepsilon}{\sqrt{\frac{1}{4}-\varepsilon^2}}\Delta\alpha_{LO} + \left|\alpha_{Sig}\right|\cos(\phi+\theta)\right)\left|\alpha_{LO}^{DC}\right|. \quad (A.6)$$

Now the term $2\varepsilon\left(\left|\alpha_{LO}^{DC}\right|^2\right)$ is a DC value so it does not contribute to the noise properties. We can see that the 2nd term $\frac{\varepsilon}{\sqrt{\frac{1}{4}-\varepsilon^2}}\left|\alpha_{LO}^{DC}\right|\Delta\alpha_{LO}$ adds excess noise to the quadrature noise of the signal beam. We can calculate the power of the 2nd term, and give the excess noise as the ratio of the power of the 2nd term to the 3rd term as

$$\Delta N_{excess} = \frac{\varepsilon^2}{\frac{1}{4}-\varepsilon^2}\,\Delta^2\alpha_{LO}. \quad (A.7)$$

For $\varepsilon \ll \frac{1}{2}$, we can write the above equation as

$$\Delta N_{excess} = \frac{16\varepsilon^2\Delta^2\alpha_{LO}}{\Delta^2 X_{Sig}}. \quad (A.8)$$

Since we measure the joint quadrature of the probe and the conjugate, we sum the homodyne detector outputs of the two beams. The excess noise in our case would be

$$\Delta N_{excess} = \frac{16\varepsilon^2\left(\Delta^2\alpha_{LO}^{p} + \Delta^2\alpha_{LO}^{c}\right)}{\Delta^2 X_{Sig}}, \quad (A.9)$$

where $\Delta\alpha_{LO}^{p}$ and $\Delta\alpha_{LO}^{c}$ are the amplitude noises of the probe and the conjugate local oscillator.

We can also note one more point here. Since we always measure the squeezing compared to the shot noise. Our measurement of the shot noise will also be worse if we have a beam splitter imbalance. The excess noise added to the shot noise measurement will be fractionally less than that added to the squeezed quadrature noise. We can use the above equations to exactly compute the squeezing. We should add excess noise in both the shot noise measurement and the squeezed noise measurement and then take the ratio of two noises.

A.2 Calibration of the SLM

Here we provide an explanation and results for the phase characterization of an SLM. We show our experimental setup for the phase characterization in Figure A.2. We reflect a beam off our SLM at an angle of less than 10^{o}, as recommended by the manufacturer. The beam is polarized at an angle of 45^{o} in the $x - y$ plane, i.e., orthogonal to the direction of the beam propagation. The SLM affects the polarization along the y-direction only and does not provide phase modulation to the x polarization. We place a polarizing beam splitter (PBS) in the reflected beam and put the beam from one of the ports onto a detector, which measures the power of the beam.

When the SLM puts a phase shift onto the y-polarized part of the beam, the effective polarization of the entire beam changes. We can represent the beam before it falls on the SLM as

$$\vec{E} = E_o\hat{x} + E_o\hat{y}. \qquad (A.10)$$

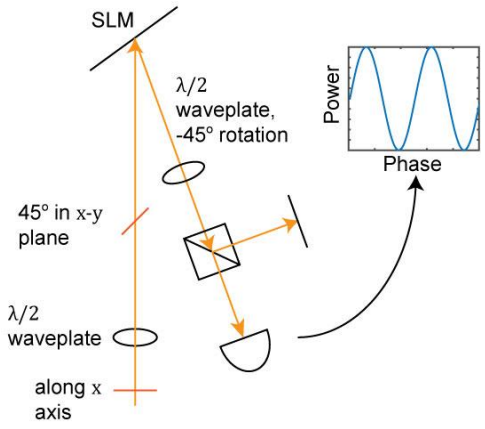

Figure A.2: Experimental setup for the characterization of an SLM. A waveplate rotates the polarization of an x-polarized beam to be at angle of 45° with the polarization axis of the SLM (perpendicular to the plane of the figure). After reflection from the SLM, another waveplate rotates the polarization of the beam by -45°. The beam passes through a polarizing beam splitter and falls on a diode for detection.

After reflection from the SLM, the electric field is given by

$$\vec{E} = E_o \hat{x} + E_o e^{i\phi} \hat{y}. \qquad (A.11)$$

Depending on the phase ϕ, the polarization of the beam could be linear, elliptic, or circular. If we rotate the polarization of the beam by 45°, the field becomes

$$\vec{E} = \frac{E_o}{\sqrt{2}}(\hat{x} + \hat{y}) + \frac{E_o}{\sqrt{2}} e^{i\phi}(\hat{x} - \hat{y}),$$

which can be re-written as

$$\vec{E} = \left(\frac{E_o}{\sqrt{2}} + \frac{E_o}{\sqrt{2}} e^{i\phi}\right)\hat{x} + \left(\frac{E_o}{\sqrt{2}} - \frac{E_o}{\sqrt{2}} e^{i\phi}\right)\hat{y}.$$

If we place a PBS into the beam with the y-axis as the transmission axis and detect the transmitted power, we will observe

$$P = \left| \frac{E_o}{\sqrt{2}} - \frac{E_o}{\sqrt{2}} e^{i\phi} \right|^2 = E_o^2 (1 - \cos\phi). \qquad (A.12)$$

We can see that the above power is a sinusoidal function of the phase retardation ϕ applied by the SLM. Hence as we change the value of the applied voltage on the SLM (eight-bit binary value), we can measure the power and hence calibrate the phase retardation with the applied binary value on the SLM.

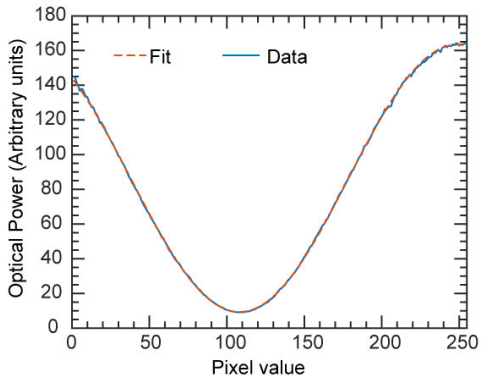

Figure A.3: Calibration data for the SLM. The blue curve shows the optical power in the transmitted PBS port, and the maroon curve shows the sine fit based on equation $(A.12)$. The y-axis shows the pixel value of the flat wavefront that we put on the SLM. We did not consider the surface flatness correction for SLM head while doing this calibration, because of the less than 2π phase shift availability.

We show the calibration data for our SLM in Figure A.3. We fit the experimental data with equation $(A.12)$, and find the range of phase modulation to be $\sim 1.823\pi$ radians.

A.3 Possible automation in the experimental setup

We mentioned in Chapter 1 that we produce local oscillators in our experiment using a seeded 4WM process. The process amplifies the seed beam to give a

probe and produces a conjugate beam. If we seed the process with a probe seed beam with a power $|\alpha_o|^2$ in a 4WM system with gain G, the power of the probe and the conjugate are $G|\alpha|$, and $(G-1)|\alpha_o|^2$ respectively. We can see that the two beams are different in power. If we use these beams in our joint homodyne detector, we get the following measurement

$$X = |\alpha_{LO}|\left(\sqrt{G}X_p + \sqrt{G-1}X_c\right), \tag{A.13}$$

where X_p and X_c are the probe and the conjugate beam quadrature operators. We can re-write the equation $(A.13)$ as

$$X = |\alpha_{LO}|\sqrt{G-1}\left(\frac{\sqrt{G}}{\sqrt{G-1}}X_p + X_c\right). \tag{A.14}$$

We can see from equation $(A.14)$ that when we use a 4WM generated probe and conjugate beam LO, we get a weighted joint quadrature operator and not the joint phase sum quadrature that we desire in our experiment. This gives an excess noise in our detection and reduces the measured squeezing. Though we can get rid of the excess probe power easily, it requires extra optics and has the potential to bring in orthogonal polarization in the LO which could add excess noise. There is another easier way to do this via electronics. We have already shown some measurements in Chapters 1 and 2 by electronically attenuating the output of a homodyne detector. We can put an electronic gain of $\kappa = \frac{\sqrt{G-1}}{\sqrt{G}}$ on the probe beam homodyne detector output to measure the desired sum quadrature operator.

Now, in our experimental setup, we have different losses on the probe and the conjugate beams. Hence the ratio of the power of the two beams is not necessarily

defined by the gain of the 4WM. In our lab, we could measure the power of the individual LO beams and make them equal. We do not measure their powers directly, instead we check the shot noises of individual homodyne detectors. If the shot noises of both the homodyne detectors aren't equal, we make them equal by using an electronic attenuation/gain.

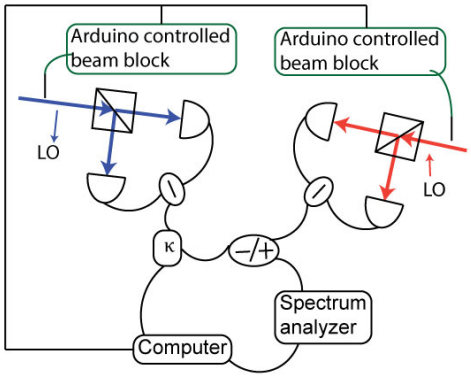

Figure A.4: Experimental setup for the automation of balancing the weights of the two homodyne detectors.

We can also automate the above process by using the standard electronic equipment, as shown in Figure A.4. We use two Arduino controlled beam blocks to block the two LO beams, one at a time. We measure the shot noise from each homodyne detector and calculate the ratio of the two powers. Depending on the ratio, we apply a feedback attenuation, which could be an easily available/home built current controlled attenuator.

We give a short description for making a quick current controlled attenuator using an electronic mixer. One way to make an electronic attenuator is to apply a dc current in the IF port of a mixer and apply the input power in the LO port. The attenuation of the output through the RF port depends inversely on the current

applied through the IF port. We also show a characterization of a sample attenuator we made in our lab. We include a theoretical fit $\kappa = A/(V - B)$, where V is the applied potential across the IF port.

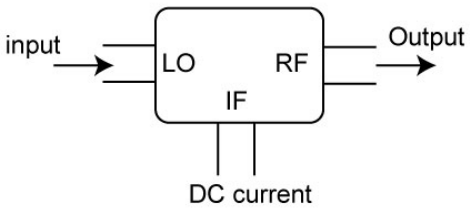

a

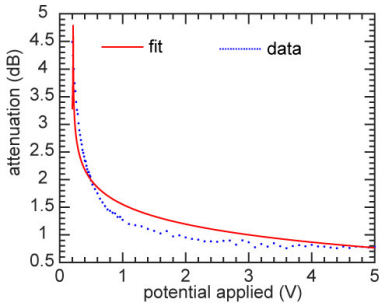

b

Figure A.5: (a) Schematic for an electronic attenuator using an electronic mixer. We apply the input to the LO port and dc current to the IF port of the electronic mixer. The attenuation of the output through the RF port is inversely proportional to the applied current. (b) Characterization of an electronic attenuator including a theoretical fit with $\kappa = A/(V - B)$, where V is the applied DC potential.

Appendix B

B.1 Deriving the phase sensitivity

We gave phase uncertainty expressions in Chapter 2 for multiple detection schemes. We provide here some explanation for how those expressions were calculated. We evaluated those expressions with the use of a Mathematica package for non-commuting variables [71]. We have provided much of this discussion in our publications [50, 53].

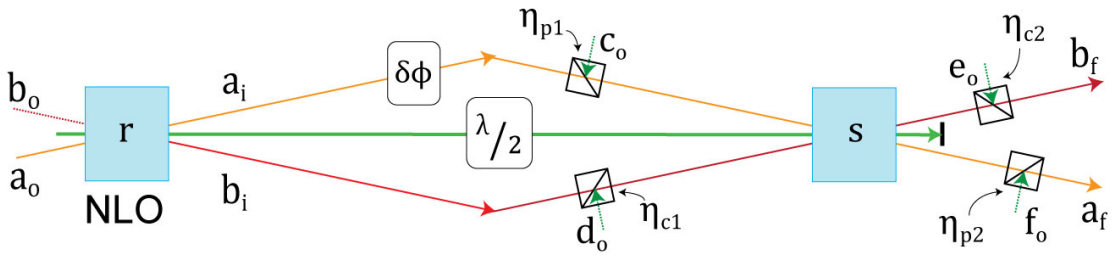

Figure B.1: Schematic of an SU(1,1) type interferometer. η_{p1}, η_{c1}, η_{p2}, and η_{c2} are the internal and the external losses on the probe and the conjugate beams respectively. The states c_o, d_o, e_o, and f_o are vacuum states coupling with the quantum states as a result of the loss. The r and s are the squeezing parameters of the 1st and the 2nd NLO media, related to the gain of the media by $G_r = \cosh^2(r)$, and $G_s = \cosh^2(s)$, where G_r and G_s are the gains of the two NLO media.

We start our discussion by providing a schematic of an SU(1,1) interferometer (Figure B.1), similar to the one that we used in Chapter 2. There are two input states a_o and b_o, which after passing through the 1st NLO medium of the interferometer become the states a_i and b_i. The state a_i goes through a phase shift ϕ. Both the states a_i and b_i suffer losses η_{p1} and η_{p2} before mixing with a pump beam inside the 2nd NLO medium. The loss is represented by a beam splitter with

a transmissivity (η_{p1} or other similar expressions) whose other port mixes vacuum (c_o, d_o, and others) with the input beam. The 2nd NLO performs its operations on the two input beams and produces two output modes. The two modes thus produced, may suffer a loss at the detection stage.

To relate the final output a_f and b_f to the inputs a_o and b_o, we need the mathematical representations of various process on the beam path. We start with the 4WM (two-mode squeezer), which is given by [53, 19, 72]

$$U = \begin{pmatrix} \cosh(r) & 0 & 0 & \sinh(r) \\ 0 & \cosh(r) & \sinh(r) & 0 \\ 0 & \sinh(r) & \cosh(r) & 0 \\ \sinh(r) & 0 & 0 & \cosh(r) \end{pmatrix} \tag{B.1}$$

We can describe the initial modes with the annihilation operators a_o and b_o, and put them in a column vector as

$$v = \begin{pmatrix} a_o \\ a_o^\dagger \\ b_o \\ b_o^\dagger \end{pmatrix}. \tag{B.2}$$

We can write the transformation using the 4WM system as

$$\begin{pmatrix} a_1 \\ a_1^\dagger \\ b_1 \\ b_1^\dagger \end{pmatrix} = Uv. \tag{B.3}$$

Similarly, we can take into account the effect of losses and the effect of the 2nd NLO medium in an SU(1,1) interferometer. In case of a truncated SU(1,1) interferometer, there is no 2nd NLO medium and hence $s = 0$. We derive

expressions for the quantum states a_f and b_f by operating on the term in equation $(B.3)$ with the loss and the 2nd NLO matrices. We provide here the final expressions for the states a_f and b_f in terms of known experimental parameters in equations $B.4)$ and $B.5)$.

$$\hat{a}_f = i\hat{e}_o\sqrt{1-\eta_{p2}} + \sqrt{\eta_{p2}}\Big\{\cosh(s)\Big[i\hat{c}_o\sqrt{1-\eta_{p1}} + \sqrt{\eta_{p1}}\big(\hat{a}_o e^{i\phi}\cosh(r) + e^{i\phi}\sinh(r)\,\hat{b}_o^{\dagger}\big)\Big] - \sinh(s)\Big[\sqrt{\eta_{c1}}\big(\hat{a}_o\sinh(r) + \cosh(r)\,b_o^{\dagger}\big) - i\sqrt{1-\eta_{c1}}d_o^{\dagger}\Big]\Big\}, \qquad (B.4)$$

$$\hat{b}_f = i\hat{f}_o\sqrt{1-\eta_{c2}} + \sqrt{\eta_{c2}}\Big\{\cosh(s)\Big[i\hat{d}_o\sqrt{1-\eta_{c1}} + \sqrt{\eta_{c1}}\big(\hat{b}_o\cosh(r) + \sinh(r)\,\hat{a}_o^{\dagger}\big)\Big] - \sinh(s)\Big[\sqrt{\eta_{p1}}\big(\hat{b}_o e^{-i\phi}\sinh(r) + e^{-i\phi}\cosh(r)\,\hat{a}_o^{\dagger}\big) - i\sqrt{1-\eta_{p1}}\hat{c}_o^{\dagger}\Big]\Big\}. \qquad (B.5)$$

We can use the expressions for $\hat{a}_f$ and $\hat{b}_f$ for calculating the sensitivities of various detection schemes. For example, the sensitivity for the detection with the total photon number operator, $\widehat{M}_N = \hat{a}_f^{\dagger}\hat{a}_f + \hat{b}_f^{\dagger}\hat{b}_f$, is given by

$$\Delta^2\phi = \frac{\langle\Delta^2\widehat{M}_N\rangle}{\partial_\phi\langle\widehat{M}_N\rangle}. \qquad (B.6)$$

The quantities mentioned in equation $(B.6)$, can be expressed using the expressions for $\hat{a}_f$ and $\hat{b}_f$,

$$\langle \widehat{M}_N \rangle = \langle \hat{a}_f^\dagger \hat{a}_f + \hat{b}_f^\dagger \hat{b}_f \rangle,$$

$$\Delta^2 \widehat{M}_N = \langle \widehat{M}_N^2 \rangle - \langle \widehat{M}_N \rangle^2 = \left\langle \left(\hat{a}_f^\dagger \hat{a}_f + \hat{b}_f^\dagger \hat{b}_f \right)^2 \right\rangle - \left(\langle \hat{a}_f^\dagger \hat{a}_f + \hat{b}_f^\dagger \hat{b}_f \rangle \right)^2. \quad (B.7)$$

We can use equation $(B.7)$ to get the sensitivity of the photon number ($\widehat{M}_N$) measurement, shown in equation (3.4). We are not putting the expression here to avoid verbosity. Similarly, we can calculate the expressions for the sensitivities of other detection schemes.

We tested all our evaluations with the end cases and in the limits of a coherent beam and other intuitive results. All these tests yielded positive results. Additionally, we compared our computations with many results available in the literature, which matched our calculations.

B.2 Derivation of phase sensitivity for a Mach-Zehnder interferometer

We used, in Chapter 2, the expressions relating the electrical signals from the devices to the phase sensitivity of our interferometer. Here we derive those expressions. Figure B.2 shows a schematic of a homodyne detector.

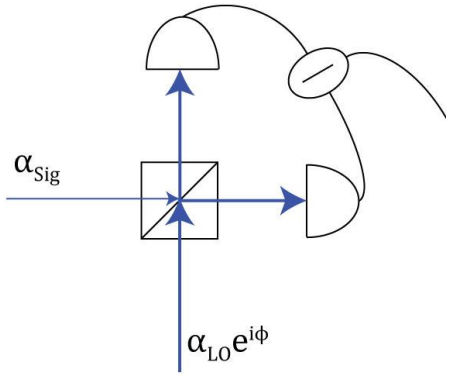

Figure B.2: Homodyne detector with the signal beam α_{Sig} overlapping with a local oscillator $\alpha_{LO}e^{i\phi}$. The power in the LO beam is much higher than the signal beam, i.e., $|\alpha_{LO}| \gg |\alpha_{sig}|$.

We can describe the output in the two ports of the 50:50 beam splitter by the equations

$$P_1 = \frac{1}{2}\left(\left|\alpha_{Sig}\right|^2 + |\alpha_{LO}| + 2\left|\alpha_{Sig}\right||\alpha_{LO}|\cos(\phi)\right),$$

$$P_2 = \frac{1}{2}\left(\left|\alpha_{Sig}\right|^2 + |\alpha_{LO}| - 2\left|\alpha_{Sig}\right||\alpha_{LO}|\cos(\phi)\right).$$

We subtract one output of the beam splitter from the other to give

$$\Delta P = 2\left|\alpha_{Sig}\right||\alpha_{LO}|\cos(\phi).$$

Now given the power P_1 and P_2 falling on the diodes, the electrical current generated by the detectors is given by $i = \rho(P_1 + P_2)$, where ρ is the responsivity of the detectors. We can find the difference current generated by the diodes, as

$$i = \rho\Delta P = 2\rho\left|\alpha_{Sig}\right||\alpha_{LO}|\cos(\phi)\,. \qquad (B.8)$$

Since we try to measure the signal to noise ratio (SNR) of the measurement, we must measure the power of the associated signal. Power of the difference current as measured across a resistor (R) is

$$P_{elec} = i^2R = 4R\rho^2\left|\alpha_{Sig}\right|^2|\alpha_{LO}|^2\cos^2(\phi)\,. \qquad (B.9)$$

Now we try to measure a small modulation $\delta\phi$ around a fixed phase ϕ_o. We can put $\phi = \phi_o + \delta\phi$ in equation $(B.9)$ to get

$$P_{elec} = 4R\rho^2\left|\alpha_{Sig}\right|^2|\alpha_{LO}|^2\cos^2(\phi_o + \delta\phi).$$

For small $\delta\phi$, the above equation can be written as

$$P_{elec} = 4R\rho^2\left|\alpha_{Sig}\right|^2|\alpha_{LO}|^2\sin^2(\phi_o)\,(\delta\phi)^2. \qquad (B.10)$$

Using a sinusoidal modulation $\delta\phi = \sqrt{2}\delta\phi_o\sin(\Omega t)$, we can write the equation $(B.10)$ as

$$P_{elec} = 4R\rho^2\left|\alpha_{Sig}\right|^2|\alpha_{LO}|^2\sin^2(\phi_o)\,(\delta\phi_o)^2 2\langle\sin^2(\Omega t)\rangle.$$

Here $\langle\sin^2(\Omega t)\rangle$ is the expectation value of $\sin^2(\Omega t)$, which is $\frac{1}{2}$. Putting this in the above equation gives an expression for the modulation signal power, given by equation $(B.11)$,

$$P_{elec} = 4R\rho^2\left|\alpha_{Sig}\right|^2|\alpha_{LO}|^2\sin^2(\phi_o)\,(\delta\phi_o)^2\,. \qquad (B.11)$$

Since we observe the signal to noise ratio (SNR) of the measurement, we need an expression for the noise. For a coherent beam, the photon number has a Poisson distribution, which manifests itself in the current produced by the detectors. For a power P of light falling on a diode, the noise power in the current is given by, $\Delta P_{elec} = 2eiBR$ [31], where e and B are the electronic charge and measurement bandwith. The total noise generated by the two diodes in the homodyne detector is

$$\Delta P_{elec} = 2eBR(P_1 + P_2) = 2eBR\rho|\alpha_{LO}|^2. \qquad (B.12)$$

The above equation assumes $|\alpha_{LO}| \gg |\alpha_{Sig}|$. We can compute the SNR of the measurement using equations $(B.11)$ and $(B.12)$,

$$\mathrm{SNR} = \frac{\mathrm{P_{elec}}}{\Delta \mathrm{P_{elec}}} = \frac{2\rho\left|\alpha_{\mathrm{Sig}}\right|^2(\delta\phi_o)^2}{\mathrm{eB}}. \qquad (\mathrm{B.13})$$

We can use the SNR of the measurement from a device like a spectrum analyzer, and use the SNR to estimate $\delta\phi_o$ from equation $(\mathrm{B.13})$.

B.3 Geometric description of an SU(1,1) interferometer

The Lie Algebra corresponding to the group SU(1,1) is spanned by the three operators $\{K_x, K_y, K_z\}$. The operators satisfy the following commutation relations [73, 8]:

$$[K_x, K_y] = -iK_z, \qquad [K_y, K_z] = iK_x, \qquad [K_z, K_x] = iK_y.$$

We can define the raising and lowering operators for the group, given by $K_\pm = K_x \pm iK_y$, which satisfy the commutation relations given by

$$[K_-, K_+] = 2K_z, \qquad [K_z, K_\pm] = \pm K_\pm$$

The Cassimir invariant $K^2 = K_z^2 - K_x^2 - K_y^2$ is given by an identity operator $K^2 = k(k-1)I$, where k acquires discrete values given by $k = \frac{1}{2}, 1, \frac{3}{2}, 2, \ldots. k$.

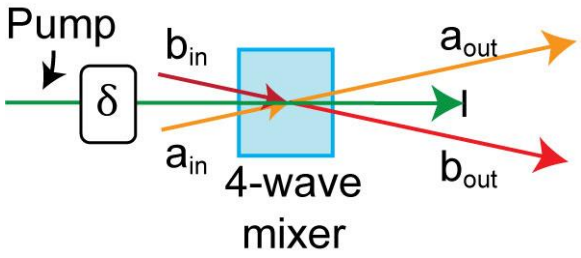

Figure B.3: A 4-wave mixer

For an 4-wave mixer with inputs and outputs shown in Figure B.3, the K operators are given by [8]:

$$K_x = \frac{1}{2}\left(a_f^\dagger b_f^\dagger + a_f b_f\right), \qquad K_y = -\frac{i}{2}\left(a_f^\dagger b_f^\dagger - a_f b_f\right), \qquad K_z = \frac{1}{2}\left(a_f^\dagger a_f + b_f^\dagger b_f\right),$$

and the corresponding raising (K_+) and lowering (K_-) operators are represented by

$$K_+ = a_f^\dagger b_f^\dagger, \qquad K_- = a_f b_f.$$

A 4-wave mixer is defined by the scattering matrix S, which transforms its two inputs to produce output states given by

$$\begin{bmatrix} a_{out} \\ b_{out} \end{bmatrix} = S \begin{bmatrix} a_{in} \\ b_{in} \end{bmatrix}, \tag{B.14}$$

$$S = \begin{bmatrix} \cosh(r) & e^{-i\delta}\sinh(r) \\ e^{i\delta}\sinh(r) & \cosh(r) \end{bmatrix},$$

where $\cosh^2(r)$ is the gain of the 4WM process, and δ is the phase of the pump beam.

S can be re-written as

$$S = \begin{bmatrix} e^{-i\delta} & 0 \\ 0 & 1 \end{bmatrix} \begin{bmatrix} \cosh(r) & \sinh(r) \\ \sinh(r) & \cosh(r) \end{bmatrix} \begin{bmatrix} e^{-i\delta} & 0 \\ 0 & 1 \end{bmatrix}, \tag{B.15}$$

Using the above scattering matrix for the 4WM process, one can write the transformations of the K operators in Heisenberg picture as:

$$\begin{bmatrix} K_x \\ K_y \\ K_z \end{bmatrix}_{out} = \begin{bmatrix} \cos(\delta) & \sin(\delta) & 0 \\ -\sin(\delta) & \cos(\delta) & 0 \\ 0 & 0 & 1 \end{bmatrix} \begin{bmatrix} \cosh(r) & 0 & \sinh(r) \\ 0 & 1 & 0 \\ \sinh(r) & 0 & \cosh(r) \end{bmatrix} \begin{bmatrix} \cos(\delta) & -\sin(\delta) & 0 \\ \sin(\delta) & \cos(\delta) & 0 \\ 0 & 0 & 1 \end{bmatrix} \begin{bmatrix} K_x \\ K_y \\ K_z \end{bmatrix}_{in}$$

$$\begin{bmatrix} K_x \\ K_y \\ K_z \end{bmatrix}_{out} = R(-\delta, z)L(2r, y)R(\delta, z) \begin{bmatrix} K_x \\ K_y \\ K_z \end{bmatrix}_{in} \tag{B.16}$$

The above matrices can be described in a light-cone like space, where the K_x and K_y are space like coordinates and K_z is a time like coordinate, with the matrices $R(-\delta, z)$: rotation about the K_z axis by δ angle, $L(2r, y)$: a Lorentz boost along the positive K_y axis, and finally $R(\delta, z)$: a rotation by $-\delta$ about the K_z axis. We can write the transformation more compactly using the notation,

$$\begin{bmatrix} K_x \\ K_y \\ K_z \end{bmatrix}_{out} = e^{i\delta K_z} e^{-2irK_y} e^{-i\delta K_z} \begin{bmatrix} K_x \\ K_y \\ K_z \end{bmatrix}_{in} e^{-i\delta K_z} e^{2irK_y} e^{i\delta K_z}.$$

Similarly, in the Schrodinger picture, this can be written as:

$$|out\rangle = e^{-i\delta K_z} e^{2irK_y} e^{i\delta K_z} |in\rangle,$$

where $|out\rangle$ and $|in\rangle$ are collective the output and the input states of the 4-wave mixer.

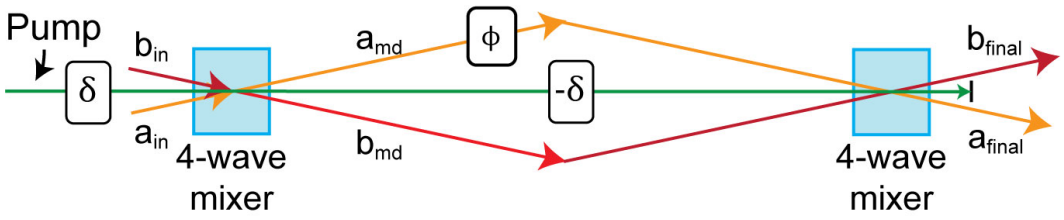

Figure B.4: Schematic of an SU(1,1) interferometer, second 4-wave mixer performs inverse of the first.

In an SU(1,1) interferometer (Figure B.4), if the pump beam phase is set to perform the inverse of the first 4-wave mixer, and the sum of the phases of the two modes inside the interferometer is given by ϕ. one can describe the entire operation using the transformation

$$K_{final} = L(2r, y)R(\phi, z)L(-2r, y)K_{in} = R(-\theta, z)L(\gamma, x)R(\theta, z)K_{in}, \qquad (B.17)$$

Where θ and γ are explicit functions of ϕ and r. The expression can be regarded as a rotation θ about K_z axis, then a Lorentz boost along the positive K_x axis, and finally a rotation of $-\theta$ about the K_z axis in a light cone space where K_x and K_y act as position coordinates and K_z acts like time coordinate. Since the interferometer can be explained using the Lorentz transformation of the K operators, which are the Lie algebra generators of SU(1,1) group, the interferometer is known as the SU(1,1) interferometer.

Similarly, a Mach-Zehnder interferometer can be described as rotations of the angular momentum operators in a 3D space which are the Lie algebra generators of SU(2) group, hence it is also given the name SU(2) interferometer. Detailed discussion on both the interferometers can be found in Yurke et al. [8].

Appendix C

C.1 Kalman Filter

In this section, we talk about the Kalman Filter, mostly the Discrete-time Kalman Filter. We use the discrete time filter for all our data analysis both experimental and simulations. The continuous time Kalman filter is used mainly to derive the equations in Chapter 3 or for finding their analytical forms. The work has been performed very well in various publications [64, 15].

A Kalman filter is defined using a state and an observation equation [46, 70]. Given the following state and observation equations:

$$s[n] = Fs[n-1] + Gu[n], \tag{C.1}$$

$$x[n] = Cs[n] + Rw[n]. \tag{C.2}$$

u and w are the Zero-mean Gaussian random process with variance 1, and n is the successive iteration of data. F, G, C, and R are the scalar constants. s is the state of the system under observation, and x is the observed output of the system. One goal here is to get an estimate of $s[n]$ based on all the past and the present data obtained from the system, i.e., $x[0] \ldots . x[n]$. A Kalman filter gives the minimum mean square error estimator of such a system [46, 70]. The exact derivation of the Kalman filter system is beyond the scope of this discussion.

To apply the Kalman Filter to our system, we must be able to put our system to the above form. Our stochastic waveform is given by

$$\phi(t) = \sqrt{\kappa}\int_{-\infty}^{t} e^{-(t-s)}dV(s)\,. \tag{C.3}$$

Differentiating the above equation gives

$$\phi(t+dt) = (1-\lambda dt)\phi(t) + \sqrt{\kappa}dV(t), \tag{C.4}$$

where $V(t)$ is a Wiener process. The distribution of $dV(t)$ is given by $dV(t)\sim\mathcal{N}(0,dt)$, where $\mathcal{N}(0,dt)$ is a normal distribution with zero mean and dt as the variance. For a normal distribution $\mathcal{N}(0,dt) = (dt)^{0.5}\mathcal{N}(0,1)$, we also define $\mathcal{N}(0,1)\sim u(t)$, we can rewrite equation $(C.4)$ as

$$\phi(t+dt) = (1-\lambda dt)\phi(t) + \sqrt{\kappa}\sqrt{dt}\,u(t). \tag{C.5}$$

We can write the signal from the homodyne detector as

$$I(t)dt = 2|\alpha|\big(\phi(t)-\phi_f(t)\big)dt + \sqrt{R_{sq}}dW(t), \tag{C.6}$$

$$R_{sq} = \sigma_f^2 e^{2r_{asq}} + \big(1-\sigma_f^2\big)e^{-2r_{sq}}, \tag{C.7}$$

where σ_f^2 is the phase variance (or error) of the tracking process, given by $\sigma_f^2 = \langle\phi(t)-\phi_f(t)\rangle^2$, R_{sq} is the noise of the joint homodyne detector as a result of the error in phase tracking, $e^{2r_{asq}}$ is the noise of the anti-squeezed quadrature, and $e^{-2r_{sq}}$ is the noise of the squeezed quadrature. $dW(t)\sim\mathcal{N}(0,dt)\sim(dt)^{0.5}\mathcal{N}(0,1)$. We can re-write equation $(C.6)$ as

$$I(t) = 2|\alpha|\big(\phi(t)-\phi_f(t)\big) + \frac{\sqrt{R_{sq}}}{\sqrt{dt}}\,\mathcal{N}(0,1). \tag{C.8}$$

We can re-write the above equation using $\mathcal{N}(0,1) \sim w(t)$ and re-arranging the terms,

$$I(t) + 2|\alpha|\phi_f(t) = 2|\alpha|\phi(t) + \frac{\sqrt{R_{sq}}}{\sqrt{dt}}\, w(t). \qquad (C.9)$$

We can compare equation $(C.9)$ with equation $(C.2)$, and equation $(C.5)$ with equation $(C.1)$. We find the equations are comparable with the substitutions:

$$\begin{bmatrix} F \\ G \\ C \\ R \end{bmatrix} = \begin{bmatrix} 1 - \lambda dt \\ \sqrt{\kappa}\sqrt{dt} \\ 2|\alpha| \\ \sqrt{\frac{R_{sq}}{dt}} \end{bmatrix}. \qquad (C.10)$$

Also, the state $s(t) = \phi(t)$, and the observation $x(t) = I(t) + 2|\alpha|\phi_f(t)$. We can apply a Kalman filter to equations $(C.5)$ and $(C.9)$ to get the minimum mean square error estimator of $\phi(t)$.

C.2 Algorithm of Kalman filtering

Once we have a state equation and an observation equation, given by equations $(C.1)$ and $(C.2)$. We can use the following algorithm to get an estimate of the state of the system ($\hat{s}(n)$) [70, 46].

Before describing the algorithm, we describe a few notations we use in the description. We use the notations $\hat{s}(n|n)$, $M(n|n)$, and $K(n)$ to represent the estimator of state s at time n, i.e., $s(n)$, the mean error in the estimation, and the Kalman gain at time n respectively. We will describe other symbols later, as required. We discuss the Kalman filter algorithm next.

We start with the initialization of the system. We assign reasonable initial values to the estimator and iteratively follow the following steps to get an estimate of the state.

1. Prediction step

$$\hat{s}(k|k-1) = F\hat{s}(k-1|k-1)$$

$\hat{s}(k|k-1)$ represents an estimation of $s(k)$ using the estimate at time $k-1$.

2. Mean square error prediction

$$M(n|n-1) = F^2M(n-1|n-1) + G^2.$$

3. Kalman Gain

$$K(n) = \frac{M(n|n-1)C}{C^2M(n|n-1) + R^2}.$$

4. Correction

$$\hat{x}(n|n) = \hat{x}(n|n-1) + K(n)\big(x(n) - C\hat{s}(n|n-1)\big).$$

5. Minimum MSE

$$M(n|n) = \big(1 - K(n)\big)M(n|n-1).$$

C.3 Experimental setup for measuring sidebands on light

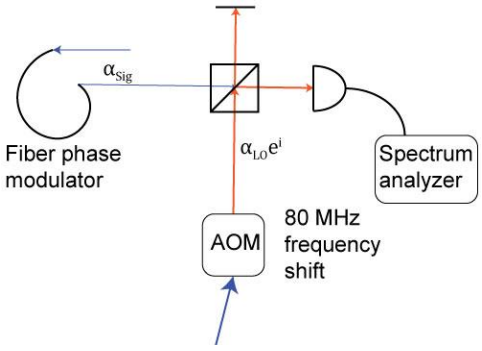

Figure C.1: Experimental setup for measuring the sidebands put on the light using a fiber modulator.

Figure C.1 shows the experimental setup used for measuring the sidebands of light generated using a fiber modulator in our phase tracking experimental setup. We overlap the phase modulated beam with another beam, 80 MHz shifted from the carrier of the phase modulated beam, on a 50:50 beam splitter. We measure the output using a diode and a spectrum analyzer.

C.4 Derivation of power measurement using a Heterodyne detector

We used the expressions relating the electrical signals from the devices to the phase sensitivity of our interferometer. Here we derive those expressions. Figure C.2 shows a schematic of a homodyne detector.

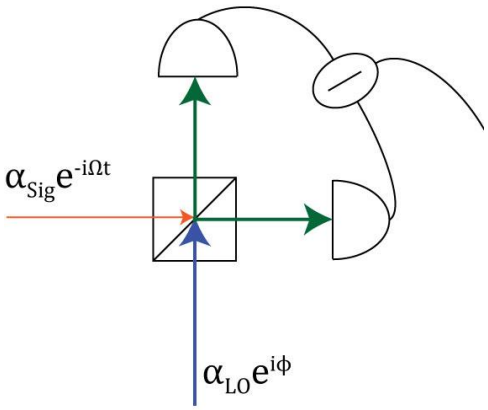

Figure C.2: Heterodyne detector with the signal beam α_{Sig} overlapping with a local oscillator $\alpha_{LO}e^{i\phi}$. The power in the LO beam is much higher than the signal beam, i.e., $|\alpha_{LO}| \gg |\alpha_{sig}|$.

We can describe the output in the two ports of the 50:50 beam splitter by the equations

$$P_1 = \frac{1}{2}\left(\left|\alpha_{Sig}\right|^2 + |\alpha_{LO}|^2 + 2\left|\alpha_{Sig}\right||\alpha_{LO}|\cos(\phi + \Omega t)\right),$$

$$P_2 = \frac{1}{2}\left(\left|\alpha_{Sig}\right|^2 + |\alpha_{LO}|^2 - 2\left|\alpha_{Sig}\right||\alpha_{LO}|\cos(\phi + \Omega t)\right).$$

We subtract one output of the beam splitter from the other to give

$$\Delta P = 2\left|\alpha_{Sig}\right||\alpha_{LO}|\cos(\phi + \Omega t).$$

Now given the power P falling on the diodes, the electrical current generated by the detectors is given by $i = \rho P$, where ρ is the responsivity of the detectors. We can find the difference current generated by the diodes, as

$$i = \rho\Delta P = 2\rho\left|\alpha_{Sig}\right||\alpha_{LO}|\cos(\phi + \Omega t)\,. \qquad (C.11)$$

Since we try to measure the signal to noise ratio (SNR) of the measurement, we must measure the power of the associated signal. The power of the difference current as measured across an $R = 50\,\Omega$ resistor is

$$P_{elec} = i^2 R = 4R\rho^2 \left|\alpha_{Sig}\right|^2 |\alpha_{LO}|^2 \langle \cos^2(\phi + \Omega t)\rangle. \qquad (C.12)$$

Since the expectation $\langle \cos^2(\phi + \Omega t)\rangle = \frac{1}{2}$, we have

$$P_{elec} = 2R\rho^2 \left|\alpha_{Sig}\right|^2 |\alpha_{LO}|^2. \qquad (C.13)$$

Since we observe the signal to noise ratio (SNR) of the measurement, we need an expression for the noise. For a coherent beam, the photon number has a Poisson distribution, which manifests itself into the current produced by the detectors. For a power P of light falling on a diode, the noise power in the current is given by, $\Delta P_{elec} = 2eiBR$ [31], here B is the measurement bandwidth, e is the electronic charge, and R is the $50\,\Omega$ resistor used in the equation $(C.12)$. The total noise generated by the two diodes in the homodyne detector is

$$\Delta P_{elec} = 2eBR(P_1 + P_2) = 2eBR\rho|\alpha_{LO}|^2 \qquad (C.14)$$

The above equation assumes $|\alpha_{LO}| \gg |\alpha_{Sig}|$. We can compute the SNR of the measurement using equations $(C.13)$ and $(C.14)$,

$$SNR = \frac{P_{elec}}{\Delta P_{elec}} = \frac{2\rho\left|\alpha_{Sig}\right|^2}{eB}. \qquad (C.15)$$

We can use the SNR of the measurement from a device like a spectrum analyzer, and estimate the power of the signal beam, i.e., $\left|\alpha_{Sig}\right|^2$ from equation $(C.15)$.

References

[1] A. Crespi, M. Lobino, J. C. F. Mathews, A. Politi, C. R. Neal , R. Ramponi, R. Osellame and J. L. O'Brien, "Measuring protein concentration with entangled photons," *Appl. Phys. Lett.,* vol. 100, no. 23, p. 233704 , 2012.

[2] B. P. Abbott et al., "Observation of Gravitational Waves from a Binary Black Hole Merger," *Phys. Rev. Lett.,* vol. 116, no. 6, p. 061102, 2016.

[3] C. M. Caves, "Quantum-mechanical noise in an interferometer," *Phys. Rev. D,* vol. 23, no. 8, pp. 1693--1708, 1981.

[4] P. Grangier, R. E. Slusher, B. Yurke and A. LaPorta, "Squeezed-light–enhanced polarization interferometer," *Phys. Rev. Lett.,* vol. 59, no. 19, pp. 2153-2156, 1987.

[5] M. Xiao, L. Wu and H. J. Kimble, "Precision measurement beyond the shot-noise limit," *Phys. Rev. Lett.,* vol. 59, no. 3, pp. 278-281, 1987.

[6] M. J. Holland and K. Burnett, "Interferometric Detection of Optical Phase Shifts at the Heisenberg Limit," *Phys. Rev. Lett.,* vol. 71, no. 9, pp. 1355-1358, 1993.

[7] M. W. Mitchell, J. S. Lundeen and A. M. Ateinberg, "Super-resolving phase measurements with a multiphoton entangled state," *Nature,* vol. 429, pp. 161-164, 2004.

[8] B. Yurke, S. McCall and J. Klauder, "SU(2) and SU(1,1) interferometers," *Phys. Rev. A,* vol. 33, no. 6, pp. 4033-4054, 1986.

[9] M. Manceau, G. Leuchs, F. Khalili and M. Chekhova, "Detection Loss Tolerant Supersensitive Phase Measurement with an SU(1,1) Interferometer," *Phys. Rev. Lett.,* vol. 119, no. 22, p. 223604 , 2017.

[10] F. Hudelist, J. Kong, C. Liu, J. Jing, Z. Y. Ou and W. Zhang, "Quantum metrology with parametric amplifier-based photon correlation interferometers," *Nature Communications,* vol. 5, no. 3049, 2014.

[11] S. Liu, Y. Lou, J. Xin and J. Jing, "Quantum Enhancement of Phase Sensitivity for the Bright-Seeded SU(1,1) Interferometer with Direct Intensity Detection," *Phys. Rev. Applied,* vol. 10, no. 6, p. 064046, 2018.

[12] Z. Y. Ou, "Enhancement of the phase-measurement sensitivity beyond the standard quantum limit by a nonlinear interferometer," *Phys. Rev. A,* vol. 85, no. 2, p. 023815, 2012.

[13] A. M. Marino, N. V. Corzo Trejo and P. D. Lett, "Effect of losses on the performance of an SU(1,1) interferometer," *Phys. Rev. A,* vol. 86, no. 2, p. 023844, 2012.

[14] M. A. Armen, J. K. Au, J. K. Stockton, A. C. Doherty and H. Mabuchi, "Adaptive Homodyne Measurement of Optical Phase," *Phys. Rev. Lett.,* vol. 89, no. 13, p. 133602 , 2002.

[15] e. a. Yonezawa H., "Quantum-Enhanced Optical-Phase Tracking," *Science ,* vol. 337, pp. 1514-1517, 2012.

[16] A. A. Berni, T. Gehring, B. M. Nielsen, V. Händchen, M. G. A. Paris and U. L. Andersen, "Ab initio quantum-enhanced optical phase," *Nature Photonics,* vol. 9, p. 577–581, 2015.

[17] G. Y. Xiang, B. L. Higgins, D. W. Berry, H. M. Wiseman and G. J. Pryde, "Entanglement-enhanced measurement of a completely unknown optical phase," *Nature Photonics,* vol. 5, pp. 43-47, 2011.

[18] C. Gerry and P. Knight, Introductory Quantum Optics, Cambridge University Press, 2005.

[19] A. Lvovsky, "Squeezed light," *arXiv:1401.4118,* 2016.

[20] Y. Takeno, M. Yukawa, H. Yonezawa and A. Furusawa, "Observation of -9 dB quadrature squeezing with improvement of phase stability in homodyne measurement," *Optics Express,* vol. 15, no. 7, pp. 4321-4327, 2007.

[21] M. Mehmet, H. Vahlbruch, N. Lastzka, K. Danzmann and R. Schnabel, "Observation of squeezed states with strong photon-number oscillations," *Phys. Rev. A,* vol. 81, no. 1, p. 013814, 2010.

[22] T. Eberle, S. Steinlechner, J. Bauchrowitz, V. Händchen, H. Vahlbruch, M. Mehmet, H. Müller-Ebhardt and R. Schnabel, "Quantum Enhancement of the Zero-Area Sagnac Interferometer Topology for Gravitational Wave Detection," *Phys. Rev. Lett.,* vol. 104, no. 25, p. 251102 , 2010.

[23] C. F. McCormick, V. Boyer, E. Arimondo and P. D. Lett, "Strong relative intensity squeezing by four-wave mixing in rubidium vapor," *Optics Letters,* vol. 32, no. 2, pp. 178-180, 2007.

[24] C. F. McCormick, A. M. Marino, V. Boyer and P. D. Lett, "Strong low-frequency quantum correlations from a four-wave-mixing amplifier," *Phys. Rev. A,* vol. 78, no. 4, p. 043816, 2008.

[25] V. Boyer, A. M. Marino and P. D. Lett, "Generation of Spatially Broadband Twin Beams for Quantum Imaging," *Phys. Rev. Lett.,* vol. 100, no. 14, p. 143601, 2008.

[26] A. M. Marino, R. C. Pooser, V. Boyer and P. D. Lett, "Tunable delay of Einstein–Podolsky–Rosen entanglement," *Nature,* vol. 457, pp. 859-862, 2009.

[27] H. Vahlbruch, M. Mehmet, K. Danzmann and R. Schnabel, "Detection of 15 dB Squeezed States of Light and their Application for the Absolute Calibration of Photoelectric Quantum Efficiency," *Phys. Rev. Lett.,* vol. 117, no. 11, p. 110801, 2016.

[28] V. Boyer, A. M. Marino, R. C. Pooser and P. D. Lett, "Entangled Images from Four-Wave Mixing," *Science,* vol. 321, no. 5888, pp. 544-547, 2008.

[29] S. Donati, Photodetectors: Devices, Circuits, and Applications, Prentice Hall PTR, 2000.

[30] J. Appel, D. Hoffman, E. Figueroa and A. Lvovsky, "Electronic noise in optical homodyne tomography," *Phys. Rev. A,* vol. 75, no. 3, p. 035802, 2007.

[31] A. J. Stevenson, M. B. Gray, C. C. Harb, D. E. McClelland and H.-A. Bachor, "Interferometers with Internal and External Phase Modulation: Experimental and Analytical Comparison," *Australian Journal of Physics,* vol. 48, no. 6, pp. 971-997, 1995.

[32] Z. Wan, J. Feng, Y. Li and K. Zhang, "Comparison of phase quadrature squeezed states generated from degenerate optical parametric amplifiers using PPKTP and PPLN," *Optics Express,* vol. 26, no. 5, pp. 5531-5540, 2018.

[33] S. Suzukia, H. Yonezawa, F. Kannari, M. Sasaki and A. Furusawa, "7dB quadrature squeezing at 860nm with periodically poled KTiOPO4," *Appl. Phys. Lett.,* vol. 89, no. 6, p. 061116, 2006.

[34] E. Magnan, J. Maslek, C. Bracamontes, A. Restelli, T. Boulier and J. V. Porto, "A low-steering piezo-driven mirror," *Review of Scientific Instruments,* vol. 89, no. 7, p. 073110, 2018.

[35] M. Turnbull, *Multi-spatial-mode quadrature squeezing from four-wave mixing in a hot atomic vapour,* http://etheses.bham.ac.uk/id/eprint/5148.

[36] D. Wilding, P. Pozzi, O. Soloviev, G. Vdovin and M. Verhaegen, "Adaptive illumination based on direct wavefront sensing in a light-sheet fluorescence microscope," *Optics Express,* vol. 24, no. 22, pp. 24896-24906, 2016.

[37] C. Bourgenot, C. D. Saunter, J. M. Taylor, J. M. Girkin and G. D. Love, "3D adaptive optics in a light sheet microscope," *Optics Express,* vol. 20, no. 12, pp. 13252-13261, 2012.

[38] J. D. Wong-Campos, K. Johnson, B. Neyenhuis, J. Mizrahi and C. Monroe, "High-resolution adaptive imaging of a single atom," *Nature Photonics,* vol. 10, p. 606–610, 2016.

[39] J. Girkin, S. Poland and A. J. Wright, "Adaptive optics for deeper imaging of biological samples," *Current Opinion in Biotechnology,* vol. 20, no. 1, pp. 106-110, 2009.

[40] V. Bagnoud and J. D. Zuegel, "Independent phase and amplitude control of a laser beam by use of a single-phase-only spatial light modulator," *Optics Letters,* vol. 29, no. 3, pp. 295-297, 2004.

[41] J. A. Davis, K. O. Valadéz and D. M. Cottrell, "Encoding amplitude and phase information onto a binary phase-only spatial light modulator," *Applied Optics,* vol. 42, no. 11, pp. 2003-2008, 2003.

[42] P. Birch, R. Young, D. Budgett and C. Chatwin, "Dynamic complex wave-front modulation with an analog spatial light modulator," *Optics Letters,* vol. 26, no. 12, pp. 920-922, 2001.

[43] T. COLOMB, "Numerical aberrations, compensation, and polarization imaging in digital holographic microscopy," [Online]. Available: https://infoscience.epfl.ch/record/64346/files/EPFL_TH3455.pdf.

[44] C. W. Helstrom, Quantum detection and estimation theory, Academic, 1976.

[45] M. G. A. Paris, "Quantum estimation for quantum technology," *Int. J. Quantum Inf.,* vol. 07, pp. 125-137, 2009.

[46] H. L. V. Trees, K. L. Bell and Z. Tian, Detection Estimation and Modulation Theory, Part I: Detection, Estimation, and Filtering Theory, Wiley, 2013.

[47] H. M. Wiseman and G. J. Milburn, Qunatum Measurement and Control, Cambridge University Press, 2010.

[48] C. Sparaciari, S. Olivares and M. G. A. Paris, "Gaussian-state interferometry with passive and active elements," *Phys. Rev. A,* vol. 93, no. 2, p. 023810 , 2016.

[49] Z. Chen, C. Yuan, H. Ma, D. Li, L. Q. Chen, Z. Y. Ou and W. Zhang, "Effects of losses in the atom-light hybrid SU(1,1) interferometer," *Optics Express,* vol. 24, no. 16, pp. 17766-17778, 2016.

[50] B. E. Anderson, B. L. Schmittberger, P. Gupta, K. M. Jones and P. D. Lett, "Optimal phase measurements with bright- and vacuum-seeded SU(1,1) interferometers," *Phys. Rev. A,* vol. 95, no. 6, p. 063843, 2017.

[51] M. A. Nielsen and I. L. Chuang, Quantum Computation and Quantum Information, Cambridge: (Cambridge University Press, 2000.

[52] W. M. Plick, J. P. Dowling and G. S. Agarwal, "Coherent-light-boosted, sub-shot noise, quantum interferometry," *New Journal of Physics,* vol. 12, p. 083014, 2010.

[53] B. E. Anderson, P. Gupta, B. L. Schmittberger, T. Horrom, C. H. Avigliano, K. M. Jones and P. D. Lett, "Phase sensing beyond the standard quantum limit with a variation on the SU (1, 1) interferometer," *Optica,* vol. 4, no. 7, pp. 752-756, 2017.

[54] P. Gupta, B. L. Schmittberger, B. E. Anderson, K. M. Jones and P. D. Lett, "Optimized phase sensing in a truncated SU(1,1) interferometer," *Optics Express,* vol. 26, no. 1, pp. 391-401, 2018.

[55] M. Manceau, F. Khalili and M. Chekhova, "Improving the phase super-sensitivity of squeezing-assisted interferometers by squeeze factor unbalancing," *New Journal of Physics,* vol. 19, p. 013014, 2017.

[56] E. Giese, S. Lemieux, M. Manceau, R. Fickler and R. W. Boyd, "Phase sensitivity of gain-unbalanced nonlinear interferometers," *Phys. Rev. A,* vol. 96, no. 5, p. 053863 , 2017.

[57] C. M. Caves, "Quantum-mechanical noise in an interferometer," *Phys. Rev. D,* vol. 23, no. 8, p. 1693, 1981.

[58] S. L. Braunstein, "How large a sample is needed for the maximum likelihood estimator to be approximately Gaussian?," *J. Phys. A: Math. Gen.,* vol. 25, no. 13, pp. 3813-3826, 1992.

[59] G. A. Durkin and J. P. Dowling, "Local and Global Distinguishability in Quantum Interferometry," *Phys. Rev. Lett.,* vol. 99, no. 7, p. 070801 , 2007.

[60] B. L. Higgins, D. W. Berry, S. D. Bartlett, H. M. Wiseman and G. J. Pryde, "Entanglement-free Heisenberg-limited phase estimation," *Nature,* vol. 450, p. 393–396, 2007.

[61] H. M. Wiseman, "Adaptive Phase Measurements of Optical Modes: Going Beyond the Marginal," *Phys. Rev. Lett. ,* vol. 75, no. 25, p. 4587 , 1995.

[62] H. M. Wiseman and R. B. Killip, "Adaptive single-shot phase measurements: The full quantum theory," *Phys. Rev. A,* vol. 57, no. 3, p. 2169, 1998.

[63] D. W. Berry and H. M. Wiseman, "Optimal States and Almost Optimal Adaptive Measurements for Quantum Interferometry," *Phys. Rev. Lett.,* vol. 85, no. 24, p. 5098, 2000.

[64] D. W. Berry and H. M. Wiseman, "Adaptive quantum measurements of a continuously varying phase," *Phys. Rev. A,* vol. 65, no. 4, p. 043803 , 2002.

[65] D. W. Berry and H. M. Wiseman, "Adaptive phase measurements for narrowband squeezed beams," *Phys. Rev. A,* vol. 73, no. 6, p. 063824 , 2006.

[66] T. A. e. a. Wheatley, "Adaptive Optical Phase Estimation Using Time-Symmetric Quantum Smoothing," *Phys. Rev. Lett.,* vol. 104, no. 9, p. 093601 , 2010.

[67] G. Y. Xiang, B. L. Higgins, D. W. Berry, H. M. Wiseman and G. J. Pryde, "Entanglement-enhanced measurement of a completely unknown optical phase," *Nature Photonics,* vol. 5, pp. 43-47, 2011.

[68] S. Daryanoosh, S. Slussarenko, D. W. Berry, H. M. Wiseman and G. J. Pryde, "Experimental optical phase measurement approaching the exact Heisenberg limit," *Nature Communications,* vol. 9, no. 4606, 2018.

[69] M. Tsang, J. H. Shapiro and S. Lloyd, "Quantum theory of optical temporal phase and instantaneous frequency. II. Continuous-time limit and state-variable approach to phase-locked loop design," *Phys. Rev. A,* vol. 79, no. 5, p. 053843, 2009.

[70] S. M. Kay, Fundamentals of statistical signal processing: Extimation Theory, New Jersey: Prentice Hall PTR, 1993.

[71] J. L. Gómez-Muñoz and F. Delgado , *Quantum Notation,* 2.3.0 ed., 2011.

[72] G. Agarwal, Quantum Optics, Cambridge University Press, 2012.

[73] C. Brif, A. Vourdas and A. Mann, "Analytic representations based on SU(1,1) coherent states and their applications," [Online]. Available: http://cds.cern.ch/record/307838/files/9607022.pdf.

[74] "Thorlabs," [Online]. Available: https://www.thorlabs.com/catalogpages/V21/1613.PDF.

[75] R. Barakat and B. H. Sandler, "Determination of the wave-front aberration function from measured values of the point-spread function: a two-dimensional phase retrieval problem," *Journal of the Optical Society of America A,* vol. 9, no. 10, pp. 1715-1723, 1992.